Improvement in Reliability of Crystalline Silicon Solar Cell Interconnection by Using Nickel Micro-Plating Bonding (NMPB) Technology

Xinguang YU

February 2023

Waseda University Doctoral Dissertation

Improvement in Reliability of Crystalline Silicon Solar Cell Interconnection by Using Nickel Micro-Plating Bonding (NMPB) Technology

Xinguang YU

Graduate School of Information,

Production and Systems (IPS), Waseda University

February 2023

Acknowledgements

I am especially thankful to my supervisor Prof. Kohei Tatsumi for his patience, guidance and time as well as for giving me the opportunity to be committed to this new research area. Also, I am very grateful to Mr. Isamu Morisako for his valuable advice, constant encouragement, insightful comments and great support. He was an outstanding role model and excellent mentor, providing me with inspiration for high-quality professional work. I specially thank Mr. Ryota Domen, Zhi Fu and Junichi Kasahara for his time, and contributions on experiments.

Others have contributed to this work in one form or another, for which I am very grateful. In particular, I thank Miss Keiko Koshiba and Ph. D Tomonori Iizuka for all their contributions. At last, I thank for secretary Ms. Syoko Hirose for purchasing experimental materials always as soon as possible.

This study was supported by JST SPRING, Grant Number JPMJSP2128.

NMPB plating solutions used in this study is specially prepared and supplied by Japan Pure Chemical Co., Ltd. (JPC). The solar simulation system used in Chapter 4 of this study is provided by Kyushu Institute of Technology Graduate School of Life Science and Systems Engineering.

The photovoltaic (PV) modules in Chapter 6 of this study were made in Choshu Industry

Co., Ltd. by Mr. Kouichi Hashimoto, and the electroluminescence (EL) and I-V measurements were also performed in the same company.

Abstract

The promotion of light conversion efficiency of crystalline silicon solar cell photovoltaic (PV) modules is a popular research topic. However, excellent light conversion efficiency does not imply that its initial performance is maintained after long-term operation. The long-term reliability of the interconnection to assemble crystalline silicon solar cells in PV modules is critical to ensure the continued performance of a device for up to 25 years. 25 years are the expected warranty period as per PV module manufacturers. Most crystalline silicon PV modules have been reported to fail from corrosion by water vapor, breakage of the solder joint interconnection during daily thermal cycles, and slight vibration caused by wind. The conventional interconnection of PV modules is mainly bonded by a low-melting-point material such as lead or lead-free solder, and the interconnection does not have sufficient heat resistance. Consequently, improvements in interconnection technologies are necessary.

Nickel micro-plating bonding (NMPB) is a new interconnection technology that was developed for power modules and could be applied to crystalline silicon solar cells for the first time. In this technique, copper ribbons bonded with lead or lead-free solder are replaced by copper wires bonded with Ni electroplating film. The NMPB interconnection offers several key advantages, such as, low-temperature (55 °C) process, enhancement of

reliability from strain and stress caused by high temperature, and coefficient of thermal expansion (CTE) mismatch between metals and silicon. Furthermore, the NMPB material, that is, Ni exhibits excellent corrosion resistance.

In this thesis, NMPB was employed as a replacement for traditional solder bonding interconnections in crystalline silicon solar cell PV modules. The electroplating process was optimized by adjusting the plating conditions and thickness of the plating film for solar cell interconnection. Thereafter, three steps were conducted to improve the reliability of the NMPB solar cell interconnection. First, the long-term reliability of the NMPB was evaluated using a resonant-type fatigue testing machine to simulate the deformation caused by thermal cycles and slight vibration caused by wind. Second, the reliability of crystalline silicon solar cells interconnected by NMPB was evaluated during both thermal cycling (TC) and damp heat (DH) tests. Finally, the assembly of PV modules interconnected by the NMPB and evaluation of reliability during the TC test was performed to ensure that their life span could exceed 25 years.

This thesis comprises seven chapters. A summary of each chapter is presented below.

Chapter 1 describes the background, purpose, and outline of this study. First, the current situation of photovoltaic modules and their market share are introduced. Then, the main bonding method of NMPB is described. Consequently, to realize the long-term reliability

of the NMPB, a new method, referred to as the resonant-type fatigue test, is introduced. Furthermore, this chapter briefly explains the main evaluation methods, that is, the TC and DH tests based on the International Electrotechnical Commission (IEC) 61215 used for evaluating the reliability of crystalline silicon solar cells and further PV modules.

Chapter 2 introduces solar cells, explaining photovoltaic module, classification of solar cells, crystalline silicon solar cells, and reliability of solder interconnection. First, this chapter briefly explains the mechanism of light conversion in the solar cells. Then it presents the current status of the various types of solar cells used and clarifies the problems still plaguing traditional solder interconnections.

Chapter 3 introduces the experimental methods and equipment used in this study. First, the plating conditions, plating solution composition, etc. of NMPB are described in detail. It also describes a resonant-type fatigue testing machine, a scanning electron microscope, and other equipment used in this study.

Although various researches have been conducted on bonding reliability of NMPB, based on CTE mismatch, long-term reliability evaluated from the aspect of metal fatigue in high cycle (~10^7) or vibration, has been rarely considered. To this end, Chapter 4 evaluates the long-term reliability of the NMPB. In this section, a test was conducted using a resonant-type fatigue testing machine, and it was estimated whether the

acceleration of fatigue evaluation time and long-term reliability of the NMPB were confirmed. The results show that the fatigue limit of NMPB is higher than that of solder bonding both at room (2.2 times) and high (4.3 times) temperature. Thus, NMPB exhibited much longer-term reliability than solder bonding in the resonant fatigue test.

Based on the excellent long-term reliability of the NMPB, a crystalline silicon solar cell interconnected by an NMPB with copper wire was proposed. Chapter 5 evaluates the reliability of crystalline silicon solar cells interconnected by an NMPB. High reliability was confirmed with approximately 1.9% degradation of output power for up to 1000 thermal cycling (TC) tests and 3.8% for 1000 h of damp heat (DH) test in bare NMPB solar cells. In contrast, 64.7% degradation in the thermal cycling test and 23.0% in the damp heat test were confirmed in solder-bonded solar cells.

In Chapter 6, to realize the life span of PV modules interconnected by NMPB, NMPB and solder bonded PV modules were fabricated with EVA and further encapsulants. Subsequently, TC tests were performed and the results showed that the retention rate of the maximum output power (Pmax) of the NMPB PV modules was 12.8% higher than that of the solder bonding modules after TC cycles. In conclusion, we believe that by replacing solder bonding with NMPB, the life span of PV modules could increase from 25 to 40 years.

Finally, in Chapter 7, a short conclusion of Chapters 4–6 is presented. The greatest benefit of the NMPB is that the lifespan of the PV module can be extended to beyond 25 years, as expected. It will bring other benefits such as lower production cost and being much eco-friendly if NMPB interconnected PV modules could be mass produced.

Contents

Chapter 1: Introduction

1.1 Background

1.1.1 Problems of Photovoltaic (PV) Modules

Nowadays, climate change and extreme weather arise from greenhouse gas have serious influences on our daily life. The main cause of climate change is the continued massive and uncontrolled burning of traditional fossil fuels. Countries and governments are committed to reducing emission of greenhouse gas by replacing conventional fossil fuels with clean energy, such as photovoltaic (PV) and wind energy.

Solar energy is one of the widely used green energy sources and photovoltaic (PV) modules are significantly developed in the last few decades. Crystalline silicon solar cells have been identified as the most viable option for mass production [1]. According to International Energy Agency Photovoltaic Power Systems Programme (IEA-PVPS), despite the COVID-19 pandemic, preliminary reported market data shows that the global PV market again grew significantly in 2020. The total cumulative installed capacity for PV at the end of 2020 reached at least 760,4 GW (DC base) [2]. At least 139,4 GW (DC base) of PV systems have been installed and commissioned in the world in 2020, as shown in Fig 1.1. Furthermore, efficiency of PV modules is also increasing that average efficiency of commercial monocrystalline silicon solar cell could reach 22.6% as shown

in Table 1.1 [3].

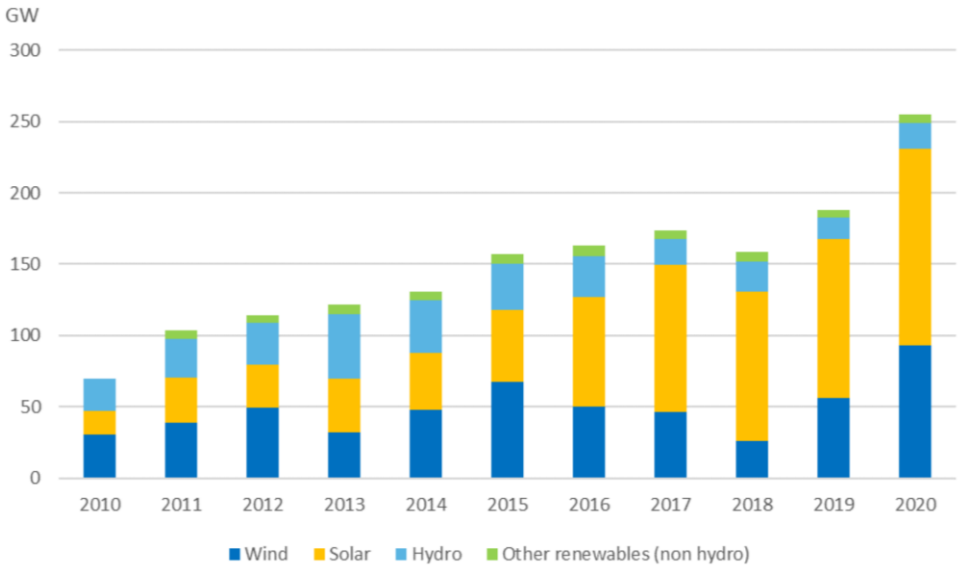

Fig. 1.1 Evolution of renewable energy annual installations [2].

Table 1.1 Top 10 most efficient solar panels [3].

	Maker	**Model**	**Power**	**Efficiency**
1	SunPower	Maxeon 3	400 W	22.6%
2	LG	Neon R	380 W	22.0%
3	REC	Alpha	380 W	21.7%
4	FuturaSun	FU M Zebra	360 W	21.3%
5	Panasonic	EverVolt	370 W	21.2%
6	Trina Solar	Vertex S	405 W	21.1%
7	Jinko Solar	Tiger Pro 6Rl3	390 W	20.7%
8	Q cells	Q.Peak DUO G9	360 W	20.6%
9	Winaico	WST-375MG	375 W	20.6%
10	Longi Solar	Hi-Mo 4	375 W	20.6%

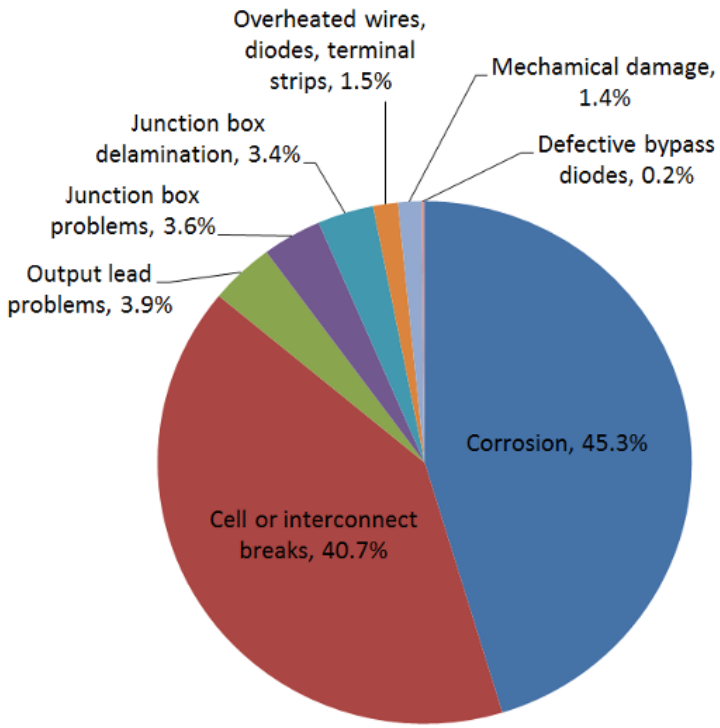

Fig. 1.2 Types of PV module field failures observed [6].

However, a lot of problems still remained to be solved in PV modules such as failure caused by coefficient of thermal expansion (CTE) mismatch and corrosion during outdoor operation. Generally, the expected life span of PV modules is around 25 years. One of the key challenges is untimely failure of solar cells interconnection in the modules. The interconnections provide electrical, mechanical and thermal contact between the solar semiconductor cell and electrodes [4]. Conventional crystalline silicon solar cells are mainly interconnected by low melting point materials such as lead or lead-free solder. By using lead or lead-free copper ribbon interconnection, it is reported that 45.3% of

crystalline PV module fails from corrosion and 40.7% is due to interconnection breakage, as shown in Fig 1.2 [5, 6]. As a result, it is necessary to find a new method to replace soldering technology in order to increase reliability of PV modules.

1.1.2 Nickel Micro-Plating Bonding (NMPB)

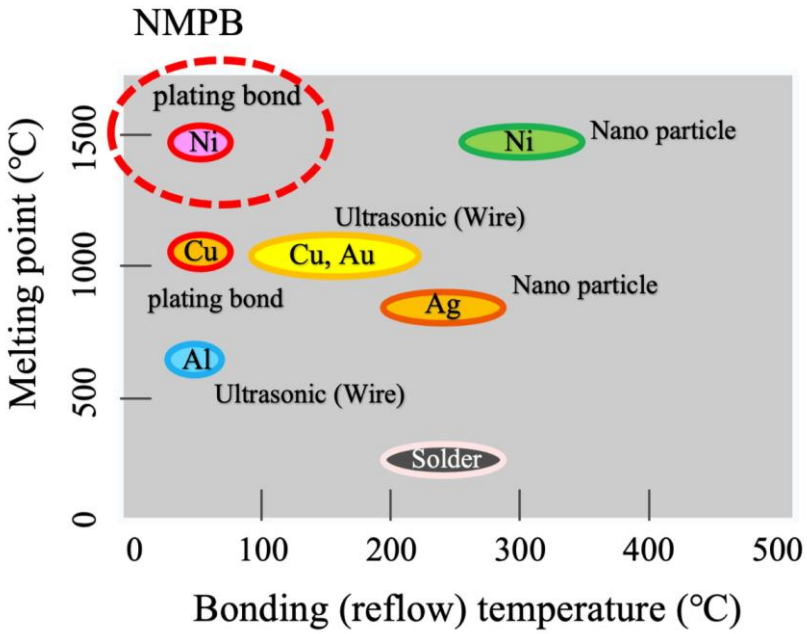

Fig. 1.3 Melting point and bonding temperature for each bonding [8].

Before this study, our laboratory has proposed and experimented with nickel (Ni) micro-plating bonding (NMPB), which uses Ni (melting point is about 1455 ℃) and has excellent heat resistance, as a new bonding method in silicon carbide (SiC) device of power modules [7]. Fig. 1.3 shows melting point and bonding temperature for each bonding

method. Compared with solder bonding process, low process temperature of 55 °C is also an attractive point for high temperature resistant interconnection technology [8]. Chen, C. H. et al. reported that the increasing soldering temperature causes bow and residual stress increase, and the increasing residual stress may cause the damage in the region of wafer near electrode [9]. Also, it was concluded by Shin, H. et al. that Si wafers experience maximum thermo-mechanical stress during the soldering process [10]. On the other hand, Jicheng Gong et al. found clear mechanism of initial intermetallic compound (IMC) formation during solder process [11], which contributes to higher strain energy density and decreases the mean-time-to failure of the assembly joints [12]. In fact, lots of disadvantages of solder and lamination process make it necessary to find a replaceable and valid method for interconnection of solar cells. As a result, low-temperature bonding process, NMPB, becomes a remarkable method for solar cell interconnection.

Previous research has shown that NMPB can be used to secure the heat resistance of the joints above 300 ℃ for the interconnection between the copper (Cu) lead and the Cu electrode [7, 13, 14] as well as between the SiC device and the Cu lead. Fig. 1.4 (a) shows schematic representation of NMPB used in SiC device and (b) columnar crystal of NMPB was observed by Electron Back Scatter Diffraction (EBSD).

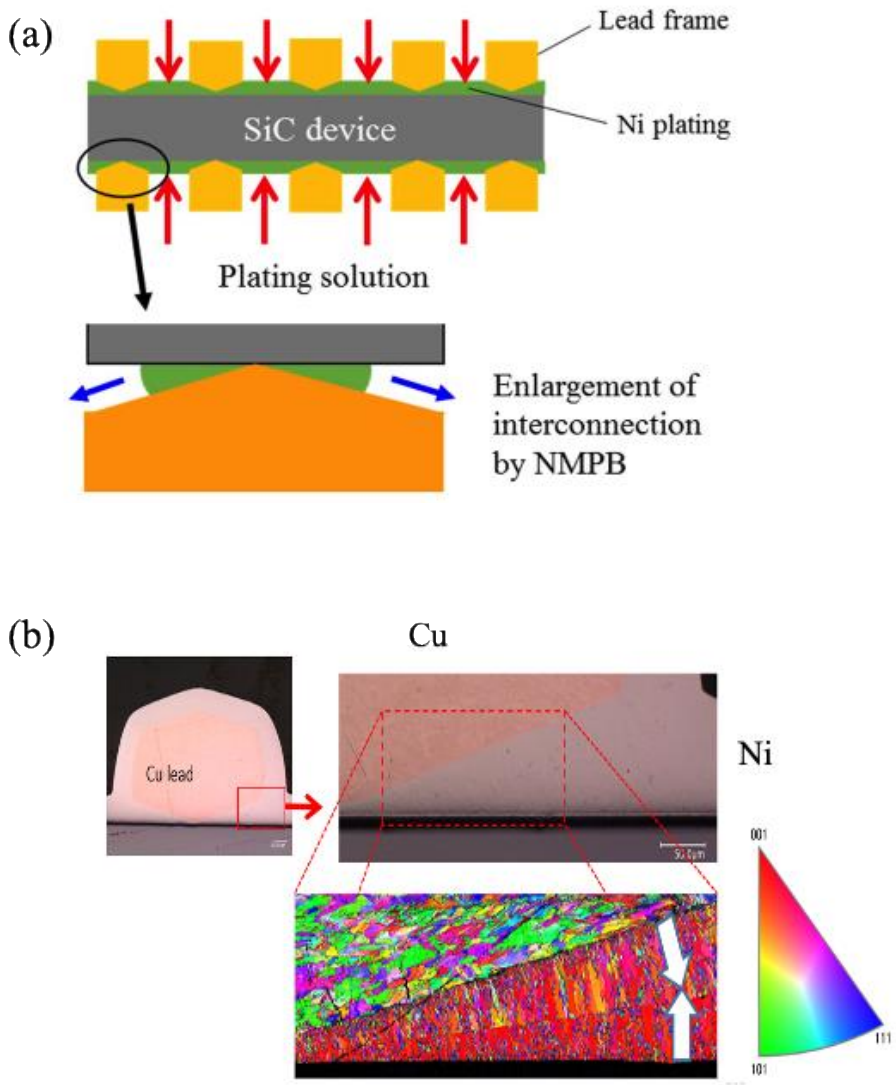

Fig. 1.4 (a) Schematic representation of NMPB using chevron shaped lead frame and (b) SiC device and columnar crystal of NMPB observed by EBSD [13].

Because Ni grew into columnar crystals, the interface could be perfectly bonded without any voids. In order to realize the reliability of NMPB under the influence of CTE mismatch between Si or SiC and Ni, thermal cycling (TC) test was carried out combined with shear test. Fig. 1.5 shows the variation of shear stress by TC test, where we can see

the clear advantage of NMPB interconnection showing the higher strength than Pb-free solder bonding at any TC cycles.

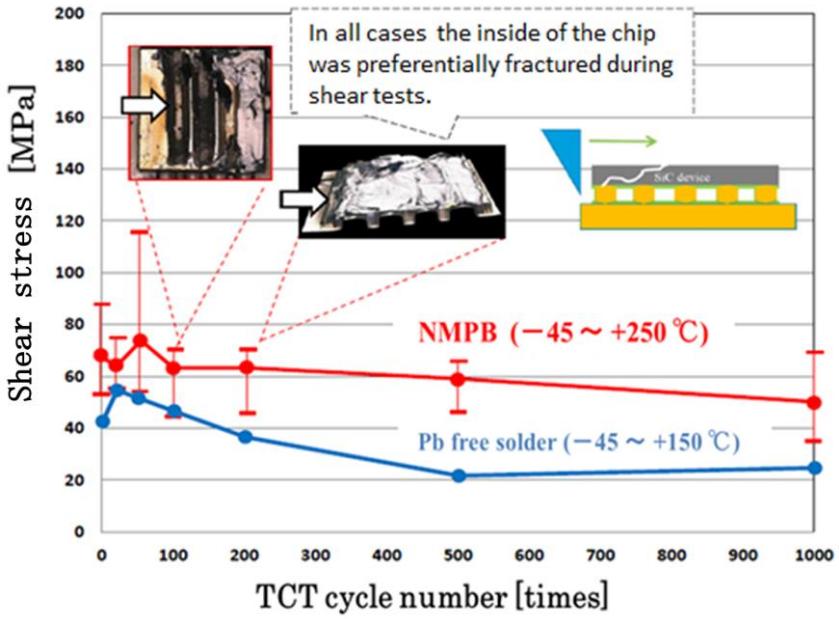

Fig. 1.5 Shear stress variation by TC test [14].

1.1.3 Resonant Type Fatigue (RF) Test

Metal fatigue is a phenomenon in which when a stress is repeatedly applied to metal, fatigue cracks occur or propagate even if the stress is yield stress or less, and fracture occurs. Therefore, it is important to study the fatigue fracture characteristics of metals in order to predict the fatigue life, prevent the fracture of machines, structures, parts, etc., and improve the fatigue fracture strength of materials. Therefore, when NMPB is used

for PV modules, it is necessary to clarify not only the static strength but also the fatigue fracture strength. It is also important to investigate the fatigue fracture strength in the assumed temperature environment, considering that it is applied to parts used in a high temperature environment.

By TC test, time required for one cycle is long, and it is hard to evaluate over 10^3 cycles. However, in application of devices, such as PV module or power module in EV (electric vehicle), high cycle and long-term reliability need to be evaluated. Furthermore, TC test is a sort of fatigue tests that repeated stress comes from CTE mismatch. For this reason, resonant type fatigue test, a method of evaluating long-term reliability instead of TC test, which can simulate the occurrence of deformation during TC test, was used to evaluate fatigue limit and clarify fatigue characteristics of NMPB in a short time.

1.1.4 Evaluation on Reliability of Crystalline Silicon Solar Cell

When long-term reliability of NMPB has been confirmed, it could be further proposed as an innovative method in interconnection of crystalline silicon solar cell that could replace conventional solder bonding methods. Fig. 1.6 shows previous research of SiC chip and Cu lead bonded by NMPB with Cu wire. These results show possibility that NMPB could also be used for Si or metal plate with Cu wire. As a result, this study will

also evaluate reliability of this new technology used in crystalline silicon solar cell. Based on International Electrotechnical Commission (IEC) 61215, TC test and DH (damp heat) test were tested. After TC and DH test, I-V curve will be measured, and maximum output power degradation will also be plotted. At last, reliability of PV module interconnected by NMPB will be evaluated and life span of NMPB PV module could be inferred by comparison with solder bonding.

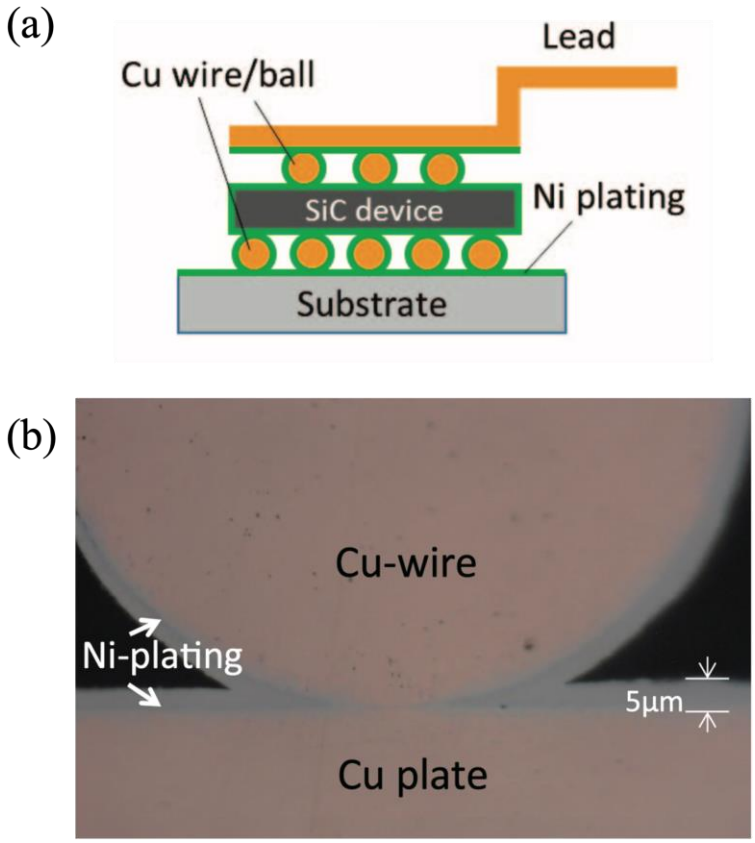

Fig. 1.6 (a) Schematic representation of NMPB using Cu lead with Cu wire [13] and (b) Plating cross section of Cu wire bonded to copper plate [7].

1.2 Objective

1. Evaluate long-term reliability of NMPB by using a resonant type fatigue testing machine.

2. Evaluate reliability of crystalline silicon solar cell interconnected by NMPB both during TC test and DH test.

3. Assemble PV modules interconnected by NMPB and evaluate reliability during TC test to ensure their life span could exceed 25 years.

Chapter 2: Introduction of Solar Cells

2.1 Photovoltaic (PV) Modules

A PV module is a packaged assembly of interconnected solar cells and their further encapsulant and supporting structure. PV modules are known by the type of solar cells used in forming them [15]. The process of transferring from a solar cell to a photovoltaic (PV) system is shown in Fig. 2.1.

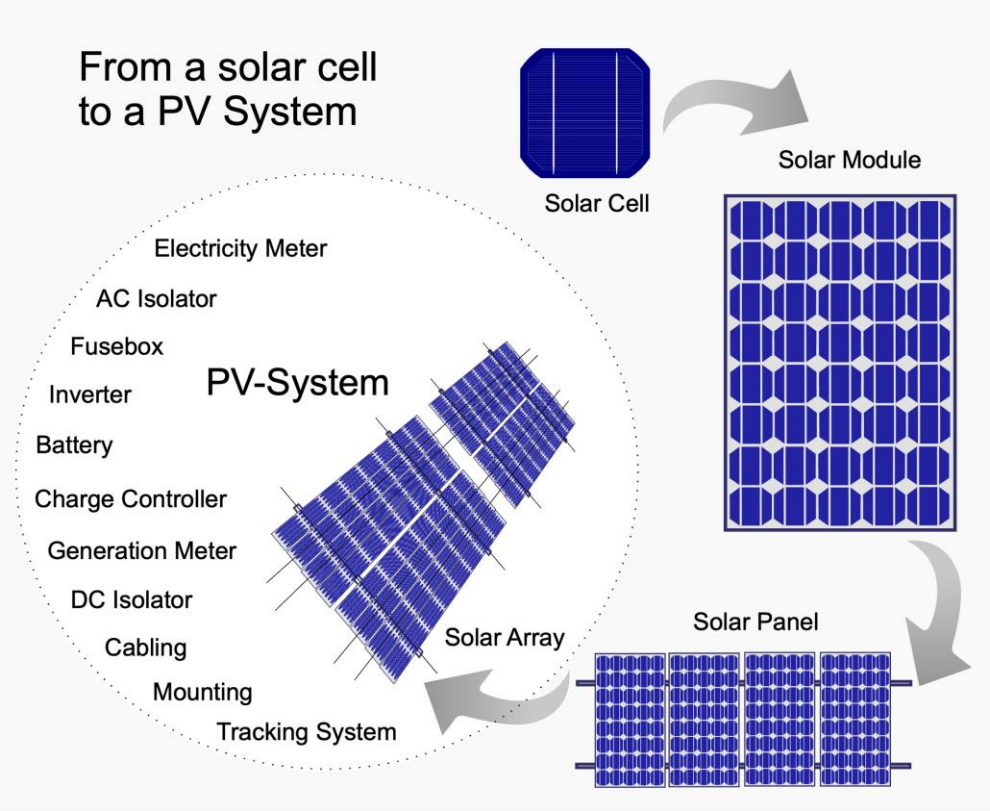

Fig. 2.1 The process for transferring from a solar cell to a PV system [16].

Single solar cells are interconnected with Cu ribbon coated with solder by methods like

reflow process. Then interconnected solar cells will be laminated with ethylene-vinyl acetate (EVA) sheets and Tedlar/PET/Tedlar (TPT) back sheets and further protected by tempered glass. Here, TPT film is polyvinyl fluoride (PVF) film on both sides, and polyethylene terephthalate (PET) film in the middle. These laminated solar cells are called PV modules.

A single solar cell cannot be directly used as a power supply. As a power supply, several single cells must be connected in series and parallel and tightly packed into components. PV modules are the core part and the most important part of the solar power generation system. Its function is to convert the solar energy into electrical energy, or store it into the battery, or promote workload. PV modules could be further combined to each other to form a PV system with an inverter so that they could produce AC electricity used in our usual life, such as house PV system used on the roof, as shown in Fig. 2.2.

Fig. 2.2 Example of PV system used on roof.

The following are the component materials of a PV module.

1. Glass: Ultra-white textured tempered glass which thickness is 3.2 mm, light transmittance is over 91% within the wavelength range of solar cell spectral response (320-1100 nm). It has resistant to ultraviolet radiation while light transmittance does not decrease. Components made of tempered glass can withstand the impact of a 25 mm diameter hockey puck at a speed of 23 m/s.

2. EVA: A high-quality EVA film layer with a thickness of 0.5 mm is used as an encapsulant for solar cells and as a connection with glass and TPT. It has high light transmittance and anti-aging ability.

Performance requirements of EVA film for solar cell encapsulation after curing: Light transmittance greater than 90%; cross-linking degree greater than 65-85%; peel strength (N/cm), glass/film greater than 30, TPT/film greater than 15; temperature resistance: high temperature 85 ℃, low temperature -40 ℃.

3. TPT: The back sheet of solar cell, basic requirements such as aging resistance, corrosion resistance, ultraviolet radiation resistance, and airtightness.

4. Frame: The aluminum alloy frame used has high strength and strong resistance to mechanical impact.

2.2 Classification of Solar Cells

According to the crystalline state, solar cells can be divided into two categories: crystalline thin film type and amorphous thin film type. The former is divided into monocrystal type and polycrystalline type [17].

According to the material, it can be divided into silicon thin film, compound semiconductor thin film and organic film, and the compound semiconductor thin film is divided into amorphous (a-Si:H, a-Si:H:F, etc.), IIIV group (GaAs, InP, etc.), IIVI group (CdS) and zinc phosphide (Zn_3P_2), etc.

According to the different materials used, solar cells can also be divided into silicon solar cell, multi-component compound thin film solar cell, polymer multilayer modified electrode solar cell, nanocrystalline solar cell, organic solar cell, plastic solar cell. Silicon solar cells are the most mature and dominate the applications.

Fig. 2.3 shows classification of major commercial solar cells. It can be realized from Fig. 2.3 that crystalline silicon solar cells have higher energy conversion efficiency when compared with thin-film solar cells consisting of a-Si:H, μc-Si:H, CdTe and CIGS [18-21].

Because there is less usage of busbar in thin-film solar cells, the application of NMPB to PV modules will be focused on crystalline silicon solar cells.

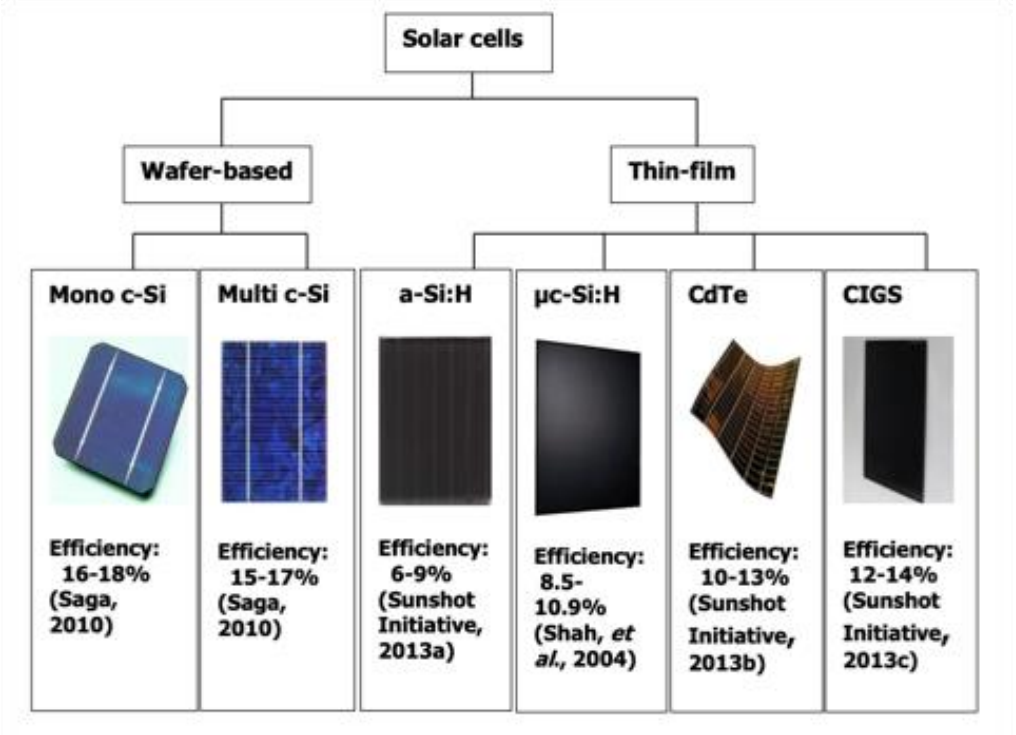

Fig. 2.3 Classification of solar cells [15].

2.3 Crystalline Silicon Solar Cells

Among all type of solar cells, crystalline silicon solar cells still share the main market until now. Crystalline silicon solar cells are the most common and widely used solar cells and have been produced for more than 60 years [15]. The typical structure of a crystalline silicon solar cell is shown in Fig. 2.4. The anti-reflection coating (ARC) is overlaid on the latter and ensures passage of all light to the silicon crystalline layers while minimizing reflection. A transparent adhesive is deposited on the overlaid coating [4]. As can be seen from Fig. 2.5, a back contact material supports a positive type (P-type) semiconductor layer which also has a negative type (N-type) semiconductor layer on it [22].

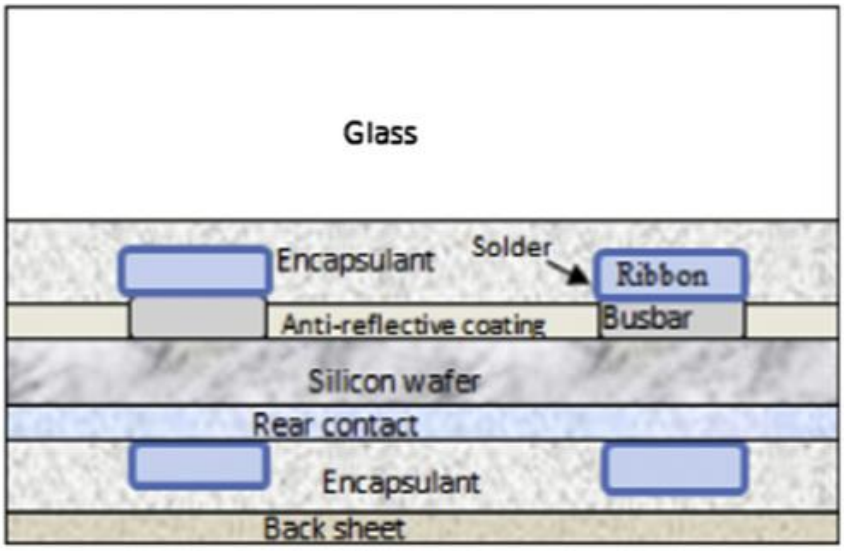

Fig. 2.4 Schematic of cross-section of a typical laminated crystalline Si solar cell [4].

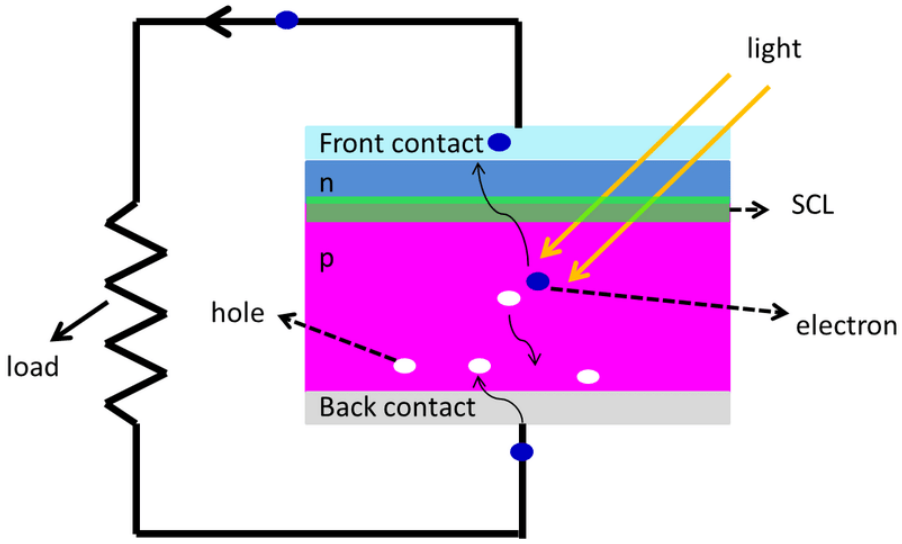

Fig. 2.5 PN junction of solar cell [22].

A solar cell is a device that converts solar energy into electrical energy by using the photovoltaic effect of semiconductor materials. The basic process of the photovoltaic effect is that light is irradiated on the solar cell and the light is accepted at the interface layer, photons with sufficient energy can excite electrons from covalent bonds in P-type silicon and N-type silicon, resulting in the generation of electron-hole pairs. The electrons and holes adjacent to the interface layer will be separated from each other by the electric field effect before recombination. Electrons move to the positively charged N region and holes move to the negatively charged P region. The charges through the interface layer will form an outward voltage between the P region and the N region.

For crystalline silicon solar cells, the typical value of the open circuit voltage is 0.5~0.6V.

When more electron-hole pairs are generated in the interface layer by light, current will be higher. When more light energy is received by the interface layer and area of the interface layer is larger, the higher the current will be formed in the solar cell.

2.4 Reliability of Solder Interconnection

The PV modules must ensure the reliability of solder interconnection in the manufacturing process and under the service conditions. The power generation of PV modules are influenced by local weather, which will also affect their life span and service time. For example, compared with modules in tropical or temperate weather, modules in desert weather have shorter life span [23]. Therefore, higher temperature will lead to faster degradation of PV modules, which indicates that temperature has an impact on PV module components. Furthermore, other reports indicate that during field operation, the diurnal temperature cycle affects PV module and leads to degradation, which eventually results in PV module failure [24-28]. No matter what the weather conditions are, PV modules will degrade due to thermal load as long as they are exposed to daily sunlight. In addition, according to another report, in most cases, passing clouds often cause temperature changes of more than 20 ℃ for many times in one day, while the diurnal temperature cycles will cause a change of 12 ℃ within 24 hours [29]. The main reason leads to failure of PV modules is cyclic thermos-mechanical fatigue loading. This kind of loading related to degradation of the solar cell interconnection and eventually PV module failure.

Other research also reported that corrosion is also a significant influence for reliability

of PV modules. According to N. Park et al., Wonwook Oh et al. and T.H. Kim et al., in hot and humid climates, PV modules will experience moisture condensation, and the resulting water will cause corrosion in more areas [30-32]. With aging of EVA sheet and back sheet, moisture can also penetrate encapsulant and infiltrate surface of solar cells, which contribute further corrosion. It was also reported that increase of the series resistance is due to the reduction solder interconnection and the oxidation of the front silver finger caused by high moisture stress and thermal stress [33]. H. Xiong et al. also reported that after aging test, smooth oxide and loose structure in aluminum paste layer (APL) of solar cell were found [34].

Furthermore, due to environmental problems, lead solders are gradually replaced by lead-free solders because lead has a harmful influence on human body. However, lead-free solders have higher melting points which will exacerbate the effect from thermal stresses on the interconnection of solar cells during soldering process. As a result, it is a challenge to use new technology to replace soldering for realizing longer life span of PV modules.

Chapter 3: Experimental Methods and Equipment Used

3.1 Electroplating and Electroless Plating

Plating can be roughly divided into electroplating and electroless plating. Electroplating is a plating method that uses an external DC power source to form thin metal film by cathodic reduction of metal ions in the aqueous solution. Electroless plating is a plating method to form thin metal film that uses electrons supplied by the oxidation reaction of the reducing agent added to the aqueous solution [35].

Since it became clear in the previous research of our laboratory that it is difficult to form a bond by electroless plating, we have been researching on bonding method by electroplating. Electroplating will be evaluated in this study as well. Table 3.1 shows a comparison between the properties of Ni-P electroless plating film and Ni electroplating film [36].

Table 3.1 Comparison of characteristics between electroless Ni-P plating and Ni electroplating [36].

	Electroless Ni-P plating	**Ni electroplating**
Component	90~92% Ni, 8~10% P	99.5% Ni
Structure	amorphous	microcrystalline
Melting point	890 ℃	1455 ℃
Electrical resistance	60 μΩ/cm	8.5 μΩ/cm
Hardness	500±50 HV	150~250 HV (ordinary bath)
Stretching	3~6%	10~30% (ordinary bath) 5~15% (glossy bath)
Stress	compression	tension
Uniform precipitation	less than ±10%	37.50%

3.2 Nickel Micro-Plating (electrolytic) Bonding

Our laboratory has been researching on nickel micro-plating bonding (NMPB) as a new bonding technology. In the method of NMPB, plating solution is flowed to wire, or ball contacted with object, and then bond is performed. Electroplating film grows in a peculiar preferential orientation by epitaxial growth. It has been confirmed that plating grows into two directions at the bonding interface of NMPB. And since the bonding interface is formed by twisted grain boundary, a very dense interface without voids is formed at atomic level. Further, since bonding temperature by electroplating is as low as about 55 ℃ and melting point of Ni is 1455 ℃, high melting point Ni can be bonded at low temperature. It is considered that NMPB can ensure reliability in a high temperature environment of about 300 ℃.

3.3 Electroplating Principles and Equipment

Figure 3.1 shows a schematic diagram of the reaction during NMPB. Ni Electroplating

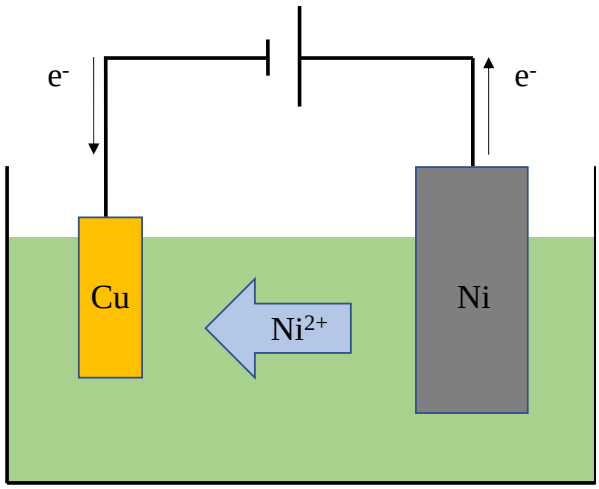

Fig. 3.1 Schematic diagram of Ni electroplating reaction.

involves setting Ni plate on the anode and object to be plated on the cathode, in which Ni precipitated as a plating film, an aqueous solution with Ni^{2+} ions, and applying a current from a DC power supply. The oxidation reaction formula is shown in formula (3-1), and the reduction reaction formula is shown in formula (3-2). On the anode side, an ionization reaction occurs at the interface between the Ni plate and the solution, Ni emits electrons, and Ni^{2+} ions dissolve in the solution. On the other hand, Ni ions undergo a reduction reaction on the cathode side, electrons are combined with Ni^{2+} ions in the solution, and Ni is precipitated.

$$Ni \rightarrow Ni^{2+}+2e^{-} \quad (3\text{-}1)$$

$$Ni^{2+}+2e^{-} \rightarrow Ni \quad (3\text{-}2)$$

In Ni electroplating, the redox reaction represented by the above formula occurs. The object to be plated must be a conductor because electric current need to be applied. Since the current flows on the equipotential surface of the electrode surface, the current distribution on the object to be plated becomes non-uniform, and the current density increases at the convex portion, resulting in a thicker coating and a thinner coating at the concave portion [37].

There are various types of Ni electroplating baths, such as Watt bath and sulfamic acid bath, which have different plating solution compositions. The hardness of the plating film in the Watt bath is about 3 times higher than that in the sulfamic acid bath, but the internal stress is large, and the joint is brittle. In addition, although the hardness of the plating film in the sulfamic acid bath was low, high shear stress was obtained [38]. Since NMPB is required to have bonding reliability, it is considered that Ni electroplating using a sulfamic acid bath is optimal for NMPB. Figure 3.2 shows the appearance of the plating equipment used in the experiment.

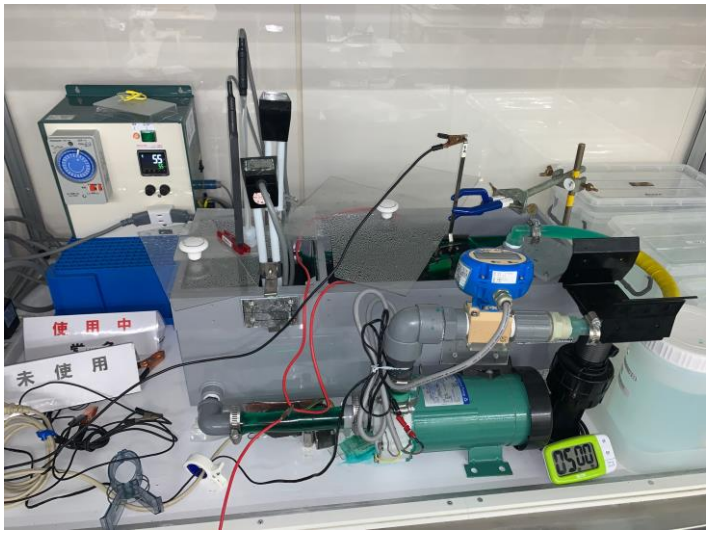

Fig. 3.2 Plating equipment used in the experiment.

Parameters for Ni electroplating include current density, plating bath temperature, pH, stirring flow rate, voltage value, current value, nickel concentration and so on. The structure and uniformity of the plating film, film formation speed, etc. depend on the above parameters. In this study, Ni sulfamic acid plating solution (NS-1605) manufactured by Japan High Purity Chemicals Co., Ltd. (JPC) was used as the plating solution. Table 3.2 shows the basic plating conditions, Table 3.3 shows the composition of the Ni plating solution used. Protective agent plays a role that it gives priority to make grains grow in narrow gap having columnar crystal grain structure so that bonding interface has no voids. To compare the property of NMPB layer to that of conventional Ni plating, in section 4.3, fine grain Ni plating solution was used where stress relaxant

was added to NMPB solution. As a pretreatment, object to be plated was immersed in an acidic solution (H_2O: H_2O_2: H_2SO_4= 2: 1: 1) for about 10 seconds, then washed with pure water and plating started.

Table 3.2 Basic plating experiment conditions.

Items	**Conditions**
Current density	1~10 A/dm²
Plating solution	sulfamic acid bath
Bath temperature	55 ℃
pH	3.6~4.0
Stirring flow rate	5.0 L/min

Table 3.3 Composition of Ni plating solution.

Component	**Content**	
	NMPB	**Fine grain Ni**
Total nickel concentration	83.6 g/L (75%)	83.6 g/L (75%)
Nickel sulfamate	450 g/L	450 g/L
Nickel chloride	7.5 g/L	7.5 g/L
Boric acid	30 g/L	30 g/L
pH	3.6	3.6
Protective agent (N-substituted pyridine compound)	2.0 mL/L	2.0 mL/L
Stress relaxant	none	10.0 mL/L
Surfactant	1.5 mL/L	1.5 mL/L

3.4 Resonant Type Fatigue Testing Machine

3.4.1 Overview

There are various fatigue testing machines such as rotary bending fatigue testing machine and flat surface bending fatigue testing machine, but these typical fatigue testing machines are difficult to test from the viewpoint of test piece size assuming fatigue evaluation of NMPB joints. Therefore, the resonant type thin plate fatigue testing machine (RF-HT, Nihon Techno-Plus Co., Ltd.), enables test in a short time by performing fatigue test which test piece size is small and the amplitude is controlled by resonance. The appearance of RF (resonant type fatigue) testing machine is shown in Fig. 3.3, and the specifications are shown in Table 3.4 [39].

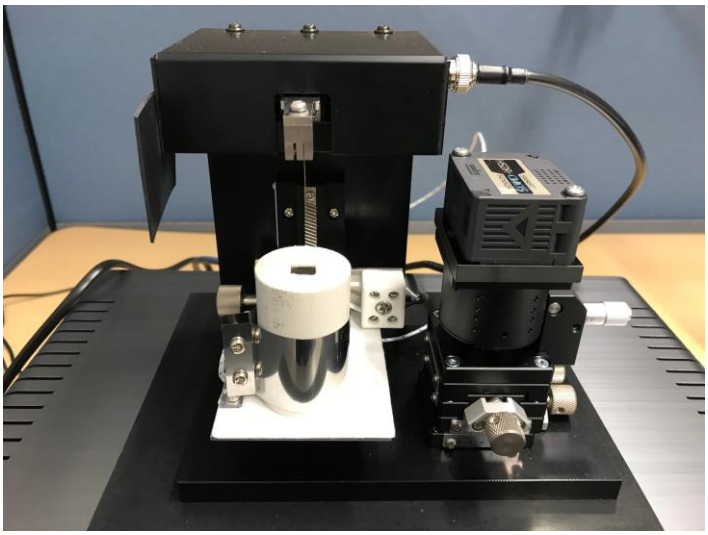

Fig. 3.3 Appearance of resonant type fatigue testing machine.

Table 3.4 Specifications of RF testing machine [39].

Items	Specifications
Test method	resonant plane bending amplitude control method, laser displacement measurement
Measurement item	resonance frequency, bending displacement
Test sample conditions	material: thin plate of metal, ceramics, resin, etc. shape: length about 20~35mm, plate thickness 0.1~0.8 mm, Width 3~8 mm
Drive frequency range	about 100 Hz to 1000 Hz

3.4.2 Configuration of Resonant Type Fatigue Testing Machine

In this study, a strip-shaped test piece with a length of 25 mm, a width of 3 mm, and a thickness of 3.4 mm was used as the fatigue test of NMPB. As for the shape of the test piece, unlike the rotary bending fatigue test and the flat bending fatigue test, which are general fatigue tests, the standard shape of the test piece is not fixed. The shape of test piece was made by referring to the test piece made by the group of Faculty of Engineering, Kumamoto University, who created resonant fatigue testing machine [40]. Figure 3.4 shows the shape of the prepared test piece [41].

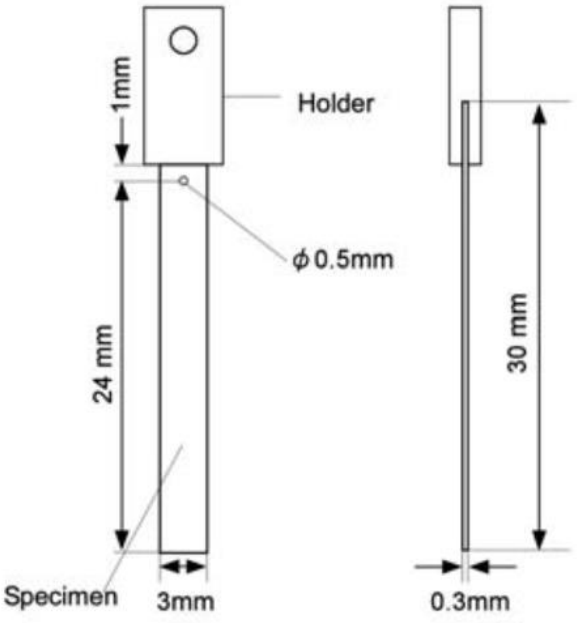

Fig. 3.4 Shape of fatigue test piece [41].

The configuration of the fatigue test machine is shown in Fig. 3.5. The holder attached to the test piece is fixed to the voice coil of the loudspeaker, and the lower end is free end. The voice coil is vibrated using a function generator and an amplifier, and the frequency is adjusted so that the test piece is in 1st mode resonance. When the test piece enters 1st mode resonance, bending occurs, and tensile and compression cyclic stress is applied to the test piece. The vibration modes in this case are shown in Fig. 3.6 (i) to (iv), where Y_h and Y are the maximum amplitudes of the holder and free end of the test piece, respectively. Theoretically, in 1st mode resonance, there is a $\pi/2$ phase shift between holder and free end of the test piece. Therefore, when the free end of the test piece has

the maximum amplitude (ii) and (iv), the amplitude of the test piece holder becomes zero. So, it is possible to evaluate the stress that occurs at the root of the holder of the test piece by measuring only *Y* with a laser displacement meter [40, 41].

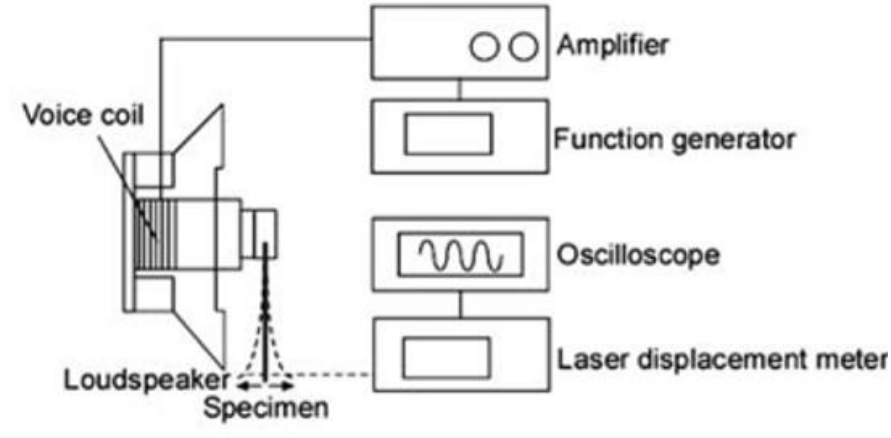

Fig. 3.5 Schematic illustration of the fatigue testing machine [41].

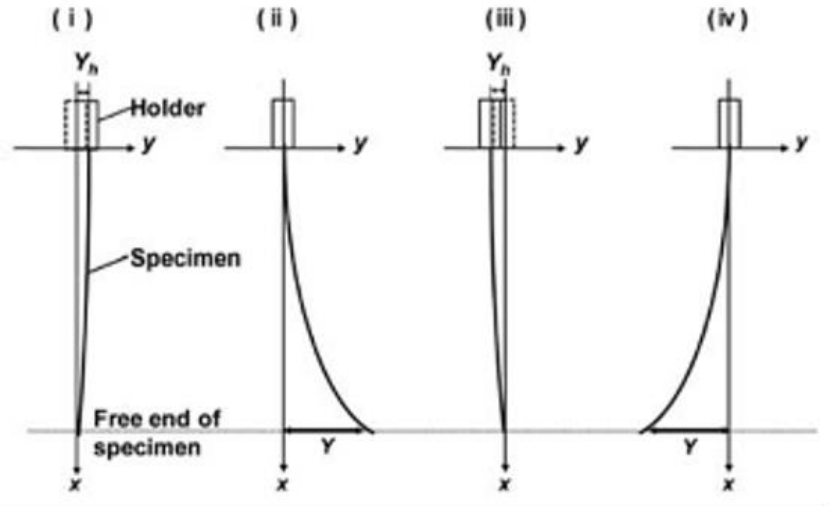

Fig. 3.6 Appearance of resonant type fatigue testing machine [41].

The 1st mode resonant frequency f of the test piece is calculated by the following formula (3-3) [42].

$$f = \lambda/2\pi$$

$$= (140EI)^{1/2}/\{2\pi (11ML^3)^{½} \quad (3\text{-}3)$$

Here, λ is the first-order natural angular frequency, E is Young's modulus, I is the second moment of fracture surface, L and M are the length and the weight from holder to free end of the test piece, respectively. In this test method, the frequency and the output of the amplifier are first set so that Y has a predetermined amplitude in the primary resonant state, but the resonant frequency gradually decreases as cracks develop and grow. Therefore, after cracking, the frequency and output are readjusted so that Y is always kept constant, and tests are conducted.

In the RF test, the frequency and the output of the amplifier are first set so that Y has a predetermined amplitude in the primary resonant state. Young's modulus of the test piece decreases as cracks develop and propagate. By doing so, the resonant frequency gradually decreases. Therefore, a program has been introduced to readjust the frequency and power to keep Y constant after cracks occurred [39, 41]. Then, the test will be terminated when the material is completely broken, or the output of the testing machine became maximum and the reached test limit.

3.4.3 Methods of Fatigue Evaluation

The S-N curve used for fatigue evaluation in this study will be explained. S-N curve is obtained by applying repeated loads such as planar bending, rotational bending, and tension-compression under a constant stress amplitude or amplitude, and plotting the number of repetitions N_f against the stress amplitude required for fracture of the test piece. Figure 3.7 shows a schematic drawing of two types of S-N curves. Generally, the amplitude stress σ_a on the vertical axis is shown on a linear scale, and the number of repetitions N_f on the horizontal axis is shown on a logarithmic scale. In the figure, *a* is a typical S-N curve of mild steel or a material showing a strain aging phenomenon. Under a constant stress amplitude, the curve becomes parallel to the horizontal axis and there will be a break point at a number of repetitions exceeding about 10^6 times. The break point means that fatigue fracture does not occur below this stress amplitude. This amplitude stress is known as the fatigue limit or durability limit, and is said to be about 50% of the tensile strength obtained in a normal tensile test for steels and copper alloys. In non-ferrous metal materials such as copper, the fatigue limit does not appear as shown by curve b in the figure, and the stress amplitude decreases as the number of repetitions increases. In such cases, fatigue limit is defined as the stress amplitude at which the test piece can withstand at least 10^7 times [43]. Since Ni, Cu, and solder evaluated in this

study are materials whose fatigue limit does not appear clearly, fatigue limit was defined as the stress amplitude that can withstand 10^7 repetitions in this study as well.

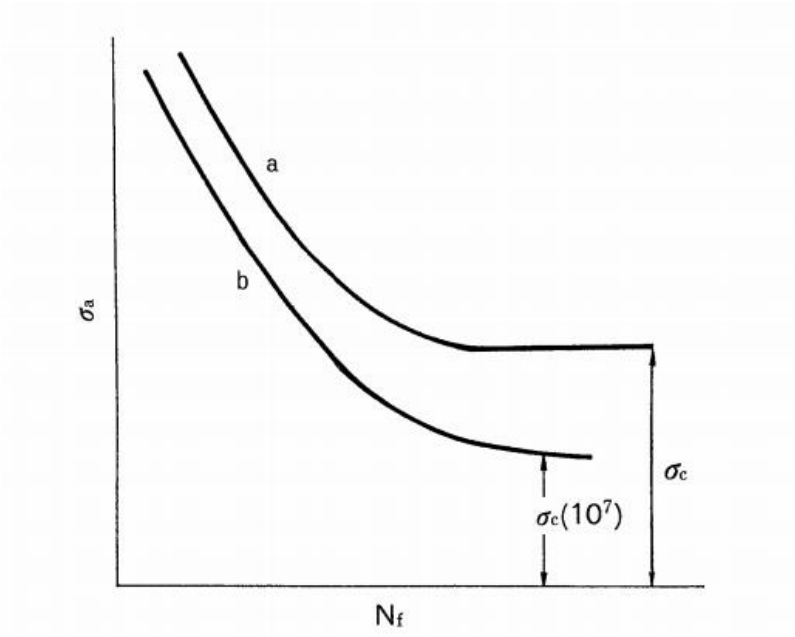

Fig. 3.7 Schematic drawing of fatigue life curve (S-N curve) [43].

3.5 Scanning Electron Microscope (SEM)

The appearance of Scanning Electron Microscope (SEM) is shown in Fig. 3.8. Generally, a SEM image is an image that uses a secondary electron image, and a BSE (back scattering electrons) image is an image that uses back scattered electrons. The principle of BSE will be explained. BSE detects reflected electrons to analyze the composition of the sample surface and visualize irregularities. The ratio of reflected electrons number is

also called the electron reflectance, and this change produces the contrast of the reflected electron image [44]. Fig. 3.9 shows the SEM image, and Fig. 3.10 shows the BSE image.

Fig. 3.8 SEM (SU5000, Hitachi High-Tech Corp.).

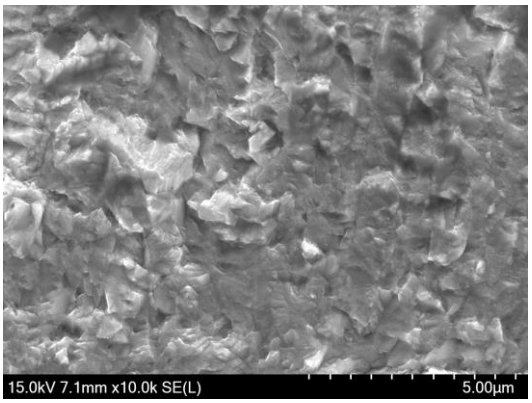

Fig. 3.9 SEM image.

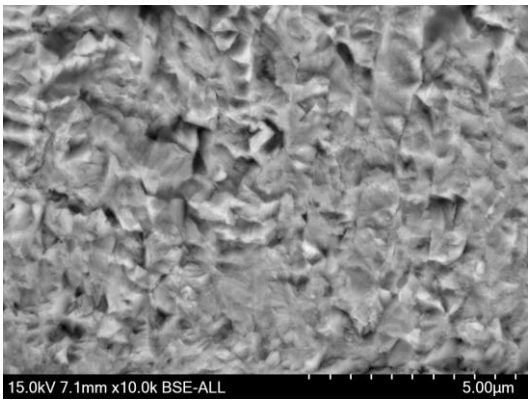

Fig. 3.10 BSE image.

SEM-EDX (Energy Dispersive X-ray Spectroscopy) performs qualitative analysis of a sample by detecting characteristic X-rays generated when the sample is irradiated with an electron beam. Characteristic X-rays have their own energy depending on the element [45].

Electron Backscatter Diffraction (EBSD) is a technique for quantitative microstructure analysis in SEM. EBSD patterns are collected and analyzed to provide a range of sample characteristics including crystal orientation, texture, phase, grain statistics, phase and strain conditions. When the SEM beam strikes a suitably prepared, tilted (at 70°), crystalline sample, Electron Back Scattered Patterns (EBSPs) may be formed. These patterns are recorded on the phosphor screen of the EBSD detector. The EBSD carries the symmetry, orientation, phase and strain information for the point excited by the beam. As EBSPs are generated very near the surface of crystalline samples, it is essential that the surface is free from damage.

3.6 X-ray Fluorescence Film Thickness Meter

The plating film thickness was measured using a fluorescent X-ray film thickness meter (EA6000VX, Hitachi High-Tech Science Corp.). The appearance is shown in Fig. 3.11. Film thickness was measured using a thin film calibration curve, and the average value

measured three times was used as the measured value.

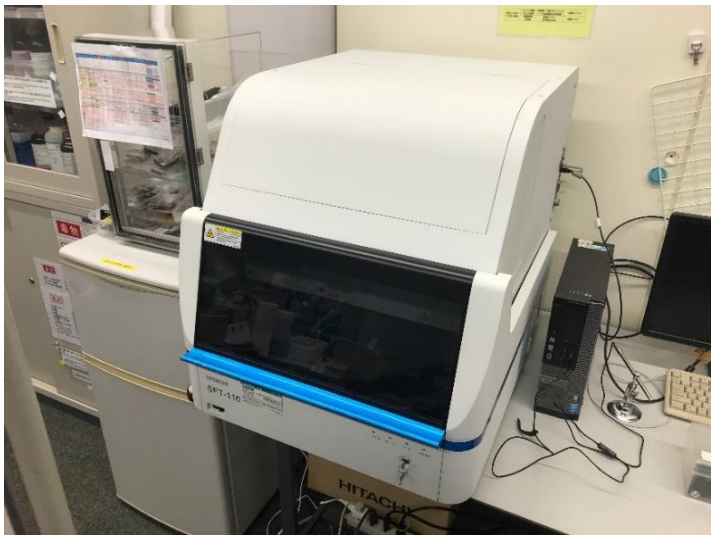

Fig. 3.11 Fluorescent X-ray film thickness meter (EA6000VX).

3.7 Small Vacuum Annealing Furnace

A small vacuum annealing furnace (QF1320-PXDS, Futek Furnace Inc.) was used for the annealing treatment. The appearance of the equipment is shown in Fig. 3.12. The heat treatment was performed at a heating rate of 5 ℃/min and the test atmosphere was vacuum. After holding the heat, the temperature was lowered to room temperature by natural cooling.

Fig. 3.12 Small vacuum annealing furnace (QF1320-PXDS).

3.8 Micro Vickers Hardness Testing Machine

A Vickers hardness test was conducted to investigate how much the hardness changed of Ni plating layer after different temperature fatigue test or annealing in different temperature. A Micro Vickers hardness testing machine (MHT-1, Matsuzawa Seiki Co., Ltd.) was used for the test, and Fig. 3.13 shows the appearance of the machine used. Vickers hardness is one of the measures to investigate hardness, and it is expressed in HV and has no unit. A regular quadrangular pyramid-shaped indenter is pushed into the sample surface, the length of the diagonal line of the indentation remaining is measured after removing the load, and the hardness is calculated from formula (3-4). As can be seen from the calculation formula, the larger the indentation, the smaller the HV, and the

smaller the indentation, the larger the HV. Fig. 3.14 shows indentations on the sample. As shown in Fig. 3.14, 3 indentations were made per sample, and HV was evaluated by the average value. The indenter load was 25 g, and the load application time was 10 seconds.

$$Hv=\text{Load (g)}/\text{ Diagonal mean square of indentation (mm}^2\text{)} *1854.37 \quad (3\text{-}4)$$

Fig. 3.13 Micro Vickers hardness testing machine (MHT-1).

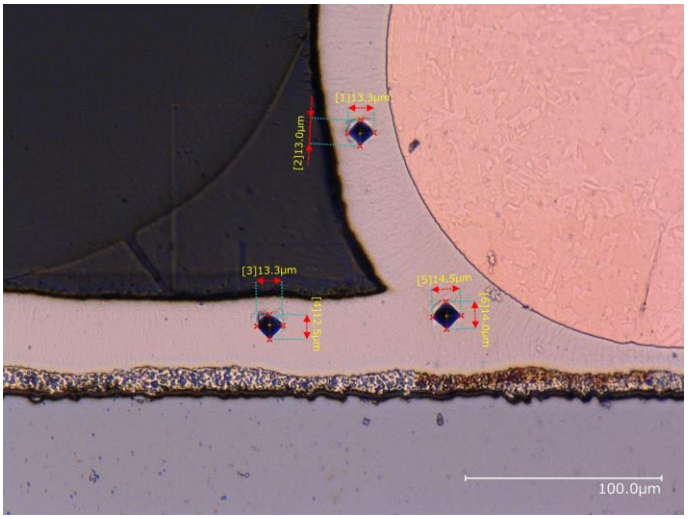

Fig. 3.14 Indentations on the sample.

3.9 pH Meter

In order to control the pH of the plating bath, the pH was measured using a portable pH meter (LAQUAact, HORIBA, Ltd.). Fig. 3.15 shows the appearance of the meter. The calibration was a two-point calibration using standard solutions of 4.01 and 6.88. When the pH changed, a 20% aqueous solution of sulfamic acid or an aqueous solution of nickel carbonate was used to adjust the pH by adding an appropriate amount so as to have an appropriate pH value.

Fig. 3.15 pH meter (LAQUAact).

3.10 Optical Microscope

An optical microscope was used to observe the sample. It was mainly used to measure indentations in the Vickers hardness test and to observe surface of samples. Fig. 3.16 shows the appearance of the optical microscope (VHK-100F, KEYENCE Corp.) used this time.

Fig. 3.16 Optical microscope (VHK-100F).

3.11 Thermal Cycling (TC) Testing Machine

Fig. 3.17 Thermal cycling testing machine (TSA-73ES-W).

In order to evaluate reliability of solar cell, according to IEC 61215, section 10.11,

thermal cycling temperate ranges from -40 ℃to 130 ℃or 150 ℃for 800 or 1000 cycles for accelerating test speed. The appearance of thermal cycling testing machine (TSA-73ES-W, ESPEC, Corp.) is shown in Fig. 3.17.

3.12 Damp Heat (DH) Testing Machine

In order to evaluate reliability of solar cell, based on IEC 61215, section 10.13, DH test was done by damp heat testing machine (PR-1KT, ESPEC Corp.) Condition of DH test is 85°C and 85% relative humidity (RH) for 1000 hours in the environment chamber. Fig. 3.18 shows the appearance of damp heat testing machine.

Fig. 3.18 Damp heat testing machine (PR-1KT).

3.13 Ion Milling System

The ion milling system (IM4000 PLUS, Hitachi High-Tech Corporation) utilizes a broad, low-energy Ar^+ ion beam milling method to produce wider, undistorted cross-section milling or flat milling, without applying mechanical stress to the sample. Flat milling of sample surface or cross-section were done before EBSD observation. Fig. 3.19 shows the appearance of ion milling system.

Fig. 3.19 Ion milling system (IM4000 PLUS).

3.14 Vacuum Reflow Solder Oven

Solar cell interconnected with Cu wire by solder as a comparison target was made by reflow, which using reflow oven (RSS-210-S, UniTemp GmbH Co., Ltd.). Fig. 3.20 shows the appearance of vacuum reflow solder oven.

Fig. 3.20 Vacuum reflow solder oven (RSS-210-S).

3.15 Tensile Testing Machine

Fig. 3.21 Tensile testing machine (AG-X).

The tensile testing machine (AG-X, Shimazu Corp.) was used for sample after resonant fatigue test. In order to observe fracture surface of sample and due to sample didn't totally get break, tensile break need to be added. Fig. 3.21 shows the appearance of tensile testing machine.

3.16 Rotary Drill

The rotary drill (SD-13, Shinko MechatroTech Co., Ltd.) was used for opening a notch in resonant fatigue test sample. Fig. 3.22 shows the appearance of rotary drill.

Fig. 3.22 Rotary drill (SD-13).

3.17 Grinding and Polishing Machine

The grinding and polishing machine (49-7250, Buehler Ltd.) was used for sample observation by SEM. A clear cross-section was necessary especially for EDX. Fig. 3.23 shows the appearance of grinding and polishing machine.

Fig. 3.23 Grinding and polishing machine (49-7250).

3.18 Diamond Wire Saw

The diamond wire saw (CS-203, New Metals and Chemicals Corp.) was used for dividing sample from one whole Cu plate plated with Ni film. This cutting method has less damage to sample. Fig. 3.24 shows the appearance of diamond wire saw.

Fig. 3.24 Diamond wire saw (CS-203).

3.19 Portable Solar Simulator

The portable solar simulator (PEC-L01, Peccell Tech., Inc.) was used for getting photoelectrical properties of solar cell. Open circuit current, short circuit current,

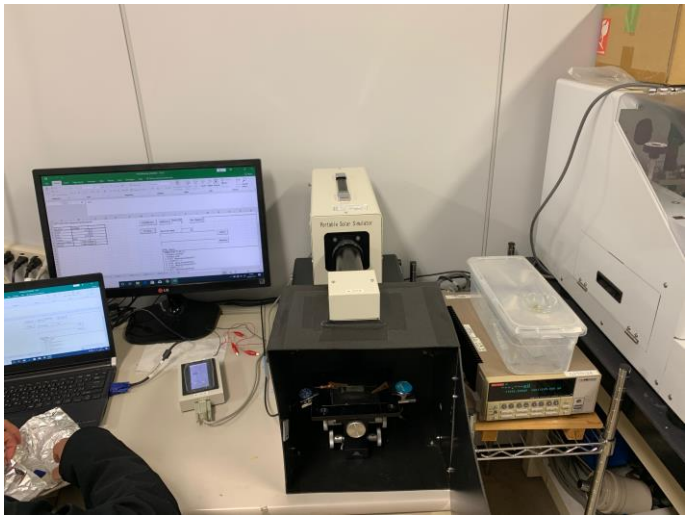

Fig. 3.25 Portable solar simulator (PEC-L01).

efficiency, FF (fill factor) etc. could be directly obtained from software. Fig. 3.25 shows the appearance of portable solar simulator. It contains a black box electrodes stage, a 150 W Shor-arc Xe lamp, a computer and a source meter. Table 3.5 shows specifications of solar simulator.

Table 3.5 Specifications of solar simulator.

Items	**Specifications**
Illumination area	40 mm square
Irradiance	150 mW/cm^2 and higher
Xe lamp	150 W Short-arc Xe lamp
Temperature in use	5~40 ℃(RT)
Humidity in use	20~80% (RH, no condensation)

3.20 Bond Tester

The second generation Nordson DAGE 4000Plus is the most advanced bond tester on the market. With best-in-class performance, the 4000Plus bond tester has become the industry standard for bond strength testing, delivering outstanding data accuracy and repeatability for results you can trust.

Fig. 3.26 shows appearance of the bond tester. The 4000Plus Versatile bond tester can carry out shear test up to 200kg, pull test up to 100kg, and push test up to 50kg for all

testing applications including heated bump pull and micro materials testing. The system also features a camera-assisted automation system ideal for applications such as pull and shear testing of wafer interconnects, lead frames, hybrid microcircuits, automotive electronics packages, and more.

Fig. 3.26 Bond tester (4000Pkus).

Chapter 4: Long-term Reliability of NMPB by Resonant Type Fatigue Test

4.1 Experimental Procedure

In order to investigate fatigue limit of Ni layer of NMPB interconnection, fatigue test was conducted using a resonant type fatigue (RF) testing machine. As the test piece evaluated by RF test, a commercially available 0.3 mm-thick Cu plate (C1100) subjected to NMPB was used for this test. Firstly, a 25×70 mm Cu plate was taken to NMPB plating procedure. Plating time was 90 min. Then the plate was cut to test pieces by wire saw and a notch with a diameter of 0.5 mm was drilled by rotary drill, in order to make stress concentration and promote the initiation of fatigue cracks [41]. Finally, pieces were polished by #2000 sandpaper for deburring. The size of test piece is shown in Fig. 4.1. As the same crystal structure of NMPB semiconductor mounting, Cu plate with double-sided NMPB layer, thickness of which is 0.34 mm, was used as the standard test piece in this study. Further, in order to evaluate the fatigue limit of NMPB, fatigue test was also performed on test pieces obtained by dipping solder on the same Cu plate as a comparison target. The composition of solder used for the solder test piece is Sn-3.0Ag-0.5Cu, which is a kind of lead-free solder often used for semiconductor chip interconnection mounting package. Similar to NMPB test piece, the solder test piece was also double-sided dipped

to 0.34 mm. In this study, fatigue limit was defined with a stress amplitude that could withstand 10^7 repetitions [43].

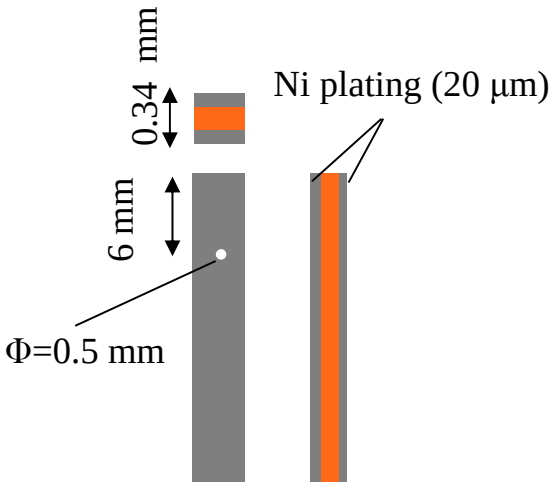

Fig. 4.1 Size of test piece for RF test.

4.2 Results

4.2.1 SW-N Curve

Test pieces were set on RF testing machine and Swing Width (SW)-N curves were obtained as shown in Fig. 4.2. Differs from S-N curve, swing width amplitudes were directly measured by laser displacement meter because the orders of displacements caused by CTE mismatch of different metals are close in TC cycles. However, orders of stress amplitudes are different because they are related to Young's modulus of metals themselves. In RF test machine, stress amplitude is linearly related to swing width amplitude in the same sample. Stress amplitude of different samples in the same condition could also be distinguished by resonant frequency which could be calculated by the following formula (4-1).

$$\text{Resonant frequency (Hz)}=\sqrt{\{E\ (\text{GPa}) / 3.829*10^{-11} / L\ (\text{mm})^4 / \rho\ (\text{g/cm}^3) * T\ (\text{mm})^2\}} \quad (4\text{-}1)$$

Here, E is Young's modulus, L is the length of vibrating part of sample (L is 20 mm in this experiment), ρ is density and T is thickness of sample (T is 0.34 mm in this experiment). Young's moduli of NMPB and solder bonding samples were set in 118.6 GPa and 102.8 GPa, respectively. Stress amplitude at hole position could be automatically calculated by software that was used. For example, when swing width is 0.8 mm, stress

amplitudes at hole position of NMPB sample and solder bonding sample were 214 MPa and 186 MPa respectively. Thus, in order to compare fatigue limits of different samples as a simulation of TC test, swing width amplitude is more suitable than stress amplitude as a parameter.

Test pieces were tested at both room temperature and high temperature. X axis represents cycles number of failure and Y axis represents swing width, which also represents stress amplitude. In Fig. 4.2 (a), red and yellow triangle represent NMPB sample tested at 25 ℃ and 250 ℃, respectively. Green and blue rhombus represent solder bonding sample tested at 25 ℃and 150 ℃, respectively. Fatigue limit of solder bonding is 0.712 mm, and NMPB is 0.775 mm at temperature of 25 ℃. Table 4.1 shows fatigue limits of samples in different conditions which are swing widths at 10^7 cycles as shown in Fig. 4.2.

Table 4.1 Fatigue limits of samples in different conditions.

Fig. 4.2 (a)		Fig. 4.2 (b)	
Samples	**Fatigue limits**	**Samples**	**Fatigue limits**
NMPB 25 ℃	0.775 mm	Cu 25 ℃	0.819 mm
NMPB 250 ℃	0.729 mm	NMPB (Cu 250 ℃annealed)	0.746 mm
Solder 25 ℃	0.712 mm	NMPB (250 ℃ annealed)	0.738 mm
Solder 150 ℃	0.603 mm	Cu 250 ℃ annealed	0.656 mm

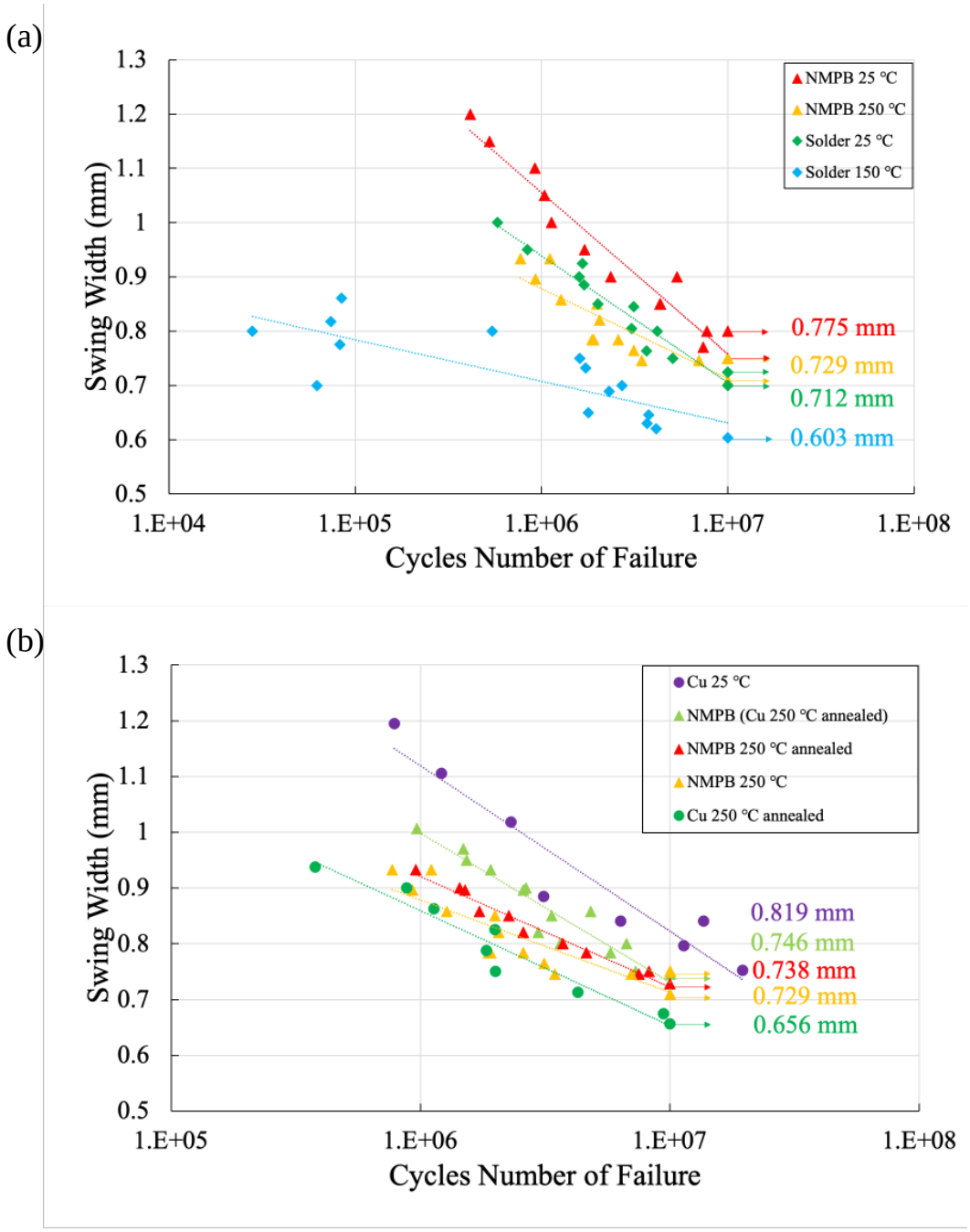

Fig. 4.2 (a) SW-N curves of NMPB at 25 and 250 ℃, solder bonding at 25 and 150 ℃, respectively. (b) SW-N curves of NMPB at 250 ℃considering the influence of base material Cu.

Considering that solder couldn't withstand 250 ℃, lower temperature condition of 150 ℃was set. The results show that fatigue limit of NMPB at 250 ℃is 0.729 mm, slightly decreased by 5.9% from 25 ℃. However, fatigue limit of solder bonding at 150 ℃ decreased by 15.3% from 25 ℃.

Table 4.2 Cycles numbers of failure of samples when swing width is 0.8 mm in Fig. 4.2 (a).

Samples	**Cycles numbers**
NMPB at 25 ℃	$7.70*10^6$
NMPB at 250 ℃	$2.45*10^6$
solder at 25 ℃	$3.50*10^6$
solder at 150 ℃	$0.57*10^6$

On the other hand, the data of Fig. 4.2 could be read in horizontal view. Table 4.2 shows cycles numbers of failure of samples in Fig. 4.2 (a), when swing width is 0.8 mm. These data could be compared to realize differences in cycles numbers of failure of different samples in the same condition. From Table 4.2, cycles number of NMPB at 25 ℃ is $7.70*10^6$ and solder bonding at 25 ℃is $3.5*10^6$. It indicates that life span of NMPB is 2.2 times that of solder bonding at room temperature. Also, cycles number of NMPB at 250 ℃ is $2.45*10^6$ and solder bonding at 150 ℃$0.57*10^6$. It indicates that life span of NMPB is

4.3 times that of solder bonding at high temperature. The conclusion is that NMPB shows higher fatigue limit, and it also means longer-term reliability than solder bonding in RF test.

Considering the influence of base material Cu, test pieces were made as shown in Fig. 4.2 (b). light green and red triangle represent NMPB electroplated on Cu plate annealed at 250 ℃ in vacuum atmosphere for 10 hours sample and NMPB sample annealed at 250 ℃ in vacuum atmosphere for 10 hours respectively, tested at 25 ℃. Purple and green circle represent Cu plate sample and Cu plate annealed at 250 ℃ in vacuum atmosphere for 10 hours sample tested at 25 ℃, respectively. Fatigue limit of Cu decreased obviously after annealed for 10 h at 250 ℃. Also, fatigue limit of NMPB on Cu annealed (10 h at 250 ℃) was 0.746 mm. This means actually NMPB tested at 250 ℃ only decreased 0.017 mm compared with NMPB at 25 ℃. As a conclusion, NMPB in high temperature still has strong fatigue strength which is not inferior to NMPB at room temperature. This would be explained in section 4.2.3.

4.2.2 Vickers Hardness

Test pieces were taken to measure Vickers Hardness to realize changes after annealing at different temperatures. Ni Surface and cross section of test pieces were measured with five points each condition, as shown in Fig. 4.3.

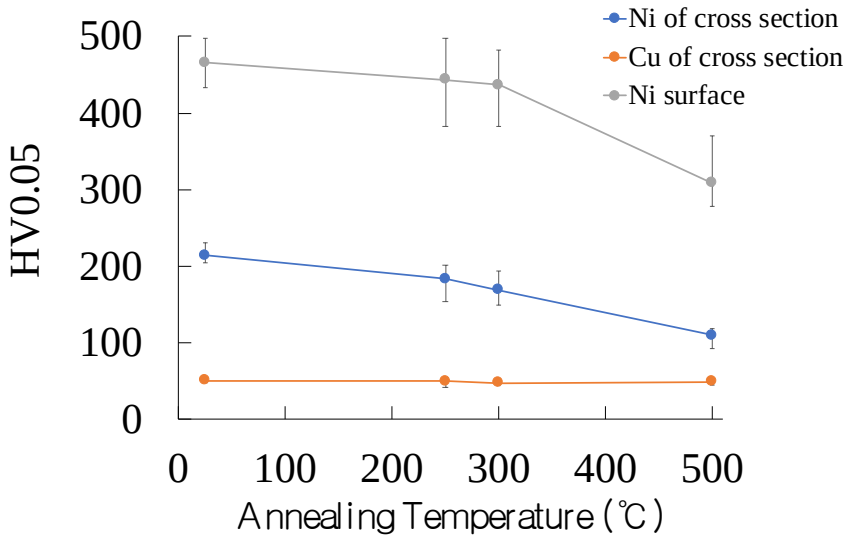

Fig. 4.3 Vickers hardness of test pieces, all annealing conditions.

From Fig. 4.3, hardness of Cu of cross section didn't change obviously, Ni surface and Ni of cross section decreased as annealing temperature increasing. This means recovery and recrystallization happened in Ni layer and made fatigue limit decreased comparing to initial pieces. However, NMPB still maintained enough high fatigue limit even annealed in high temperature.

4.2.3 SEM Observation of Crack Growth and Fracture Surface

Fig. 4.4 and Fig. 4.5 show SEM images of crack growth and fracture surface respectively, for each condition. As described in section 4.1, notch was introduced to make stress concentration and the results of Fig. 4.4 show that crack always grew from the middle

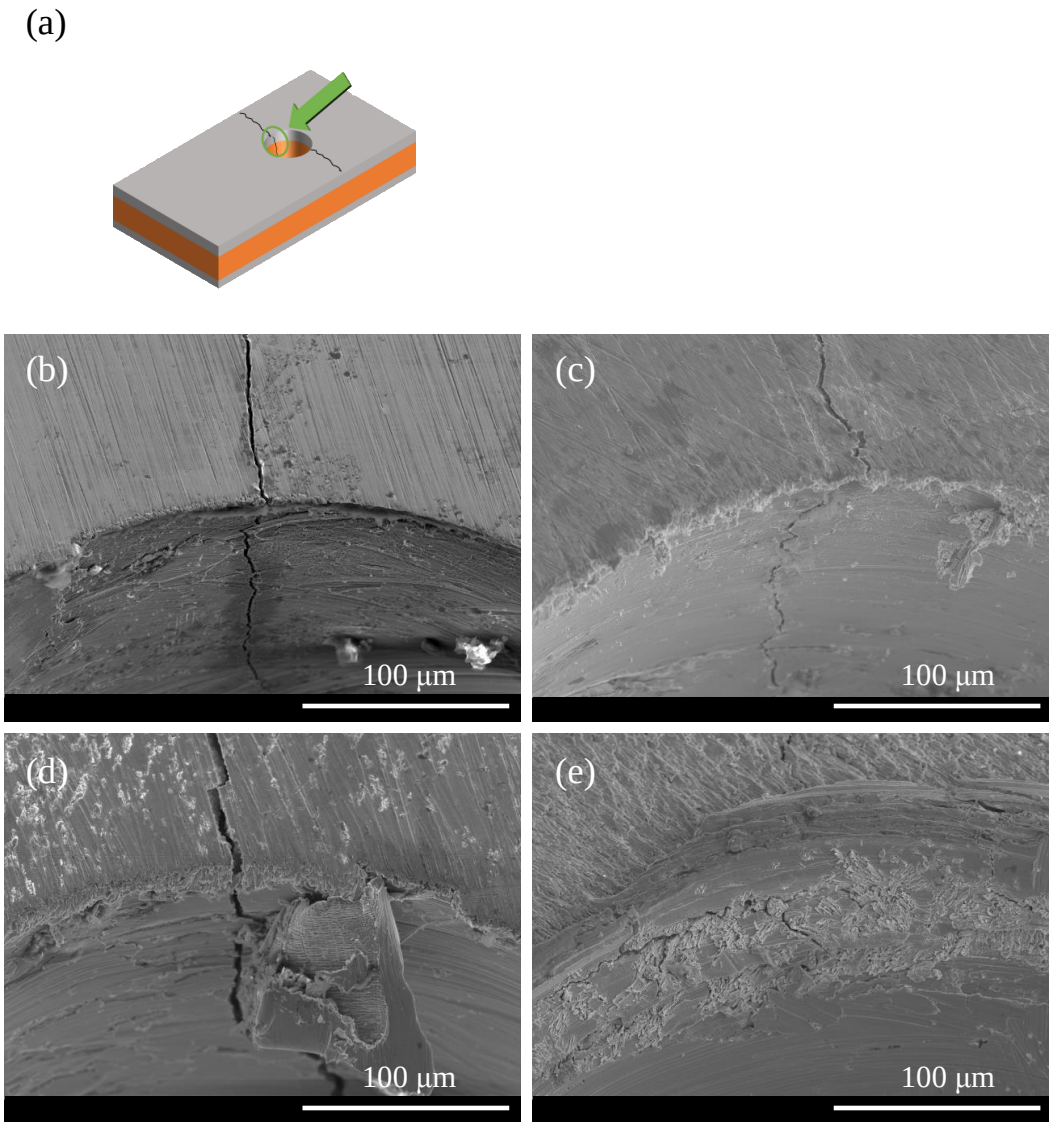

Fig. 4.4 Crack observation by SEM, (a) schematic diagram of observation angle. NMPB at (b) 25 ℃, (c) 250 ℃. Solder bonding at (d) 25 ℃, (e) 150 ℃.

edge of notch. In NMPB, crack grew in one direction practically perpendicular to notch both at 25 ℃and 250℃. However, in solder bonding, crack growth was divided to random directions at 150 ℃. As a result, several cracks happened and caused decrease of fatigue limit.

Fig. 4.5 (a) shows that after RF test, the test piece was broken by tensile failure in up-down direction for fracture surface observation. Fig. 4.5 (b) ~ (e) show that fracture surface of NMPB didn't change much from 25 ℃to 250 ℃. However, in solder bonding, voids which are closed to interface grew up in solder phase. Combining results of Fig. 4.4 and 4.5, due to diffusion between Cu and solder, voids occurred in solder phase. Voids caused additional cracks in RF test. Eventually, it resulted in decrease of fatigue limit. Considering low melting point of lead-free solder (230 ℃), when temperature ran over 60% of melting point (Kelvin temperature) [46], creep happened in solder bonding at 150 ℃and led to obvious fatigue limit decrease. From Q.K. Zhang et al., it could also be explained that several cracks occurred at high temperature resulted from creep fatigue in particular [47]. And in NMPB, slower diffusion speed contributed to high-heat-resistant interconnection and voiding does not occur. This would also be discussed in section 4.2.4 by EDX analysis.

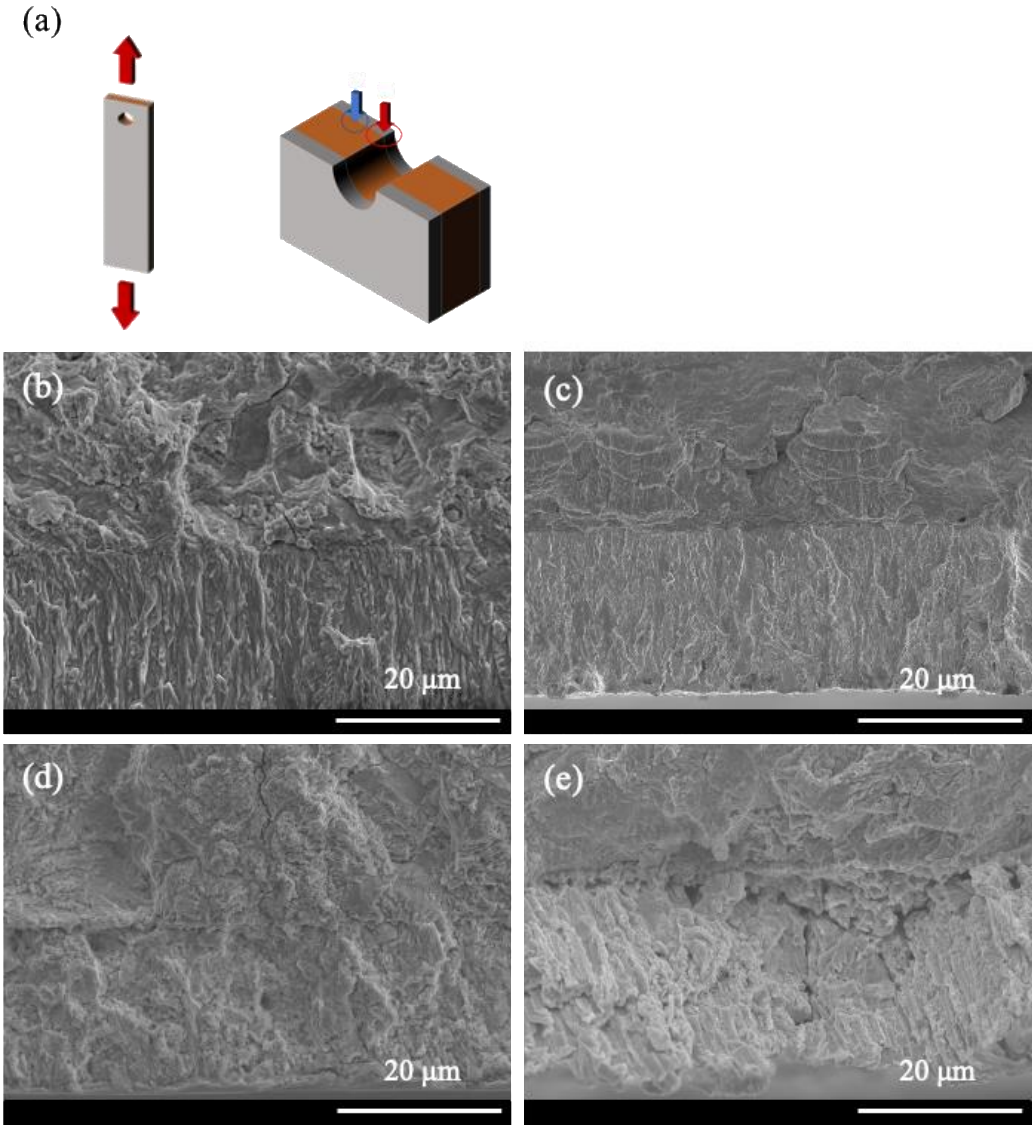

Fig. 4.5 Fracture observation by SEM, (a) schematic diagram of fracture observation. NMPB at (b) 25 ℃, (c) 250 ℃. Solder bonding at (d) 25 ℃, (e) 150 ℃.

4.2.4 EDX Results of Diffusion in Interface

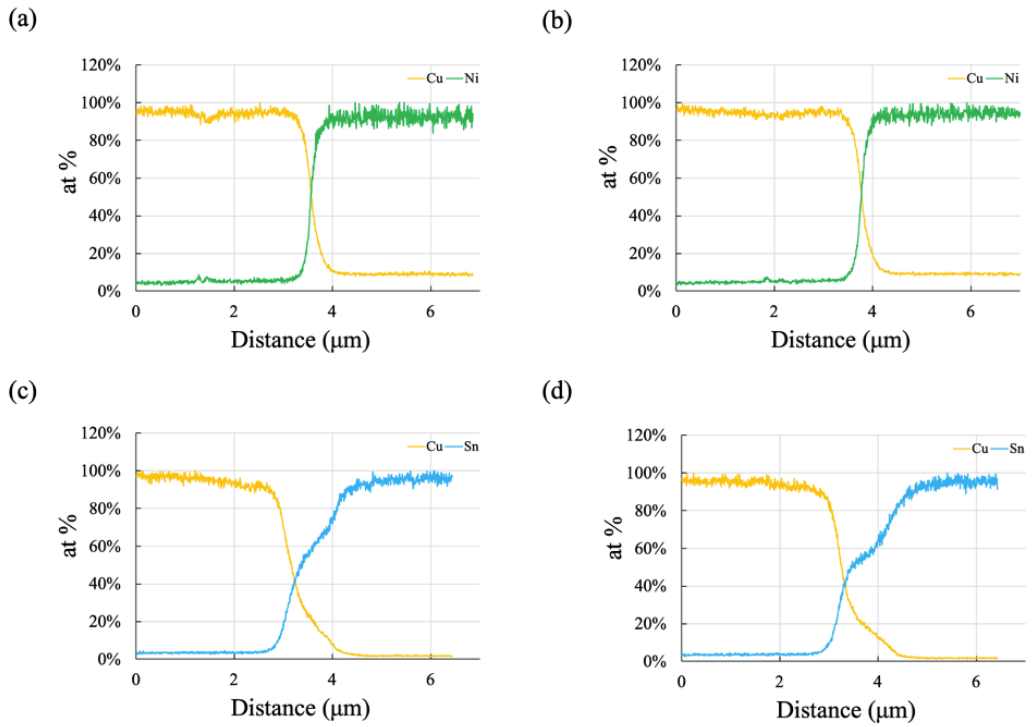

Fig. 4.6 EDX results of NMPB at (a) 25 ℃, (b) 250 ℃. Solder bonding at (c) 25 ℃, (d) 150 ℃.

In this section, EDX is used to analyze diffusion layer. Atomic percent was calculated from counts which related to energy of characteristic X-rays emitted by electrons. Characteristic X-rays have energy unique to each element, so elemental analysis can be performed by measuring EDX. In Fig. 4.6 diffusion information was plotted by distance versus atomic percent. For metals, the temperature dependence of the diffusion coefficient D is expressed as follows:

$$D = D_0 \exp(-Q/RT)$$

(4-2)

Here, D_0 is the frequency factor, Q is the activation energy of diffusion and R is the gas constant. Diffusion length could be compared referring to D. D of each sample is shown in Table 4.3.

Table 4.3 Diffusion coefficients of Ni and Sn in Fig. 4.6.

Samples	D_0 **(m^2/s) [48]**	Q **(J/mol) [48]**	**Diffusion coefficients (m^2/s)**
Ni (Ni/Cu) 25 ℃	$6.1*10^{-5}$	$2.55*10^{5}$	$1.16*10^{-49}$
Ni (Ni/Cu) 250 ℃	$6.1*10^{-5}$	$2.55*10^{5}$	$2.01*10^{-30}$
Sn (Sn/Cu) initial	$2.4*10^{-7}$	$3.31*10^{4}$	$1.18*10^{-10}$
Sn (Sn/Cu) 25 ℃	$2.4*10^{-7}$	$3.31*10^{4}$	$3.76*10^{-13}$
Sn (Sn/Cu) 150 ℃	$2.4*10^{-7}$	$3.31*10^{4}$	$1.95*10^{-11}$

Here, R is the value of 8.31 $J \cdot K^{-1} \cdot mol^{-1}$. D_0 and Q is the data of diffusion experiment that Ni or Sn is the main element and Cu is diffusion element [48]. The diffusion conditions of Fig. 4.6 are not exactly the same, and Table 4.3 is just a reference for comparing the diffusion distance of Cn/Ni or Cu/Sn interface. From Table 4.3, diffusion coefficient of Sn initial is $1.18*10^{-10}$ m^2/s, sample condition of which is immediately after reflow process. Even reflow process continued only several minutes, reflow temperature of

250 ℃ is high enough that most diffusion of Fig. 4.6 (c) comes from it. Furthermore, diffusion coefficient of Sn is $3.76*10^{-13}$ (25 ℃) and $1.95*10^{-11}$ m^2/s (150 ℃), and Ni is $1.16*10^{-49}$ (25 ℃) and $2.01*10^{-30}$ m^2/s (250 ℃). Diffusion length of Sn (Cu/Sn) was much longer than Ni (Cu/Ni) at 25 ℃ mainly resulted from reflow process. Furthermore, increase of diffusion length of Sn is several orders of magnitude longer than Ni from room to high temperature.

Diffusion layer of NMPB had no obvious change from 25 ℃ to 250 ℃ because Ni has barrier layer in interface of Cu/Ni, the presence of barrier layer prevented Cu from diffusing into Ni. On the other hand, solder bonding had thick initial diffusion layer because of high temperature bonding process and diffusion layer subsequently increased at 150 ℃. The increase of diffusion layer is considered to be the second reason for decrease of fatigue limit. This also explained why voids grew in solder layer near interface, which is a common disadvantage of lead-free solder at elevated temperature.

Furthermore, interface between Cu and Sn has different gradients especially at 150 ℃ which are consider having Intermetallic Compound (IMC) layer of Cu_6Sn_5. Fig. 4.7 shows the binary phase diagrams of Sn-Cu and Sn-Ag [49]. Cu_6Sn_5 IMC layer could be found as η phase in Sn-Cu phase diagram. Ag_3Sn IMC layer could be found as ε phase in Sn-Ag phase diagram. However, it wasn't observed in Cu/Ni interface and means there is

no IMC layer between Cu and Ni. Sn-Ag phase diagram will be used in section 5.2.5.

(a)

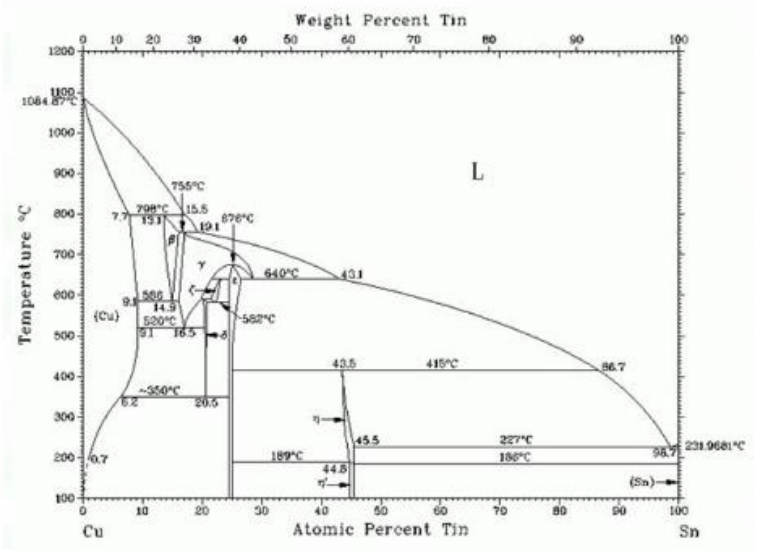

(b)

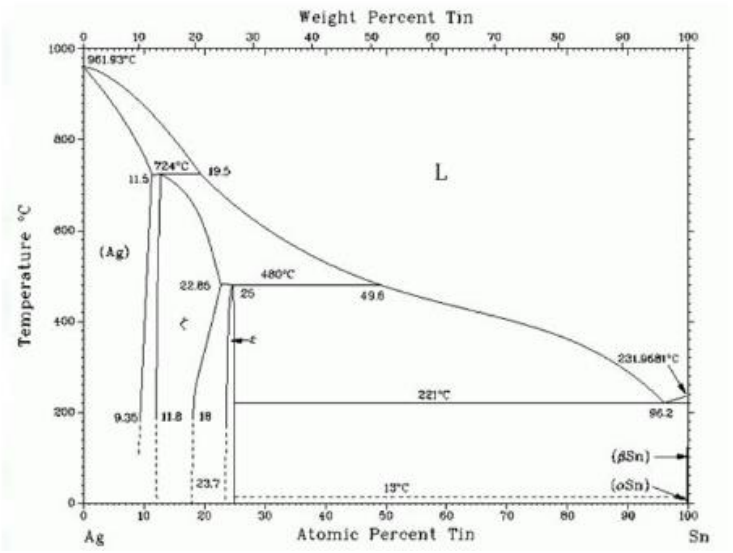

Fig. 4.7 Binary phase diagrams of (a) Cu-Sn and (b) Ag-Sn [49].

4.2.5 Cracking Mode Analysis

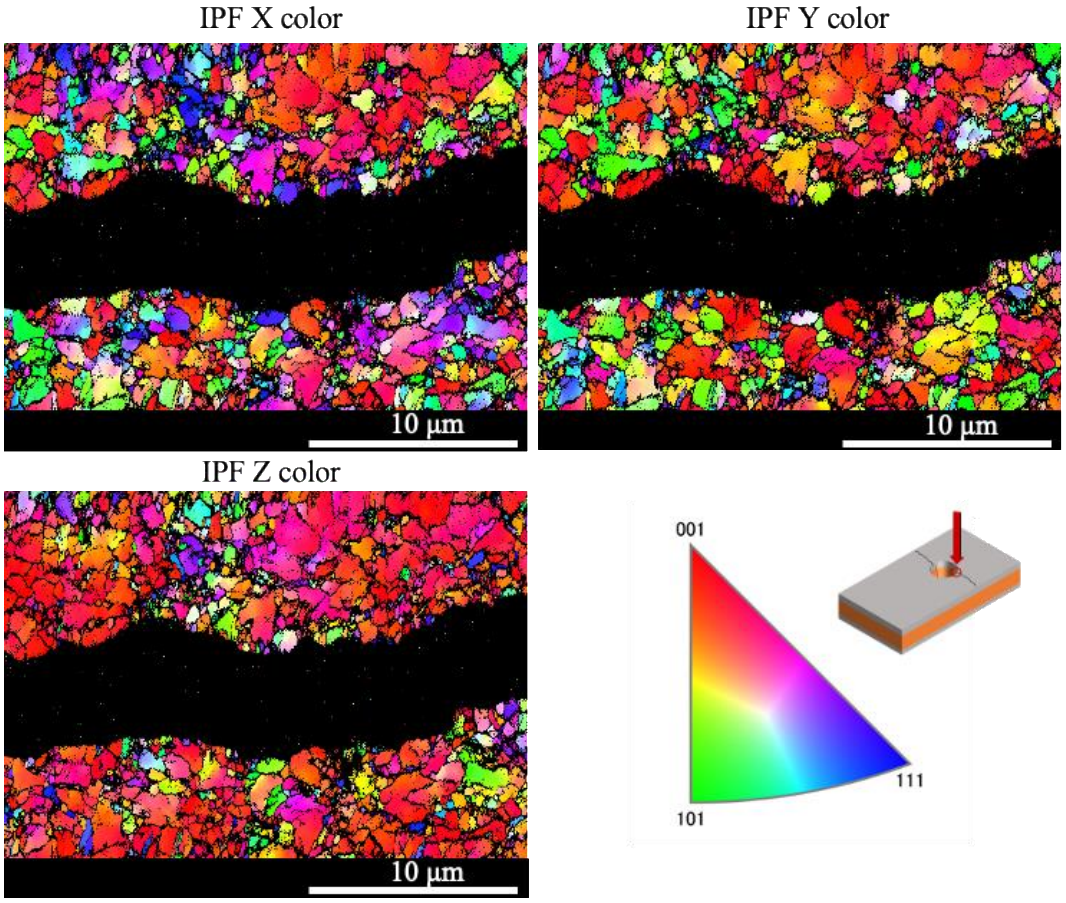

Fig. 4.8 EBSD result of 25 ℃test piece from surface view.

In order to realize change in cracking mode from 25 to 250 ℃of NMPB test piece, EBSD observation was made. Crystal orientations from the surface view of NMPB at 25 ℃ shown in Fig. 4.8. Since NMPB is micro size columnar crystal perpendicular to substrate [13], cracking mode could be judged from surface view of crack propagation. From image IPF Z, crystal orientation is aligned in Z direction, which is <001>. And combining image

IPF X and Y, crack occurred in grain boundary of different orientation crystals. This indicates that cracking mode of NMPB at 25 ℃is intergranular cracking (IGC).

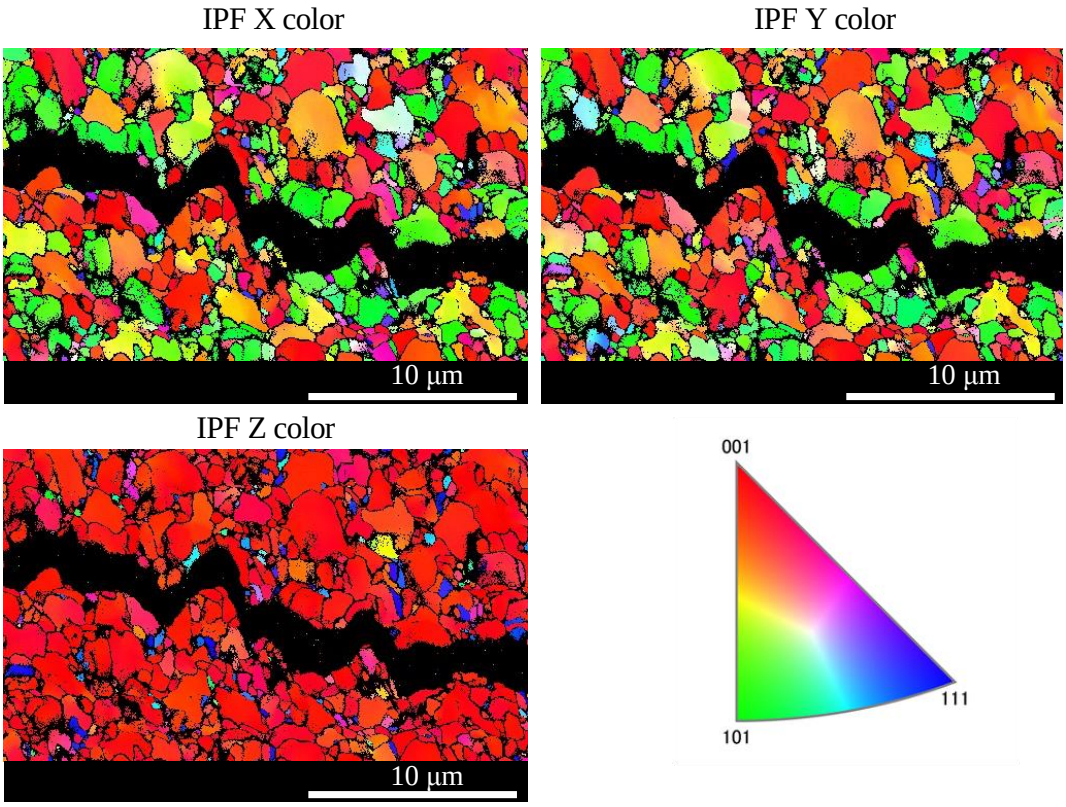

Fig. 4.9 EBSD result of 250 ℃test piece from surface view.

On the other hand, as shown in Fig. 4.9, image IPF Z, crystal orientation still is aligned in <001> event though recrystallization happened at 250 ℃. Also, combining IPF X and Y, cracking mode is mixed by intergranular cracking and transgranular cracking (TGC).

Furthermore, fracture surface and EBSD result of NMPB at 25 and 250 ℃are shown in Fig. 4.10. Combining crystal orientation of fracture surface, from Fig. 4.10 (a), only

intergranular ductile striations were observed in 25 ℃ test piece. However, both intergranular and transgranular ductile striations were observed in 250 ℃ test piece [50, 51], as shown in Fig. 4.10 (b). As a result, cracking mode of NMPB changed from IGC to IGC and TGC mixture.

At room temperature, initial NMPB test piece shows high grain boundary energy and crack propagation direction is always along grain boundary. At high temperature, because recrystallization helped reduced grain boundary energy, crack is more likely to happen inside crystal. Considering the fatigue test result of NMPB at room and high temperature, it can be concluded that cracking mode change maintained NMPB a high fatigue strength.

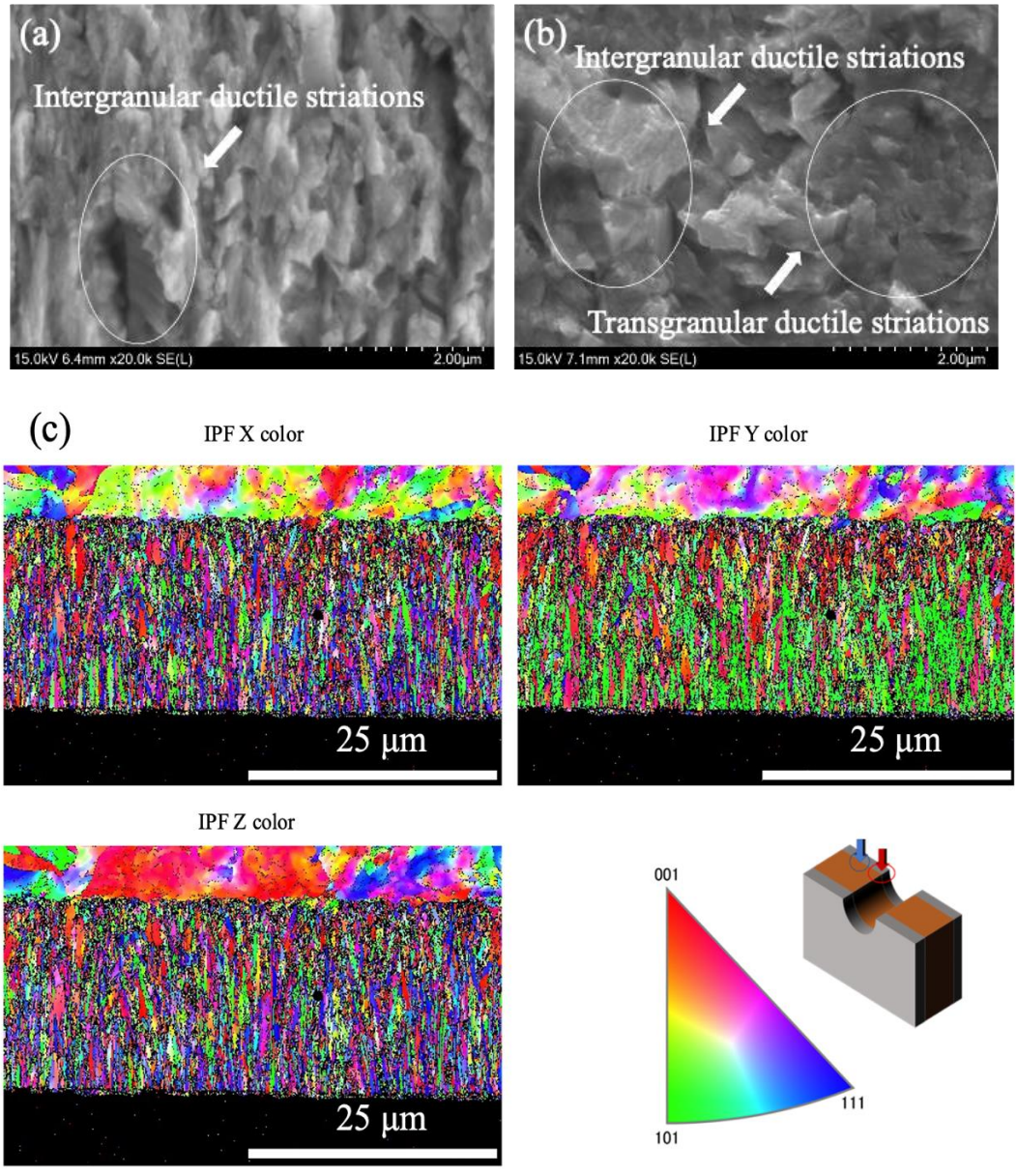
(a)
Intergranular ductile striations
15.0kV 6.4mm x20.0k SE(L)
2.00μm
(b)
Intergranular ductile striations
Transgranular ductile striations
15.0kV 7.1mm x20.0k SE(L)
2.00μm
(c)
IPF X color
IPF Y color
IPF Z color
25 μm
25 μm
25 μm
001
111
101

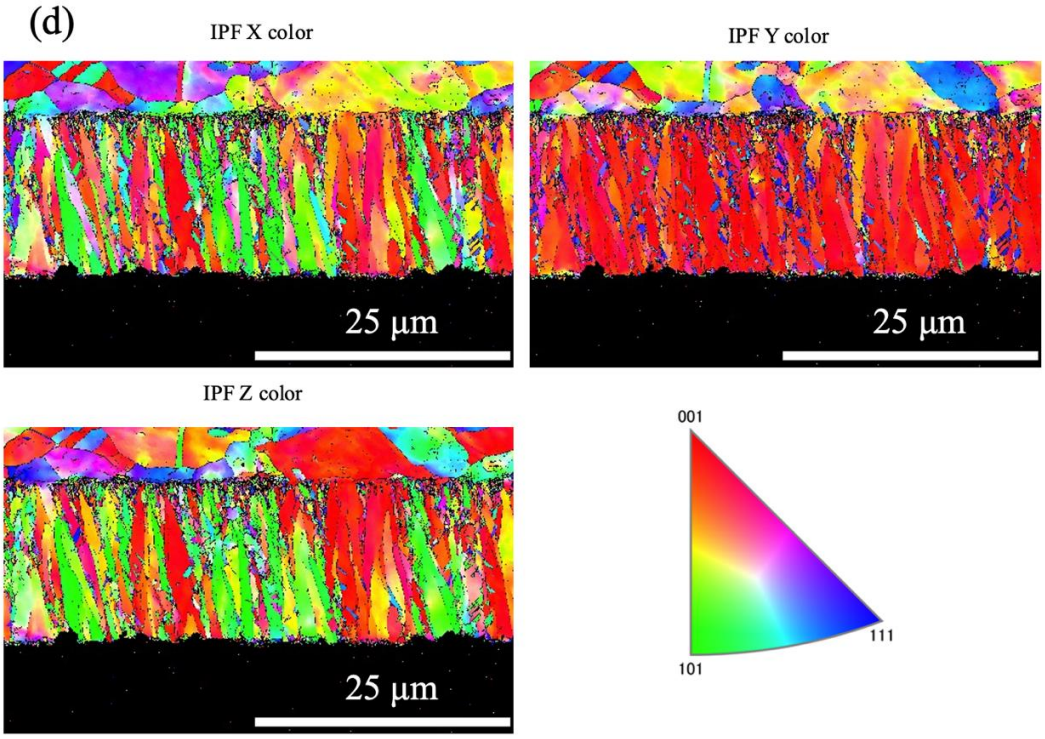

Fig. 4.10 Fracture surface of (a) 25 ℃(b) 250 ℃test piece. EBSD of fracture surface (c) 25 ℃(d) 250 ℃test piece.

4.3 Discussion

Blue square in Fig. 4.11 shows SW-N curve of fine grain Ni plating layer, which was made in the same method as NMPB except adding 10 ml/L stress relaxant in plating solution. This group of tests are set to find out how different the fatigue strength of NMPB is comparing to fine grain Ni. The results show that fatigue limit of fine grain Ni is 0.796 mm. In high cycle area, fatigue strength of NMPB is lower than fine grain Ni, however, higher in low cycle area.

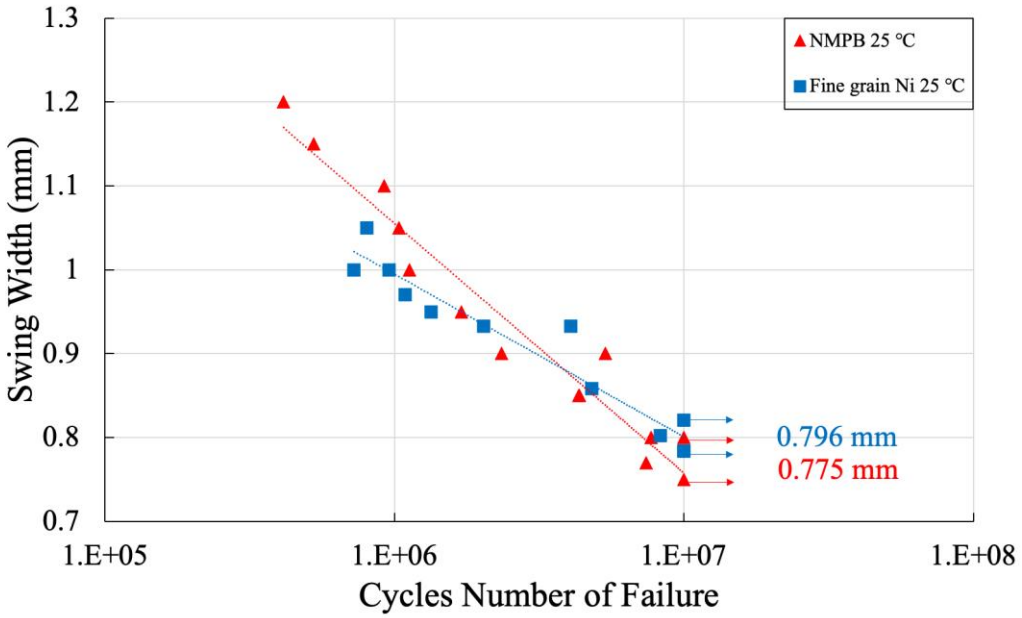

Fig. 4.11 SW-N curve of NMPB and fine grain Ni at 25 ℃

Fig. 4.12 shows BSE (Back Scattered Electron) images of (a) cracking surface and (b)

fracture surface of fine grain Ni. Submicron grains were observed, and they were classified as fine grains. Fine grain strengthening makes fatigue limit of fine grain Ni higher than NMPB in high cycle area. However, compared with results in Fig. 4.8, in low cycle area, <001> and <101> texture makes NMPB has higher Young's modulus and yield stress.

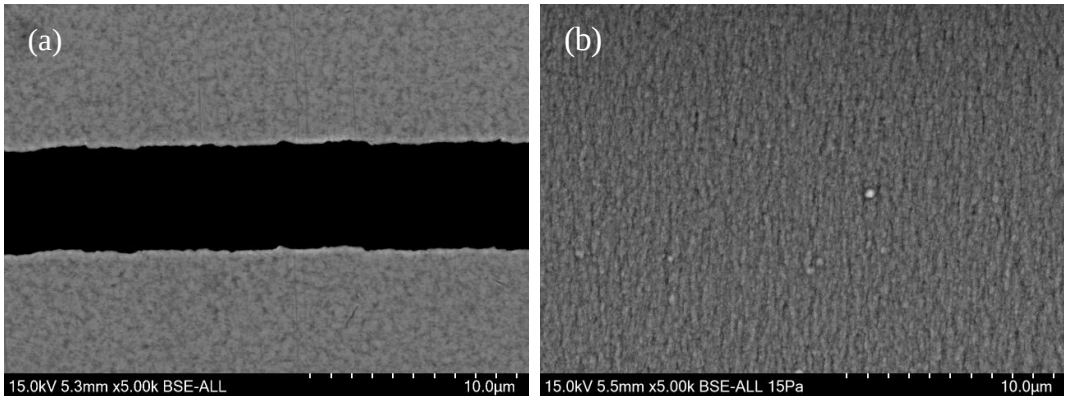

Fig. 4.12 BSE image of cracking surface and fracture surface, fine grain Ni.

4.4 Conclusions

1. Compared with lead-free solder bonding, NMPB has absolutely higher fatigue limit both in room temperature and high temperature.

2. Fast diffusion caused voids in solder bonding at 150 ℃, which was not found in NMPB at 250 ℃, and directly led to decrease of fatigue limit, as well as creep fatigue did in RF test.

3. Cracking mode of NMPB changed from IGC (25 ℃) to IGC and TGC mixture (250 ℃). Recrystallization helped reduce energy between grain boundary and kept strong fatigue strength of NMPB in high temperature.

4. This experiment demonstrated that nickel micro-plating bonding technology could be considered to have adequate potential as a practical, simple mounting technology that is highly heat-resistant and ensures long-term reliability, by evaluation of fatigue limit.

Chapter 5: Improvement of Reliability on Crystalline Silicon Solar Cell Interconnected by NMPB Technology

5.1 Experimental Procedure

5.1.1 Solar Cell

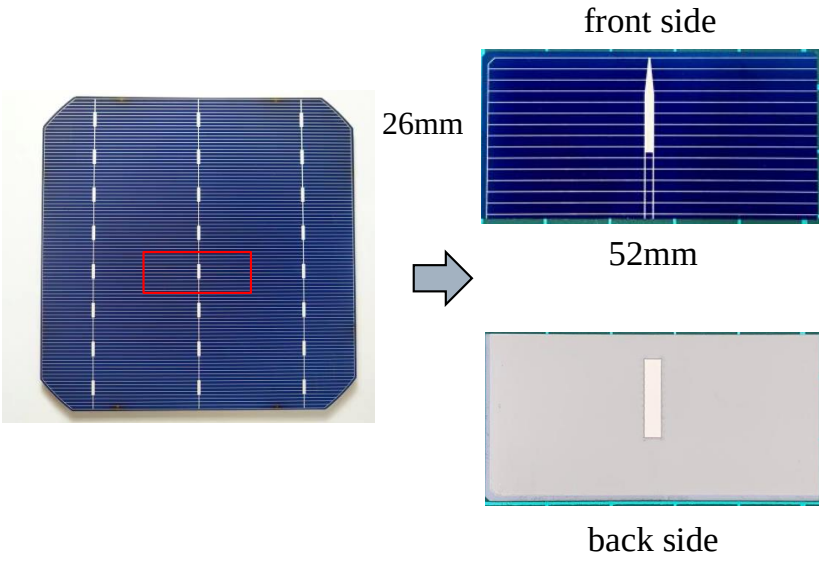

Fig. 5.1 Solar cell piece used in experiment.

Fig. 5.1 shows a piece of 52*26 mm solar cell which was cut from 156*156 mm original multicrystalline silicon (multi c-Si) solar cell (SULE Solar Co., Ltd.) with dash line Silver (Ag) busbar. The typical characteristics of the cells at light intensity of one sun were, approximately, as follows: open circuit voltage (Voc): 0.59 V; short circuit voltage (Isc): 403.9 mA; fill factor (FF): 0.75; and conversion efficiency: 17.5%.

Fig. 5.2 (a) shows 52*26 mm solar cell interconnected by NMPB with Cu wire whose diameter is 0.3 mm. The part in the center of solar cell is Ag busbar and the thin silver lines covering whole Si substrate surface are Ag fingers, function of which is collecting photoelectrons to Ag busbars. Fig. 5.2 (b) shows cross section image of NMPB interconnection on solar cell. Straight Cu wires were fixed to Ag busbars on both sides of Si substrate and two Ni layers grew from Ag and Cu surfaces in the meantime. Eventually two layers in the gap perfectly met to format bonding. Width of Ag busbar on front surface is 1.8 mm and back side is 2.0 mm, which are interconnected in the same method. It was revealed that in the development of next generation silicon heterojunction (HTJ) solar cells, Ag could be replaced by Cu plating electrode mainly due to soaring price of silver [52]. Other papers reported that Ni/Cu plating is also an alternative method for new solar cell electrode [53, 54]. Since reliability of Ni-Cu interface has been demonstrated [55], it is highly possible to apply NMPB to solar cell electrode with plating methods. 5 cells were put into one group to test procedure. A group of solar cells that interconnected with the same cooper wire by lead free solder (Sn-3.0Ag-0.5Cu) in the method of reflow, were also tested as control group. Due to Ag finger would also be electroplated, the whole cell was covered by insulating tape except Ag busbar during NMPB plating process in order to control variables comparing to solder bonding method.

As the technology developed, bifacial PV modules which are widely promoted all over the world, are provided with prevention of moisture immersion, influence of ethylic acid coming from ethylene-vinyl acetate (EVA) sheet become extremely slow [56]. It was also revealed that replaceable encapsulant materials without releasing acid into modules during long outside exposure are quite essential for highly reliable modules [57]. On the other hand, reliability tests on crystalline Si photovoltaic modules without encapsulant have proved that it is possible to produce PV modules without EVA sheet [58]. As a result, EVA sheet and further lamination were not conducted in this study for promising applications in the future. Both NMPB and solder bonding cells weren't encapsulated by EVA sheet, tempered glass and PET back sheet in order to accelerate test speed.

It was reported that fatigue crack growth in silicon wafer [59] and broken Ag finger [60] during thermal cycling test also cause slight degradation of solar cell. Moreover, Corrosion of Al rear electrode also has an impact on output power degradation [61]. As a result, degradation comes from cell itself was considered in this paper and controlled variable ensured the data's accuracy in comparison.

(a) 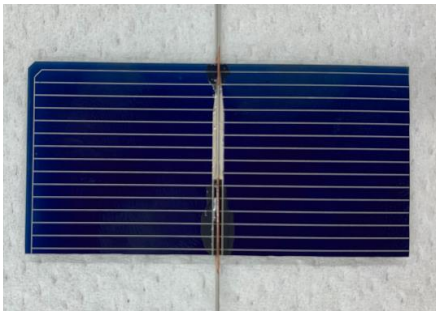 (b) 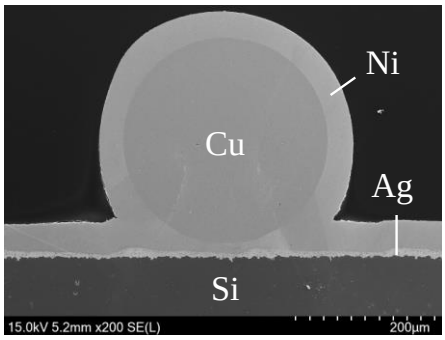

Fig. 5.2 (a) NMPB interconnected solar cell sample.

(b) cross section of NMPB.

5.1.2 Copper Wire

Cross section of Conventional copper ribbon is shown in Fig. 5.3 (a). Since ribbon type interconnection is not suitable for electroplating due to there are no gaps for plating solution flow into, copper wire type interconnection was chosen, as shown in Fig. 5.3 (b). On the other hand, wire type interconnection could also reduce Ag busbar area, so that it increases light absorption. J. Walter et al. reported that wire type interconnection is a simple and evolutionary concept to lower the cost of PV modules by reducing silver consumption for the front side metallization [63]. A. Faes et al. also reported that by replacing standard busbars and ribbons, copper wires without Ag busbar increased efficiency by lowering ohmic losses and enable fine-line printing, reduced consumption

of silver by 85% or more and enhanced module reliability [64].

Differently, traditional interconnection methods would be totally replaced not only by using Cu wires, but also using NMPB technology for increasing reliability of PV modules in this study.

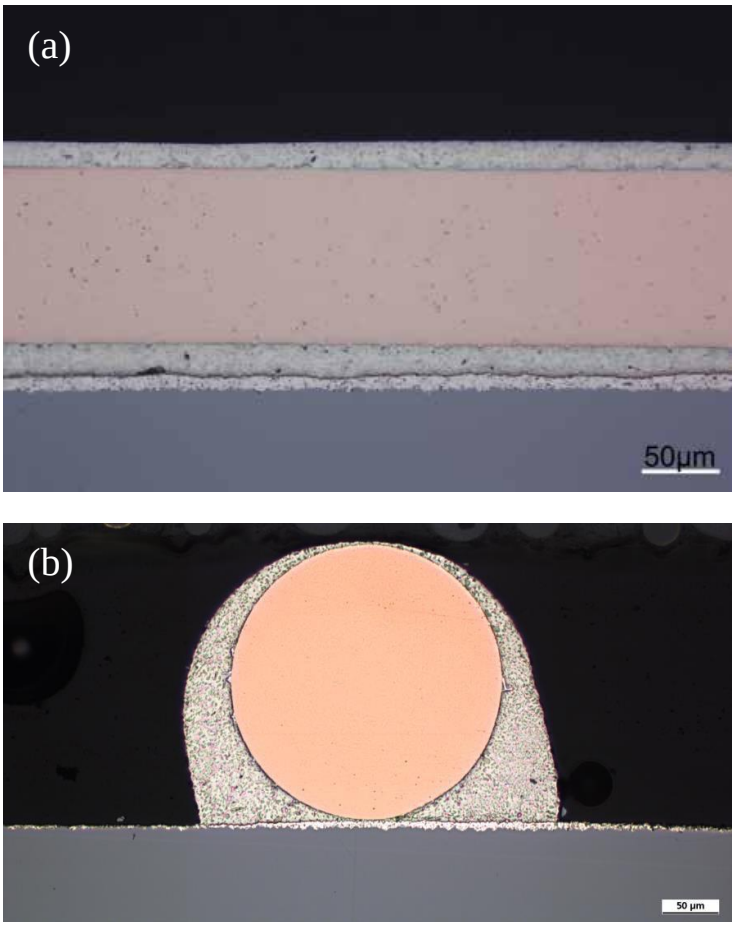

Fig. 5.3 Cross section of (a) copper ribbon type interconnection [62].

5.2 Thermal Cycling (TC) Test

5.2.1 IEC 61215 Standard of TC Test

In IEC 61215 standard 2005, TC test was defined as follow.

10.11 Thermal cycling test

10.11.1 Purpose

To determine the ability of the module to withstand thermal mismatch, fatigue and other stresses caused by repeated changes of temperature.

A test of 1000 TC cycles is considered equivalent to approximately 30 years of outdoor testing.

5.2.2 Experimental Procedure

The first test is thermal cycling (TC) test, conditions of which are shown in Fig. 5.4. Conditions of TC test were obtained in the environmental chamber (TSA-73ES-W, ESPEC Corp., Japan). Based on section 10.11 in the standard 61215 of the International Electrotechnical Commission (IEC 61215), thermal cycling temperate ranges from -40 ℃ to 150 ℃ for 1000 cycles in order to accelerate test speed. An accelerated test is possible because it is the same activation process as the phenomenon that regulates diffusion in different temperatures. For metals, temperature dependence of the diffusion coefficient *D* is expressed as follows [65]:

$$D = D_0 \exp(-Q/RT)$$

Here, D_0 is frequency factor, Q is activation energy of diffusion and R is gas constant. The electrical performance of each sample was measured at every 200 cycles by using a solar simulation system (PEC-L01, Peccell Technologies, Japan). The standard test conditions consist of: (a) irradiance: 1000 W/m^2, (b) cell temperature: 25°C, and (c) spectral distribution of irradiance: AM 1.5G (IEC 60904-3).

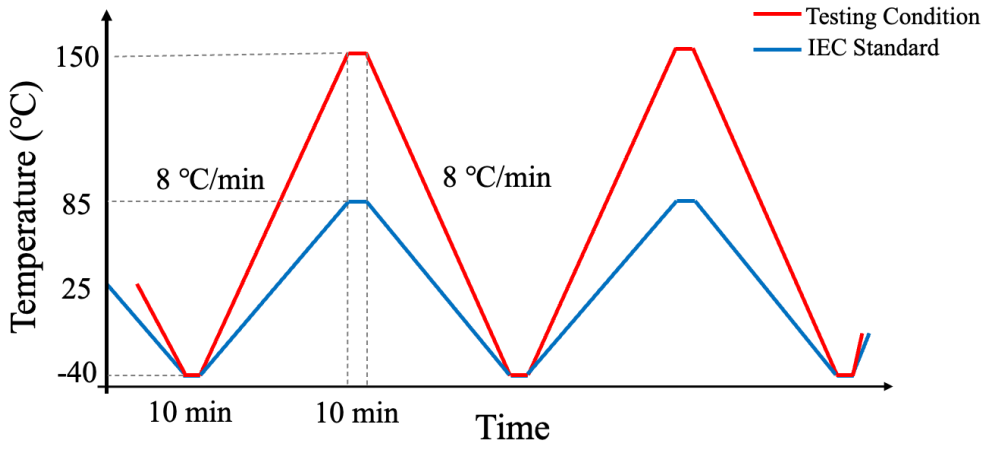

Fig. 5.4 Condition of TC test based on IEC 61215.

5.2.3 I-V Curves and Degradation

Typical I-V curves were obtained as shown in Fig. 5.5 (a) NMPB and (b) solder bonding. Obvious degradation was confirmed in solder bonding cells and NMPB cells kept excellent quality even after 1000 cycles finished. Fig. 5.6 (a) shows more details of

average max output power (P_{max}) of 5 cells every 200 cycles comparing to initial condition. The results of (b) show that P_{max} of solder bonding cells decreased 64.7% when 1000 cycles test finished. However, there was only 1.9% decrease in NMPB cells after 1000 cycles. Because of CTE mismatch between interconnection metal and silicon wafer, stress and creep strain would have a big influence on interconnection bond. In screen printing process of solar cell fabrication, Ag busbar was sintered with Ag paste. Porous and

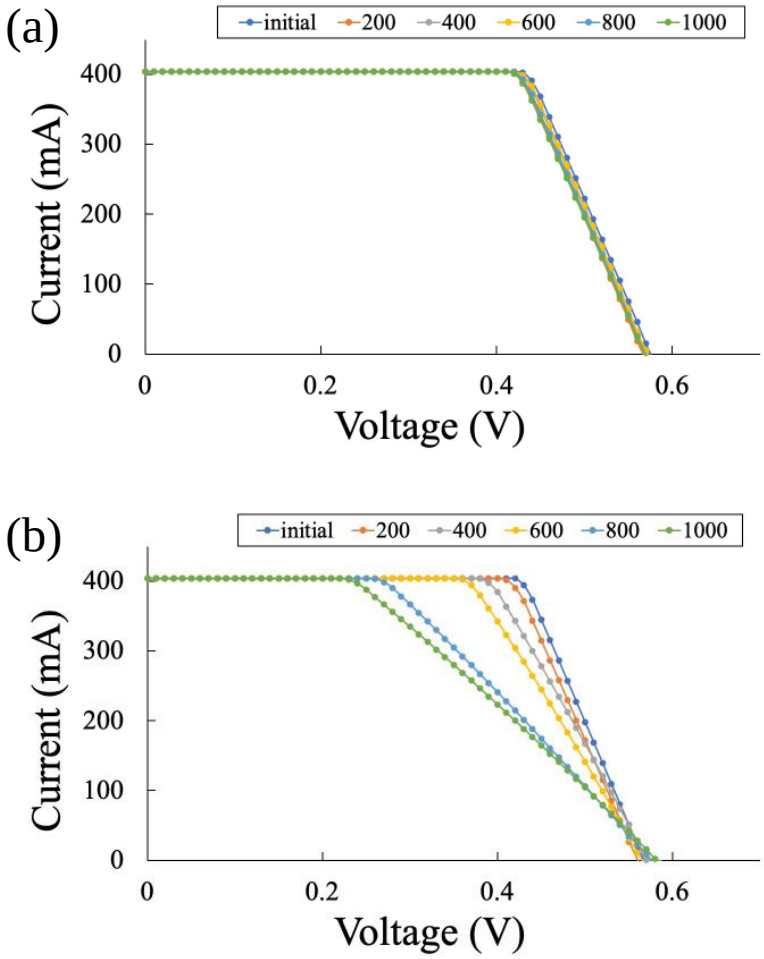

Fig. 5.5 Typical I-V curve of (a) NMPB, (b) solder bonding during 1000 TC cycles.

uneven Ag busbar layer was a result of consideration of interests. In Fig. 5.6, the large margin of error bars in solder bonding samples is considered coming from porous and uneven thickness of Ag busbar. Porous and thick Ag busbar layer formed thick IMC layer and strong stress resulted in weak bonding.

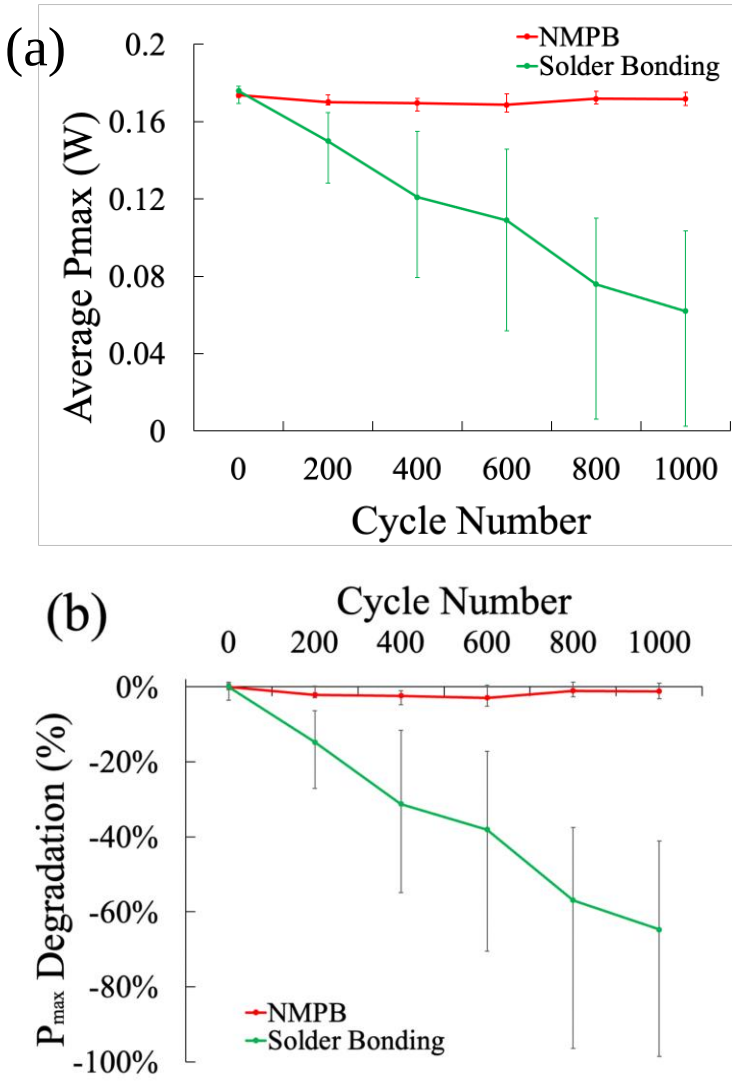

Fig. 5.6 (a) Average P_{max} and (b) P_{max} degradation of each 200 cycles.

5.2.4 Cross Section Observation by SEM

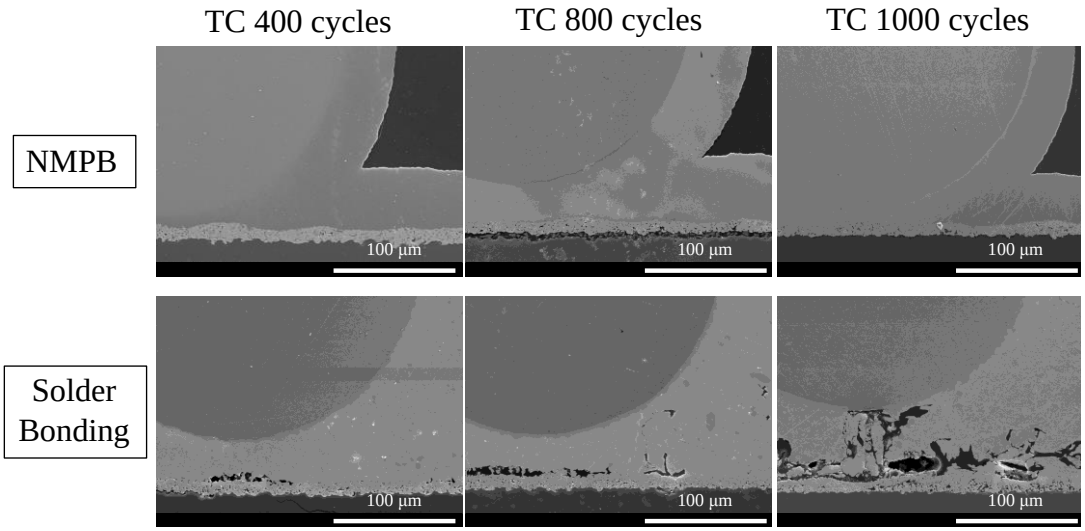

Fig. 5.7 Cross section of NMPB and solder bonding samples at 400, 800 and 1000 TC cycles.

Fig. 5.7 shows SEM cross section image of NMPB and solder bonding on solar cell each TC cycles. Until 1000 cycles, NMPB didn't have any voids or cracks, and combine Pmax data in Fig. 5.6, it kept excellent performance comparing to initial condition. However, voids and cracks appeared at 400 cycles in solder bonding samples. Further, cracks grew at 800 and 1000 cycles inside solder, which led to large degradation that Cu wire was already peeled from Si substrate and cell almost failed. The cracks are considered to appear in the vicinity of solder and Ag interface along the grain boundary of solder [66]. It is suggested that cracking of solder interconnections under thermomechanical loadings

is enhanced by the recrystallization, because the network of newly formed grain boundaries extending through the interconnections provide favorable paths for cracks to propagate intergranularly [67]. Failure modes are dependent on the localized microstructural changes in the strain concentration regions of the interconnections and the crack paths follow the networks of grain boundaries produced by recrystallization [68]. These results are considered that high temperature causes fast diffusion rate between interface of Cu and constituent element of solder, tin (Sn). Also, stress from residual stress [69] and caused by CTE mismatch associate with creep strain [70, 71] resulted to initial cracks along grain boundary of solder [69].

5.2.5 Diffusion Analysis by EDX

Fig. 5.8 shows EDX results at each cycle. NMPB has shorter initial diffusion length and slower diffusion speed. And solder bonding has longer initial diffusion length and faster diffusion speed. Fast diffusion speed results to voids near interface and thick intermetallic compounds (IMC) layer. Furthermore, IMC layer contribute to higher stress and creep strain [11, 72]. On the contrary, NMPB totally doesn’t have these problems that soldering bonding has and it is an excellent bonding method for application of solar cell that need to be put into cruel temperature cycles.

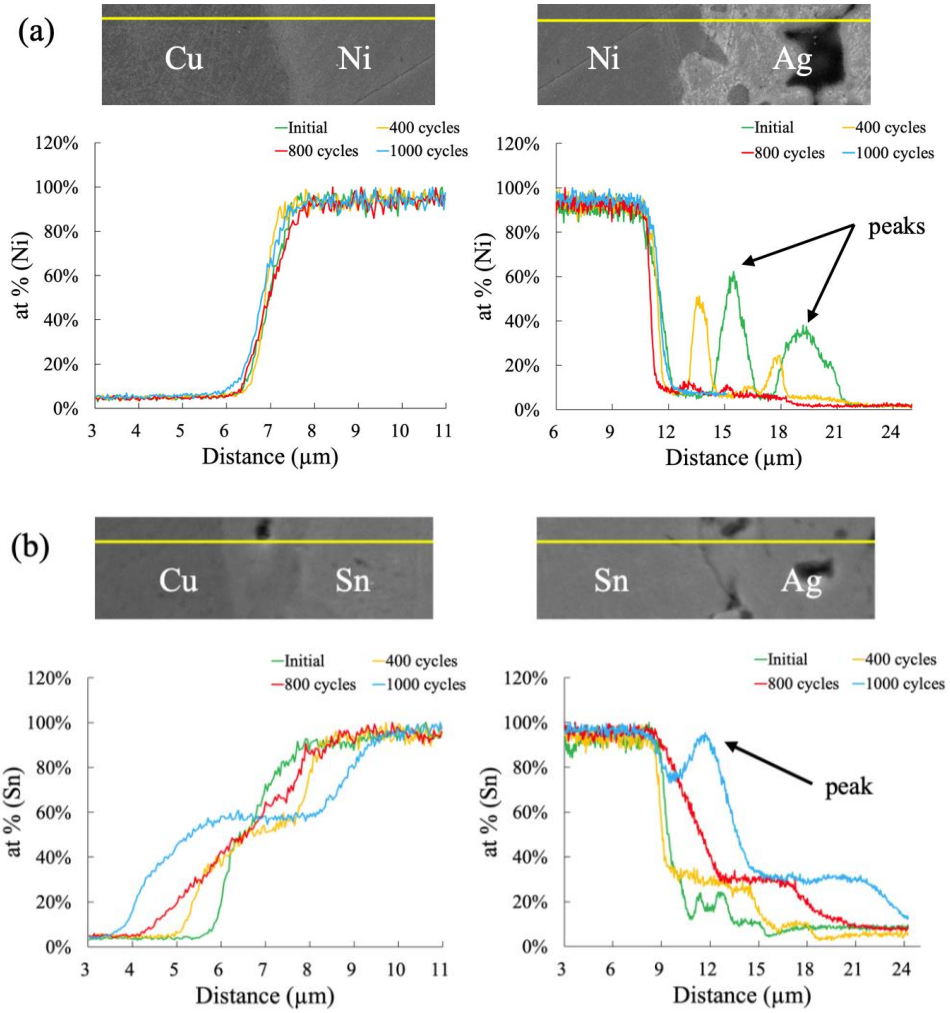

Fig. 5.8 EDX line analysis result of (a) NMPB (Ni) and (b) solder bonding (Sn) at each cycle.

The peaks in Sn-Ag resulted from holes and defects in Ag layer, which formed by sintering. In order to observe cross-section, samples were prepared by polishing process and metal particles were remained in these holes. Only atomic percent of Ni and Sn phases were taken because opposite phase information is negatively related to them. Fig. 5.8 was

made for comparison of different TC cycles.

Referring to Fig. 4.7, Cu_6Sn_5 and Ag_3Sn IMC layers were formed in Sn/Cu and Sn/Ag interfaces, respectively. Diffusion lengths are consistent with the results calculated by formula (4-2). In the meantime, diffusion length was also influenced by time according to Fick's second law and calculated as follows:

$$L(t) \propto \alpha\sqrt{(D\mathrm{t})} \tag{5-1}$$

Here, α is a constant, D is diffusion coefficient. Gradient became flatter in the middle of diffusion layer with the increase of TC cycles in Sn/Cu and Sn/Ag interfaces. Table 5.1 shows approximate diffusion lengths intercepted from Fig. 5.8 by taking half distance of slopes.

Table 5.1 Approximate Diffusion length of Sn read from Fig. 5.8.

Samples		**Diffusion lengths (μm)**
Sn (Cu-Sn)	400 cycles	2.13
	800 cycles	2.98
Sn (Sn-Ag)	400 cycles	6.12
	800 cycles	8.56

Because time of one TC cycle is constant, time of 800 cycles is twice of 400 cycles. As a result, in Cu/Sn and Sn/Ag interfaces, *L(t)* of Sn in 800 cycles would be 1.41 (√2) times of 400 cycles. From Table 5.1, approximate diffusion lengths of Sn in Cu/Sn and Sn/Ag are 2.13 and 2.98 μm in 400 cycles, 6.12 and 8.56 μm in 800 cycles, respectively. These results shows that the latter is 1.41 (√2) times that of the former. This is consistent with formula (5-1).

Here, diffusion lengths of Ni were not inspected because they were too short to intercept. Furthermore, due to barrier layer formed by Ni, Cu and Ag could not diffuse into Ni layer, no IMC layer was formed in Cu/Ni and Ag/Ni interface. This could also be considered that NMPB is a tough bonding against stress and strain during thermal cycles.

5.2.6 EBSD Analysis of Cross Section

Fig. 5.9 shows cross section EBSD result of (a) initial and (b) 1000 cycles NMPB samples. The results show that NMPB has micro size columnar crystal growth and until 1000 cycles, NMPB didn't have any recrystallization. This is the reason why NMPB has stronger against TC cycles. Also, columnar crystal perpendicular to substrate is the key

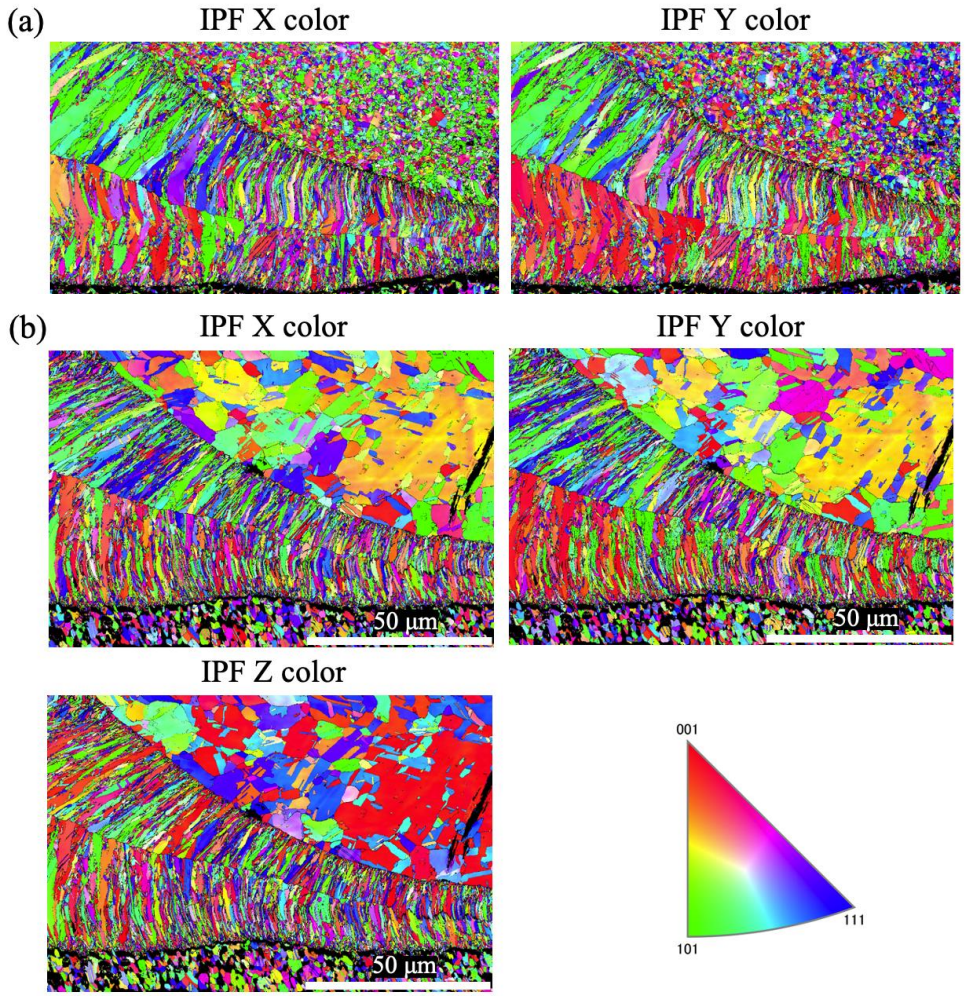

Fig. 5.9 Cross section EBSD results of (a) initial and (b) 1000 cycles.

point that NMPB could grow without any voids along meeting interface comparing to commercial electroplating method.

5.2.7 Vickers Hardness

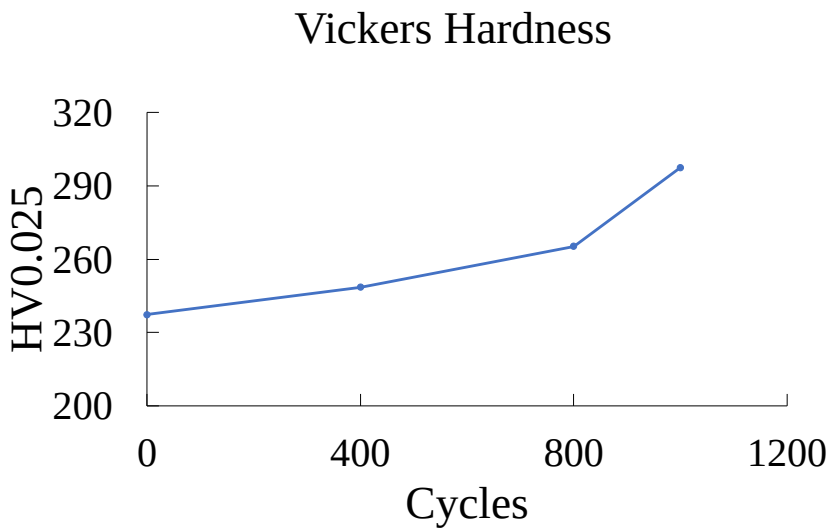

Fig. 5.10 Vickers hardness of Ni layer in cross section.

Vickers hardness of Ni layer in Cross section is shown in Fig. 5.10. Hardness slightly increased from 237.4 to 297.5 as TC cycle increasing. This indicates that during TC test, dislocation accumulated in Ni layer made Ni became harder than initial condition. However, even hardness increasing after 1000 cycles TC test didn't influence reliability of NMPB that no cracks appeared in Ni layer or near boundary.

5.3 Damp Heat (DH) Test

5.3.1 IEC 61215 Standard of DH Test

In IEC 61215 standard 2005, DH test was defined as follow.

10.13 Damp-heat test

10.13.1 Purpose

To determine the ability of the module to withstand the effects of long-term penetration of humidity.

10.13.2 Procedure

The following severities are applied:

Test temperature: 85 °C ± 2 °C, relative humidity: 85% ± 5%, test duration: 1 000 h.

A 1000-hour DH test is considered equivalent to approximately 10 years of outdoor testing.

5.3.2 Experimental Procedure

The second test is damp heat (DH) test, conditions of which is 85°C and 85% Relative Humidity (RH) for 1000 hours in the environment chamber (PR-1KT, ESPEC Corp., Japan), based on section 10.13 in IEC 61215. Also, the electrical performance of each sample was measured each 250 hours by the same solar simulator. Typical I-V curves

were obtained as shown in Fig. 5.11 (a) NMPB and (b) solder bonding. Still, the results show that after 1000 hours test, degradation was confirmed in solder bonding cells and NMPB cells decreased a little but kept excellent quality after 1000 cycles finished.

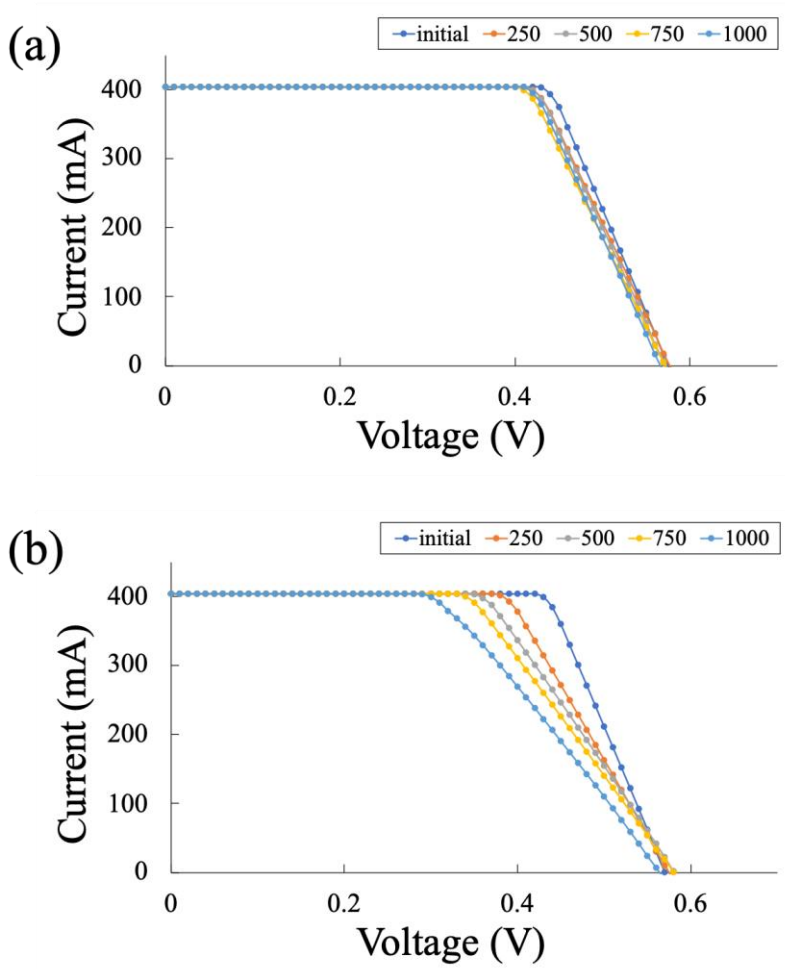

Fig. 5.11 Typical I-V curve of (a) NMPB, (b) solder bonding during 1000 hours DH test.

5.3.3 I-V Curves and Degradation

Fig. 5.12 (a) shows more details of average power max (P_{max}) of 5 cells every 250 hours comparing to initial condition. The results of (b) show that P_{max} of solder bonding cells decreased 23.0% when 1000 hours test finished. However, only 3.8% decreased in NMPB cells after 1000 hours.

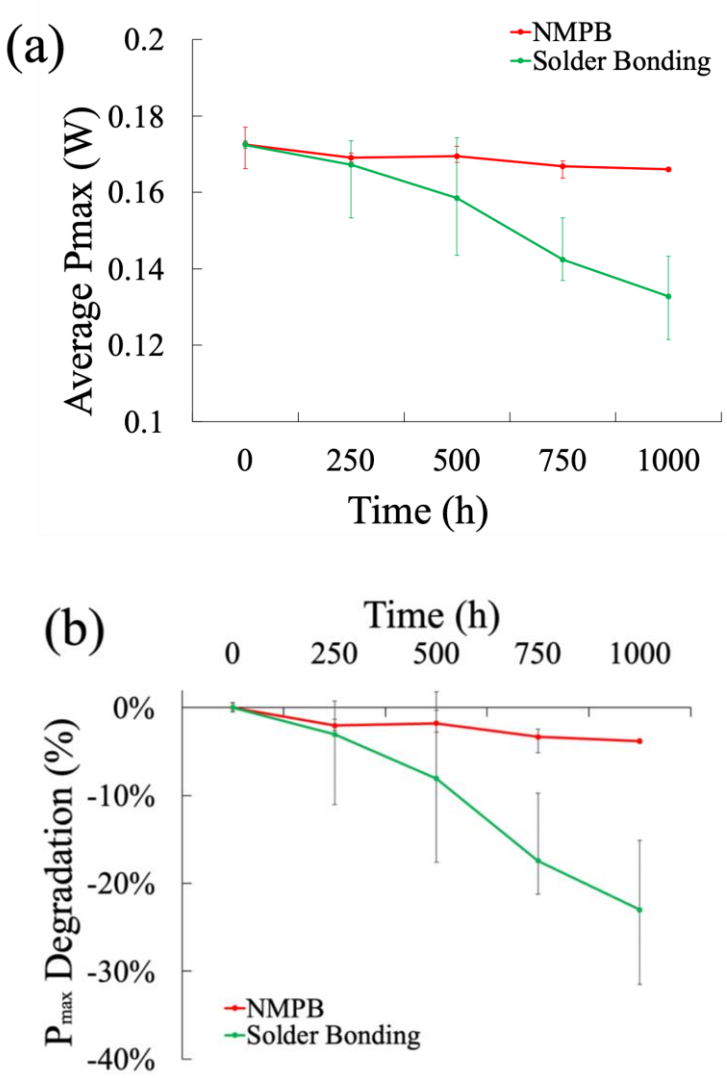

Fig. 5.12 (a) Average P_{max} and (b) P_{max} degradation of each 250 hours.

5.3.4 Cross Section Observation by SEM

Fig 5.13 (a) shows the surface change of NMPB and solder bonding every 500 hours. This is considered that serious corrosion occurred in solder bonding and NiO passivation film has a tough protection from corrosion. Fig. 5.13 (b) shows EDX point analysis of each sample. The result shows tin was severely oxidized until the depth of 10 μm while Ni had no oxidation inside material. As a result, it could be predicted that NMPB could prevent corrosion in long term operation from air and water.

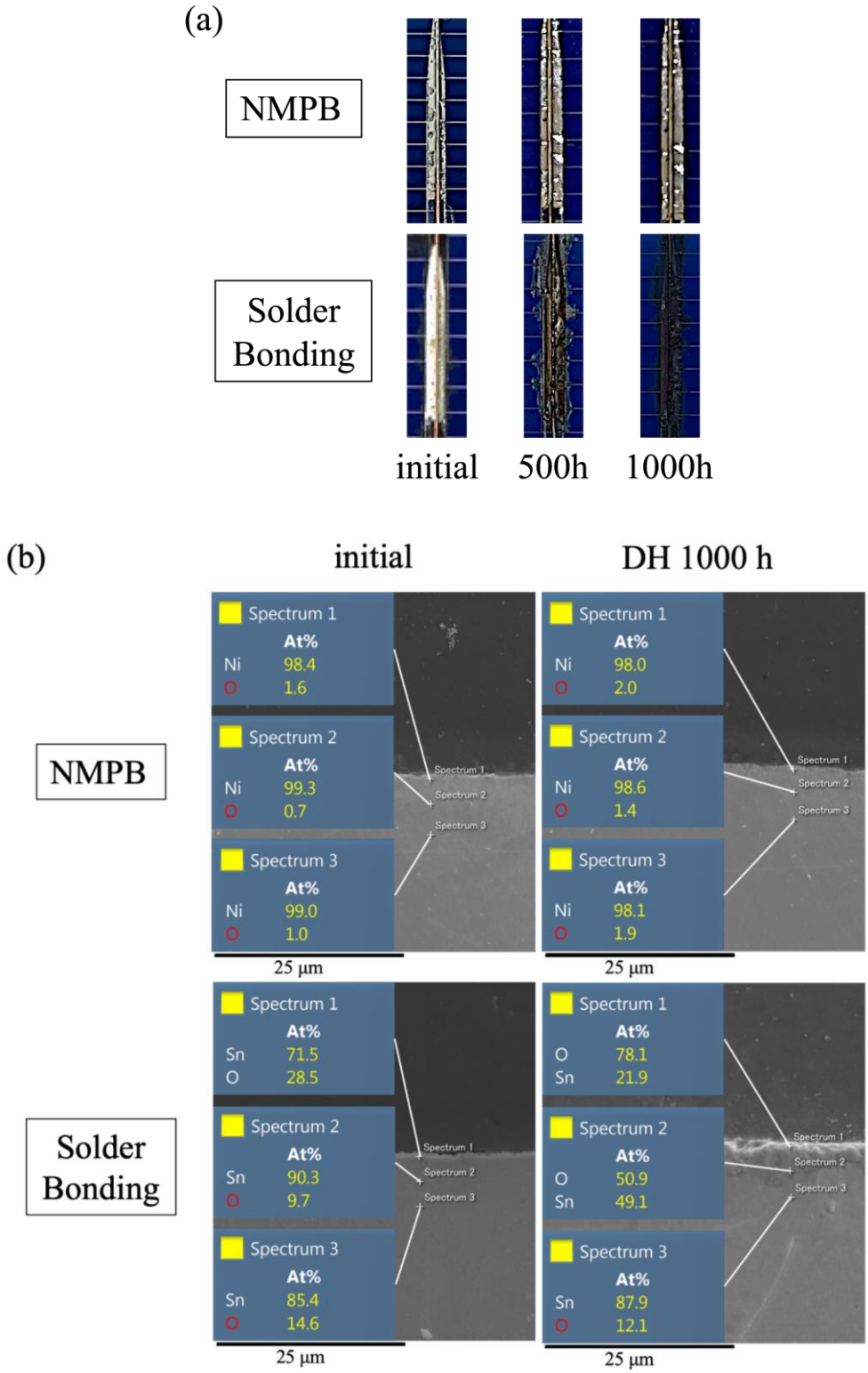

Fig. 5.13 (a) Surface change of each sample. (b) EDX point analysis of each sample.

5.4 Conclusion

For 1000 cycles TC test, NMPB crystalline silicon solar cell samples have a little degradation of 1.9% on max output power, which is much smaller than solder bonding (64.7%). Also, for 1000 hours DH test, NMPB samples also have a degradation of 3.8%, which is smaller than solder bonding (23.0%). These results of two tests have apparent proofs that NMPB is suitable for improvement in interconnection of solar cell so that PV modules could operate longer in high reliability. Furthermore, it is available to apply NMPB to PV module by laboratory fabrication.

Chapter 6: Application and Reliability on Crystalline Silicon PV Modules Interconnected by NMPB Technology

6.1 NMPB Interconnection Process

Fig. 6.1 shows the front and back picture of a mono silicon cell interconnected by NMPB with Cu wires. The size of solar cell is 166*83 mm and on front side, there are 36 (4*9)

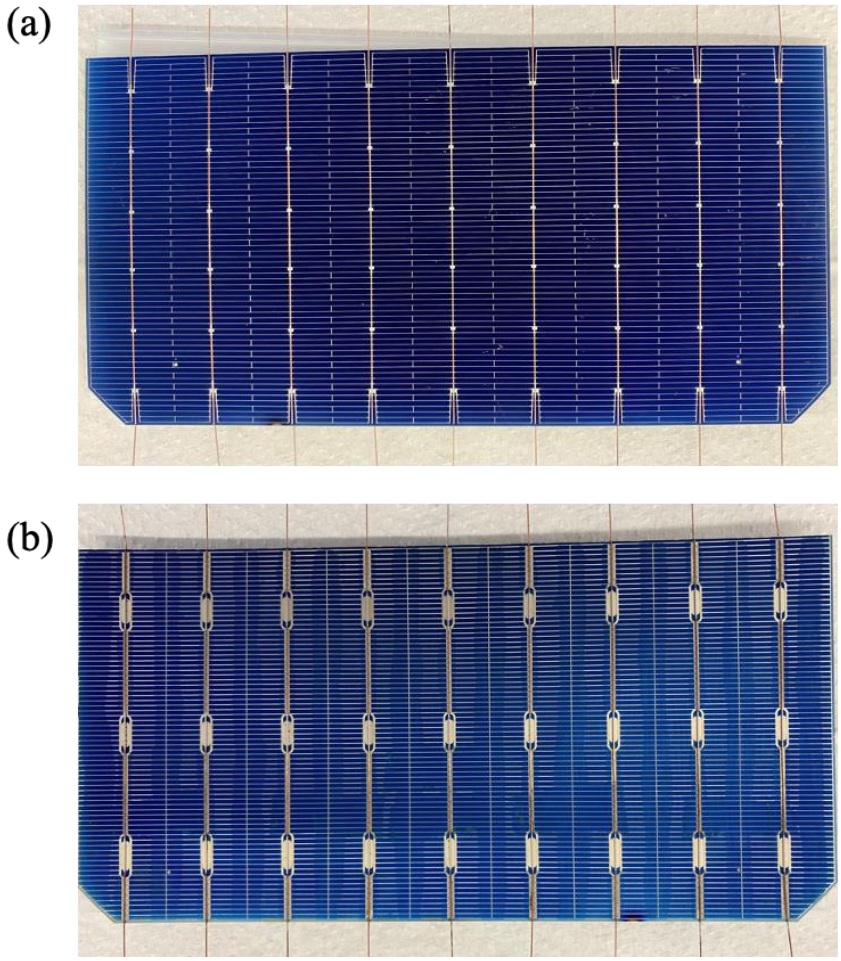

Fig. 6.1 Front (a) and back (b) picture of mono silicon solar cell interconnected by NMPB with Cu wires.

smaller square Ag busbars whose size are 1.5 mm^2, and 18 (2*9) bigger square Ag busbars whose size are 2 mm^2, surrounded by Ag fingers. On back side, there are also 27 (3*9) square Ag busbars surrounded by Al fingers. The diameter of Cu wire is 300 mm. Because Ag finger is electro-connected to Ag busbar, Ag finger would also be electroplated with Ni film. Furthermore, Ag finger with Ni film is concerned to be a protection film against corrosion. The condition of NMPB is the same with Table 2.2 and the plating times are 90 min in front and 150 min in back, respectively. Fig. 6.2 shows cross section of one interconnection joint of solar cell, front and back. The results shows that Cu wires are perfectly bonded by Ni without any voids and cracks.

A control group of solar cells with solder bonding were also fabricated with Cu wire coated with eutectic solder (Sn60/Pb40) in order to make comparison.

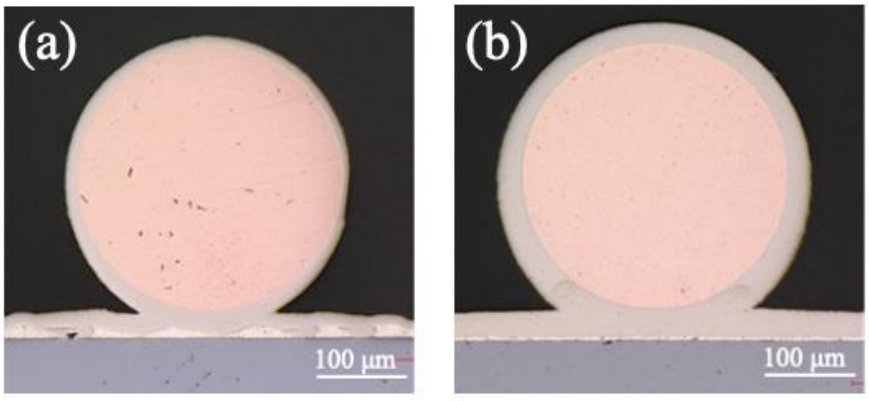

Fig. 6.2 Cross section of surface (a) and back (b) interconnection of a mono silicon solar cell.

6.2 Pull Test and Shear Test of Interconnections

In order to realize the bonding strength and variability of interconnections, pull and shear test were performed. Fig. 6.3 (a) shows a pull tester and (b) shows the schematic diagram of shear test.

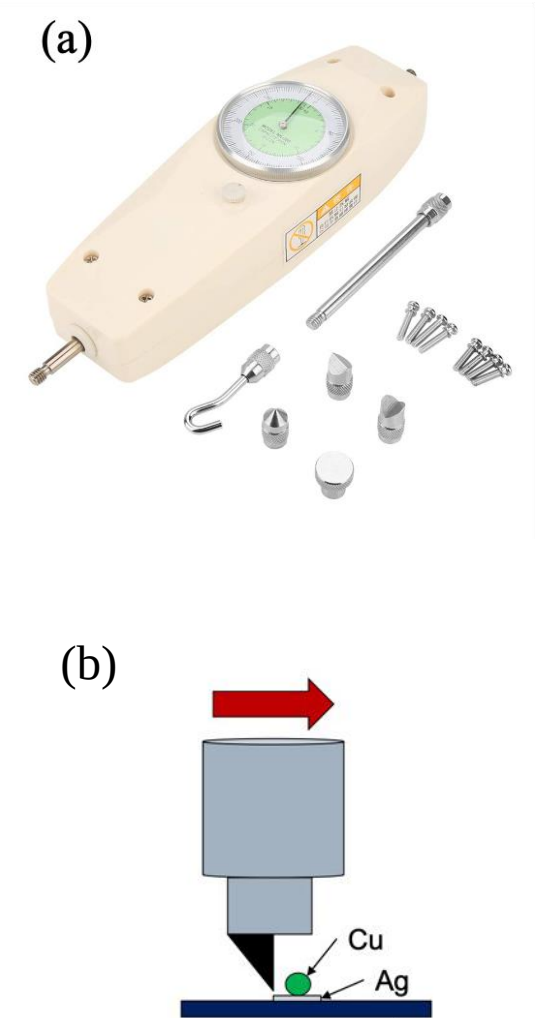

Fig. 6.3 (a) Pull tester (b) Schematic diagram of shear test.

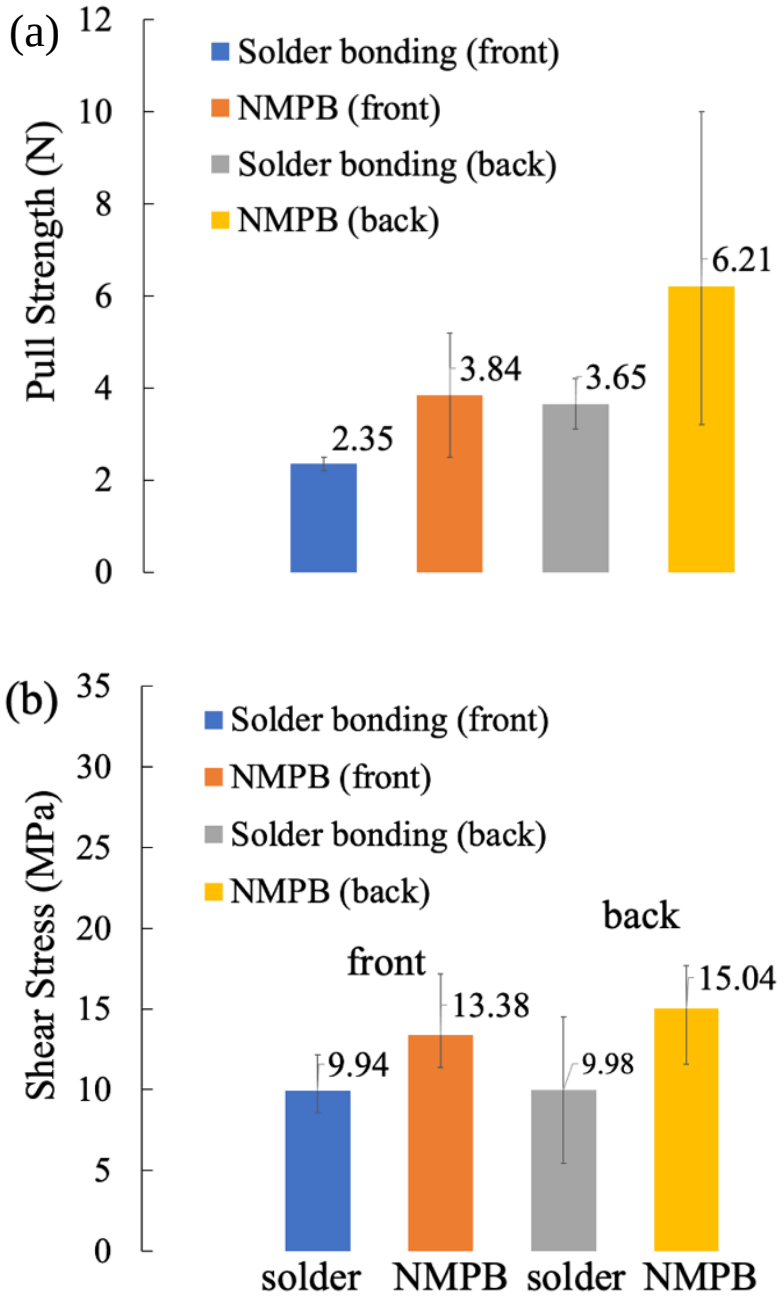

Fig. 6.4 Results of (a) pull test and (b) shear test.

Pull test was performed by a hook following the direction of Cu wire and parallel to the surface of solar cell. Fig 6.4 shows the results of pull and shear tests. Compared with

commercial solder bonding joints, the average pull strength of NMPB was found to be 3.84 N in the front and 6.21 N in the back, which is higher than that of the solder. In addition, as shown in Fig 6.4 (b), the results of the shear test shows that the average shear stress of the front and back side were 13.38 and 15.04 MPa, respectively, and it was found that the bonding strength was stronger than that of solder.

Furthermore, as a result of observing the fracture points in the shear test, as shown in Fig. 6.5, the front side of the solder joints fractured at the interface between solder and Ag or Ag and Si, and the back side fractured at the interface between Ag and Si. On the other hand, all the joints on the front side of NMPB broke at the interface between Ag and Si. And on the back side, in addition to fracture at the interface between Ag and Si, there was also cell cracking. These results show that NMPB has sufficient bonding strength for solar cells.

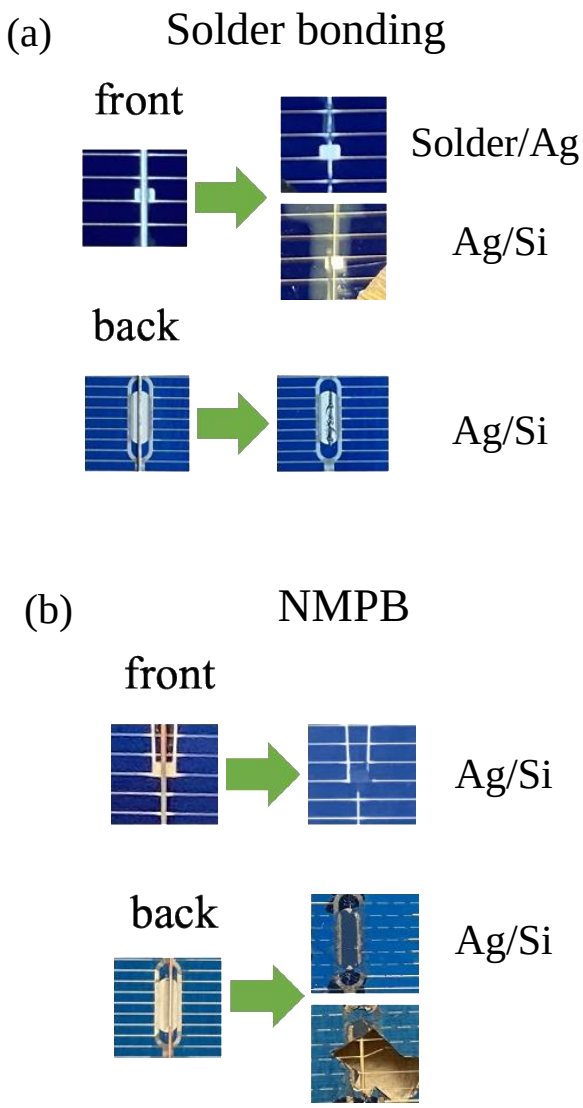

Fig. 6.5 Observation of fracture point of (a) solder bonding (b) NMPB samples.

6.3 Fabrication of PV Module

6.3.1 Process of PV Module Fabrication

After Ni electroplating process, the solar cells were taken to washing process in order to remove resist and impurities remained on surface. Two times acetone and one time ethanol washing were taken in order and one washing process lasted 5 min. Finally, the solar cells dried on the hot plate at 45 ℃.

After the washing process, the solar cells were taken to fabrication process. Fig. 6.6 shows schematic cross-sectional view of NMPB PV module. Encapsulants like ethylen-vinyl acetatesheet (EVA), tempered glass and polyethyleneterephthalate (PET) back sheet. The solar cells were firstly covered by EVA sheet, then tempered glass and PET sheet on the front and back side, respectively. Finally, the combination was taken to pressure process which performed under 150 ℃in vacuum atmosphere.

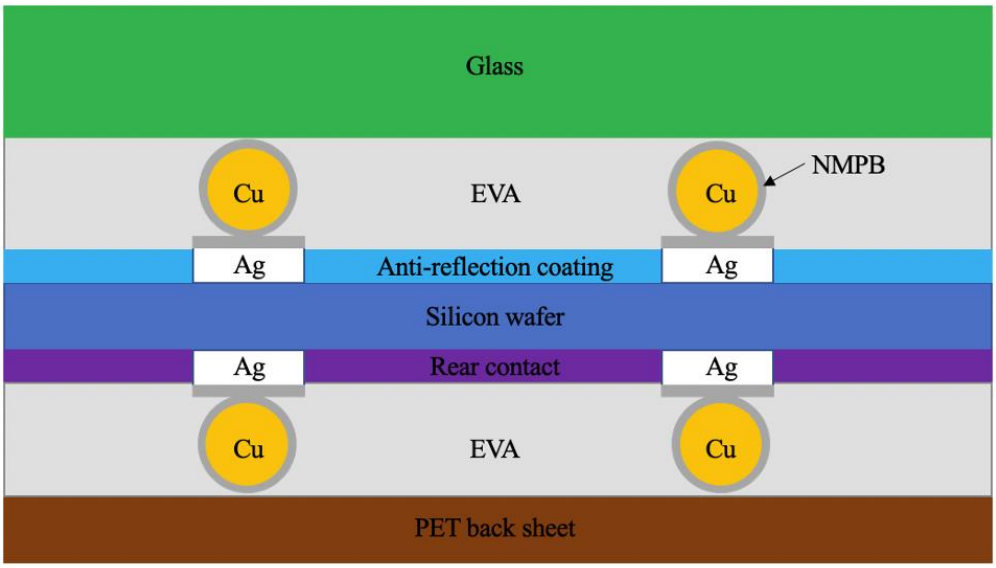

Fig. 6.6 Schematic cross-sectional view of NMPB PV module.

6.3.2 Electroluminescence (EL) Test

Electroluminescence (EL) method is one of the methods for evaluating the power generation performance of solar cells. Its structure is similar to that of an LED (Light Emitting Diode). By injecting current into the solar cell in the positive direction, it can be made to emit light like an LED. Since it is used in multiple layers, light emission with a wavelength of around 1100 nm can be obtained. If this is captured by an image sensor (camera), the power generation performance of the device can be easily evaluated as a light and dark image [73]. EL test is usually performed in a dark room for acquire good quality of image.

Fig. 6.7 (a) shows front picture of one NMPB PV module (b) EL picture of the same PV module. The same module of solder bonding was also manufactured as shown in Fig. 6.8. From EL images, connection of every single joint was perfectly interconnected in NMPB module compared with solder bonding.

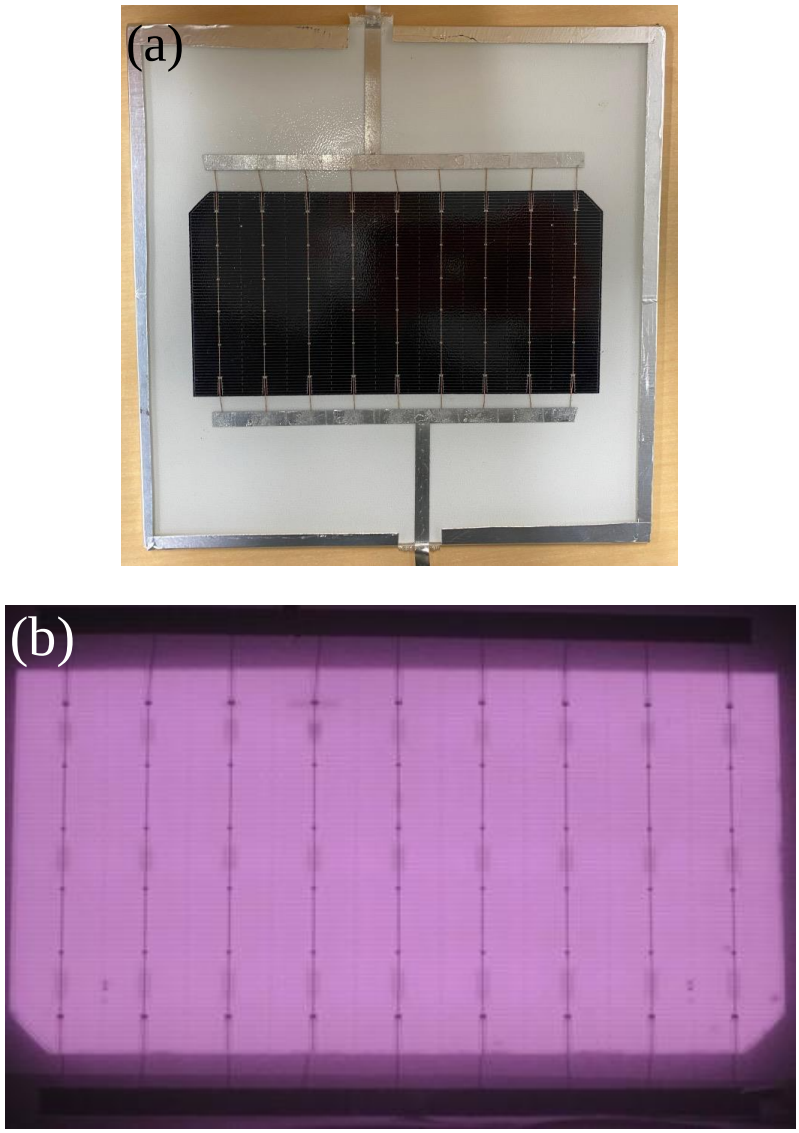

Fig. 6.7 (a) Front picture of one NMPB PV module.
(b) EL image of the same PV module.

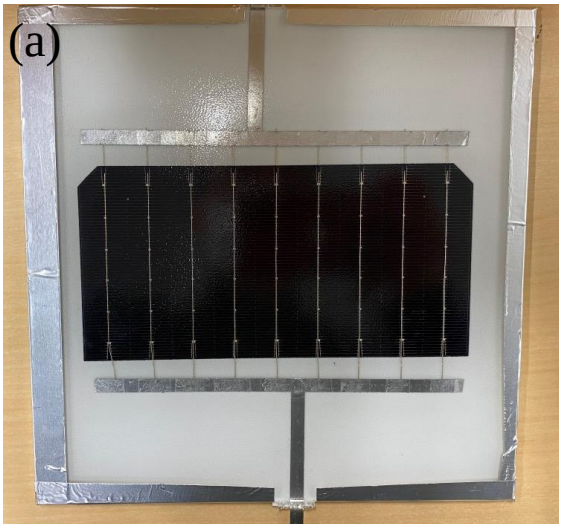

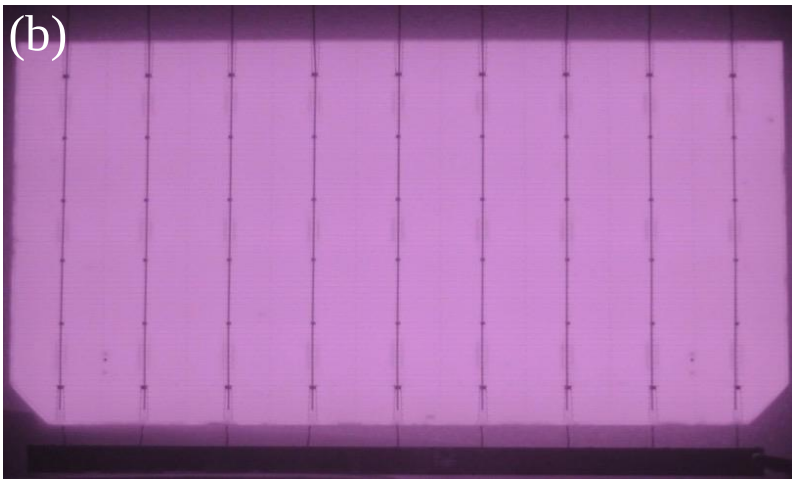

Fig. 6.8 (a) Front picture of one solder bonding PV module.
(b) EL image of the same PV module.

Modules show no dark area in EL image initially and this means no output power loss from electrodes due to interconnection process.

6.4 TC Test

The TC cycles were set from -40 ℃ to 130 ℃ for accelerating the testing speed. The slope is of temperature to time is the same to Fig. 5.2 following IEC standard. Every 200 cycles, EL images, I-V curves and output characteristics were measured, until 800 cycles.

6.4.1 EL Images

Fig. 6.9 shows EL images of solder bonding and NMPB modules every 200 cycles at TC test.

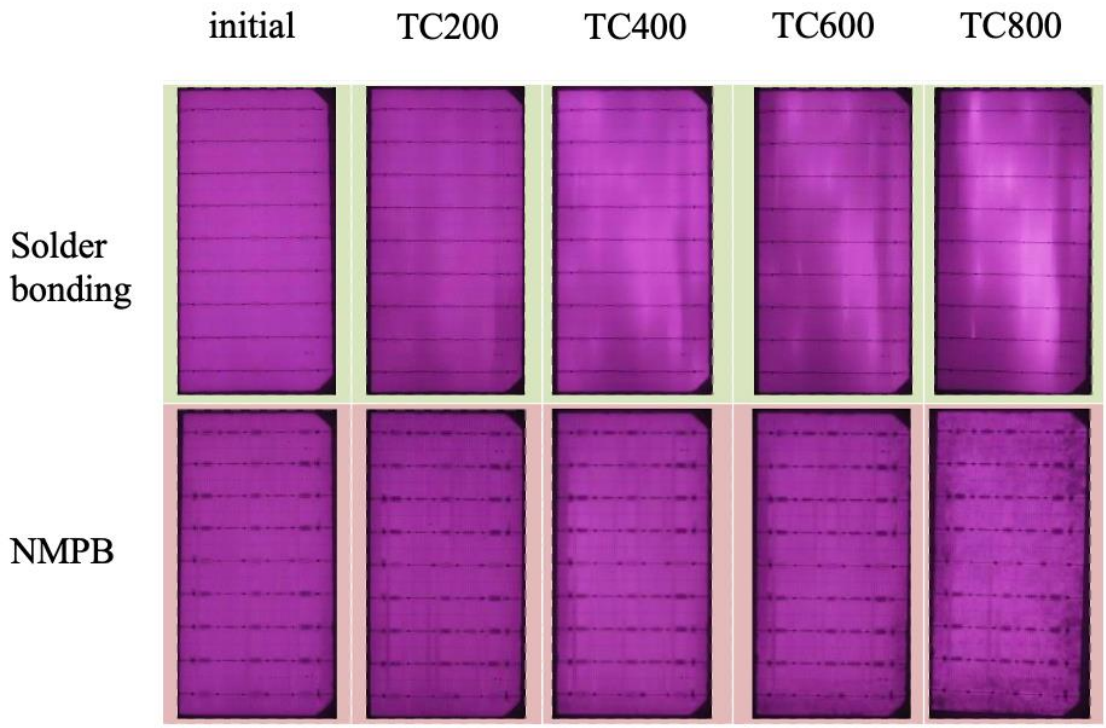

Fig. 6.9 EL images of solder bonding and NMPB modules every 200 cycles at TC test.

From the EL image results, it seems that the size of the shadow increases as the number of cycles increases in solder bonding module. The shadow is also expanded for NMPB module, but the degree is much smaller than that for solder bonding. NMPB is expected to result in less peeling of the interconnection.

6.4.2 Table of Module Characteristics

Initial characters of one module are that I_{sc} is 5.5 A, V_{oc} is 0.68 V, Fill Factor (FF) is 0.78, Pmax is 3.04 W and E_{ff} is 22.1% (approximate). The retention rate is the degradation of each character.

From the table, 19.5% degradation of efficiency in solder bonding and 6.7% in NMPB were confirmed.

Table 6.1 Retention rate of modules.

retention rate

Initial	Isc/A	Voc/V	FF	Pmax/W	Eff/%
Solder	100%	100%	100%	100%	100%
NMPB	100%	100%	100%	100%	100%

TC200	Isc/A	Voc/V	FF	Pmax/W	Eff/%
Solder	99.7%	99.8%	97.8%	97.3%	97.3%
NMPB	99.8%	99.6%	99.1%	98.5%	98.5%

TC400	Isc/A	Voc/V	FF	Pmax/W	Eff/%
Solder	99.6%	99.9%	95.1%	94.6%	94.6%
NMPB	99.7%	99.7%	98.7%	98.1%	98.1%

TC600	Isc/A	Voc/V	FF	Pmax/W	Eff/%
Solder	99.1%	99.7%	91.3%	90.2%	90.2%
NMPB	99.7%	99.6%	97.5%	96.8%	96.8%

TC800	Isc/A	Voc/V	FF	Pmax/W	Eff/%
Solder	99.4%	100.0%	81.0%	80.5%	80.5%
NMPB	99.8%	99.6%	93.8%	93.3%	93.3%

6.4.3 Graph of Isc, Voc, FF and Pmax

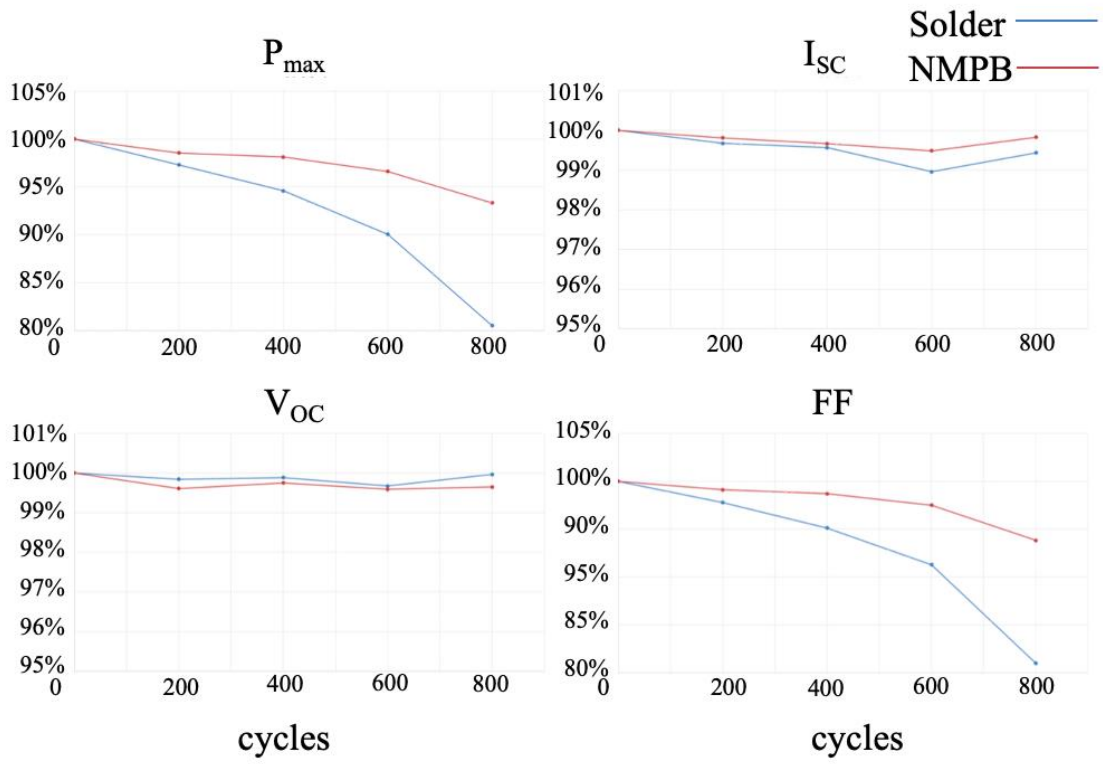

Fig. 6.10 Retention rate of Isc, Voc, FF and P_{max}.

Retention rates show that NMPB module has lower degradation in Isc, Voc, FF and P_{max} than solder bonding module. The decrease of output power is considered to be related to increase of series resistance.

6.4.4 I-V Curves

I-V curves also show that NMPB module had lower degradation in output power (Fig. 6.11). Compared with solder bonding curve, the curve maintained high similarity with initial even 600 thermal cycles finished. This result is consistent with the P_{max} result in table 6.1.

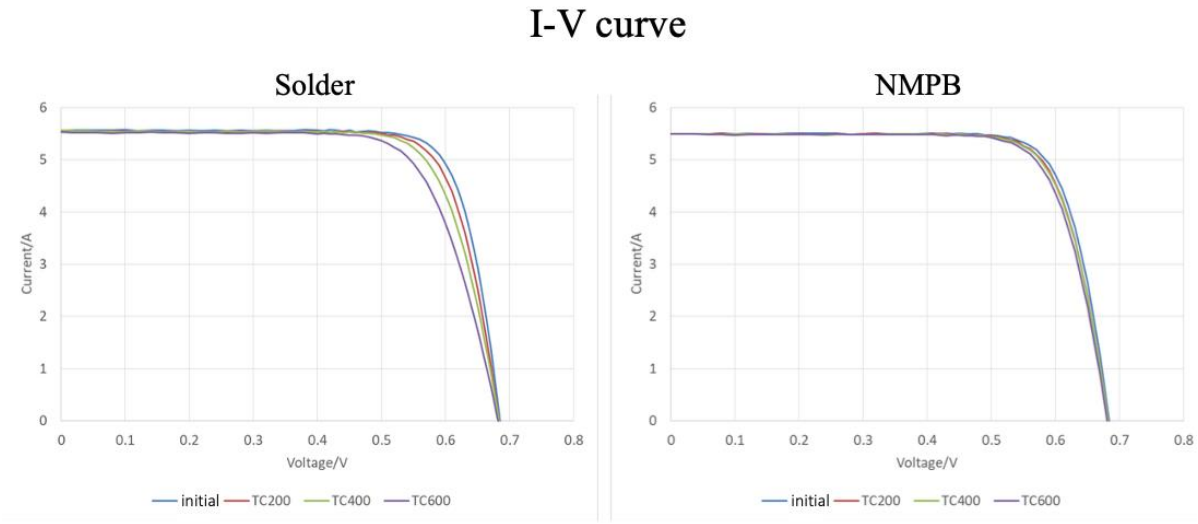

Fig. 6.11 I-V curve of modules every TC 200 cycles.

6.5 Conclusion

For both solder bonding and NMPB modules, the main reason for the decrease in P_{max} retention is the decrease in Fill Factor (FF), and the decrease in FF is due to deterioration of the cell electrodes. This is presumed to be caused by an increase in series resistance due to peeling of the interconnection.

From the EL results, it seems that the size of the shadow increases as the number of TC cycles increases in solder bonding. The shadow is also increased for NMPB, but the degree is smaller than that for solder bonding. NMPB is expected to result in less peeling of the interconnection.

As a conclusion, in TC test, NMPB has better reliability in interconnection of PV modules.

Chapter 7: Conclusion

In this study, Ni micro-plating bonding (NMPB), a new method of forming interconnection of crystalline silicon solar cell PV module was proposed. Due to poor resistance to thermal cycling stress and corrosion of traditional solder bonding method, a replaceable method is considered to be necessary. The NMPB interconnection provides key advantages: low temperature (55 ℃) process, enhancement of reliability from strain and stress caused by high temperature and coefficient of thermal expansion (CTE) mismatch between metals and silicon. Furthermore, material of NMPB, Ni, possesses excellent corrosion resistance. All these advantages made us to believe that it has high possibility than NMPB could take over solder bonding to be next generation of crystalline silicon solar cell interconnection.

Long-term reliability of NMPB and application to solar cells and further PV modules were demonstrated in three steps.

In research history of NMPB， although various researches have been conducted on bonding reliability of NMPB, considering CTE mismatch, long-term reliability evaluated from the aspect of metal fatigue due to thermal stress has not been much discussed. For this purpose, firstly, in Chapter 4, long-term reliability of NMPB was confirmed by resonant type fatigue test. The results shows that NMPB has 2.2 times higher fatigue limit

than solder bonding. This is a forceful result that NMPB could replace solder as a high reliability bonding method.

With the excellent results of NMPB on long-term reliability, crystalline silicon solar cell interconnected by NMPB with copper wire was proposed. Secondly, in Chapter 5, single solar cells interconnected both by solder bonding and NMPB was compared in TC and DH test. High reliability was confirmed with about 1.9% degradation of output power for up to 1000 thermal cycling (TC) test and 3.8% for 1000 hours of damp heat (DH) test in bare NMPB solar cells, while 64.7% degradation in thermal cycling test and 23.0% in damp heat test were confirmed in solder bonding solder cells. The results show that NMPB solar cells has higher output power and more stable structure against thermal cycles. In addition, Ni is also an excellent material that strong with corrosion so that solar cells maintained higher output power.

Finally, in Chapter 6, in order to realize life span of PV module interconnected by NMPB, NMPB and solder bonding PV modules were made with EVA and further encapsulants. TC test was performed. The result show that retention of the maximum output power (Pmax) of NMPB PV modules is much higher than solder bonding modules after TC cycles. As a conclusion, it is concerned that long-term reliability of crystalline silicon

solar cell PV module could extend its life span from commercially 25 years to 40 years, by using NMPB interconnection technology.

Even in experimental fabrication, it takes around 90 min to interconnect one PV module, it is expected that the electroplating time could be shorter than 30 min when automatic manufacture line is used. Furthermore, compared with reflow process of solder bonding, the electricity consumption in factory electroplating could totally rely on solar system on the roof of factory buildings. These would make NMPB a charmful and hopeful method for manufacture of PV modules.

Reference

[1] Saga T., "Advances in Crystalline Silicon Solar Cell Technology for Industrial Mass Production", NPG Asia Mater., 2, pp. 96-102 (2010).

[2] Snapshot of Global PV Markets 2021, IEA-PVPS (2021).

[3] www.cleanenergyreviews.info/blog/most-efficient-solar-panels, Most Efficient Solar Panels 2021, Clean Energy Reviews.

[4] Musa T. Zarmai et al., "A Review of Interconnection Technologies for Improved Crystalline Silicon Solar Cell Photovoltaic Module Assembly", Applied Energy, Vol. 154, 15, pp. 173-182 (2015).

[5] J. H. Wohlgemuth et al., "Long Term Reliability of PV Module", 20th European Photovoltaic Solar Energy Conference and Exhibition, pp. 6–10 (2005).

[6] Campeau Z, Anderson M, Hasselbrink E, Kavulak D, Shen Y-C, Lacerda R, et al., "SunPower module degradation rate", SunPower Corp., pp. 1–61 (2013).

[7] Noriyuki Kato et al., "High-Temperature-Resistant Interconnections Formed by Using Nickel Micro-Plating and Ni Nano-particles for Power Devices", Transactions of The Japan Institute of Electronics Packaging, Vol. 6, pp. 87-92 (2013).

[8] W. Wondrak, R. Held, E. Niemann and U. Schmid, "SiC devices for advanced power and high-temperature applications", IEEE Trans. Ind. Electron., vol. 48, no. 2, pp. 307-

308 (2001).

[9] Chen, C. H., Lin, F. M., Hu, H. T., & Yeh, F. Y., International Symposium on Solar Cell Technologies, 4 (2008).

[10] Shin, H., Han, E., Park, N., Kim, D., Energies 11, 3256 (2018).

[11] Jicheng Gong, Changqing Liu, Paul P. Conway, Vadim V. Silberschmidt, Scripta Materialia 60, 333 (2009).

[12] M. T. Zarmai, n. N. Ekere, C. F. Oduoza & E. H. Amalu, "Effect of Intermetallic Compounds on Thermo-Mechanical Reliability of Lead-free Solder Joints in Solar Cell Assembly", International Journal of Mechanical Engineering (IJME), Vol. 4, Issue 6, 29-38 (2015).

[13] K. Tatsumi et al., "Development of Packaging Technology for High Temperature Resistant SiC Module of Automobile Application", IEEE 67th Electronic Components and Technology Conference (ECTC), pp. 1316-1321 (2017).

[14] K. Tatsumi et al., "High Temperature Resistant Packaging Technology for SiC Power Module by Using Ni Micro-Plating Bonding", IEEE 69th Electronic Components and Technology Conference (ECTC), pp. 1451-1456 (2019).

[15] Musa Tanko Zarmai, "Modelling of Solder Interconnection’s Performance in Photovoltaic Modules for Reliability Prediction", School of Engineering, Faculty of

Science and Engineering University of Wolverhampton, Doctor’s thesis (2016).

[16] Wang, T.-C. and Tsai, S.-Y., "Solar Panel Supplier Selection for the Photovoltaic System Design by Using Fuzzy MCDM Approaches", Energies, Vol.11, Issue 8 (2018).

[17] Saga, T., "Advances in crystalline silicon solar cell technology for industrial mass production", NPG Asia Materials, 2(3), pp.96-102 (2010).

[18] Sunshot Initiative, Amorphous Silicon (2013a). Energy Efficiency & Renewable Energy, 1-2 (2013).

[19] Shah, A.V., Schade, H., Vanecek, M., Meier, J., Vallat-Sauvain, E., Wyrsch, N., Kroll, U., Droz, C. and Bailat, J., "Thin-film silicon solar cell technology", Progress in Photovoltaics: Research and Applications, 12(2-3), pp.113-142 (2004).

Available at: <http://energy.gov/eere/sunshot/photovoltaics-research-and- development>.

[20] Sunshot Initiative, Cadmium Telluride (2013b). Energy Efficiency & Renewable Energy, 1-2 (2013).

Available at: <http://energy.gov/eere/sunshot/photovoltaics-research-and- development>.

[21] Sunshot Initiative, Copper Indium Gallium Diselenide (2013c). Energy Efficiency & Renewable Energy, 1-2 (2013).

Available at: <http://energy.gov/eere/sunshot/photovoltaics- research-and-development>.

[22] Abass Aimi, "Light absorption enhancement and electronic properties of thin-film

solar cells" (2014).

[23] Han, C., Park, N. and Jeong, J., " Lifetime Prediction of Silicon PV Module Ribbon Wire in Three Local Weathers", Photovoltaic Module Reliability Workshop (2012). Available at: <http://www1.eere.energy.gov/solar/pdfs/pvmrw12_poster_si_han.p df>.

[24] Jeong, J., Nochang, P., Wonsik, H. and Changwoon, H., "Analysis for the Degradation Mechanism of Photovoltaic Ribbon Wire under Thermal Cycling", Proceedings of 37th Photovoltaic Specialists Conference, pp.003159-003161 (2011).

[25] Sakamoto, S., T. Kobayashi, and S. Nonomura, "Epidemiological Analysis of Degradation in Silicon Photovoltaic Modules", Japanese Journal of Applied Physics, 51, pp.1-4 (2012).

[26] Jeong, J.S., Park, N. and Han, C., "Field Failure Mechanism Study of Solder Interconnection for Crystalline Silicon Photovoltaic Module", Microelectronics Reliability, 52, pp. 2326-2330 (2012).

[27] Skoczek, A., Sample, T. and Dunlop, E.D., "The results of performance measurements of field-aged crystalline silicon photovoltaic modules", Progress in Photovoltaics: Research and Applications, 17 (4), pp.227- 40 (2009).

[28] Granata JE, Boyson WE, Kratochvil JA, Quitana MA., "Long-Term Performance and Reliability Assessment of 8 PV Arrays at Sandia National Laboratories", Proceedings

of 34th IEEE Photovoltaic Specialist Conference, pp.1486–1491 (2009).

[29] Betts, A.K., "The diurnal cycle over land" (2004).

Available at:<http://alanbetts.com/workspace/uploads/ec-sem01_betts-1274648223.pdf>.

[30] Nochang Park, Changwoon Han, Donghwan Kim, "Effect of moisture condensation on long-term reliability of crystalline silicon photovoltaic modules", Microelectronics Reliability, Vol. 53, Iss. 12, pp. 1922-1926 (2013).

[31] Wonwook Oh, Seongtak Kim, Soohyun Bae, Nochang Park, Sung-Il Chan, Yoonmook Kang, Hae-Seok Lee, Donghwan Kim, "Migration of Sn and Pb from Solder Ribbon onto Ag Fingers in Field-Aged Silicon Photovoltaic Modules", International Journal of Photoenergy, Vol. 2015, Article ID 257343, 7 pages (2015).

[32] T.H. Kim, N.C. Park, D.H. Kim, "The effect of moisture on the degradation mechanism of multi-crystalline silicon photovoltaic module", Microelectronics Reliability, Vol. 53, Iss. 9–11 (2013).

[33] Wonwook Oh, Seongtak Kim, Soohyun Bae, Nochang Park, Yoonmook Kang, Hae-Seok Lee, Donghwan Kim, "The degradation of multi-crystalline silicon solar cells after damp heat tests", Microelectronics Reliability, Vol. 54, Iss. 9–10, pp. 2176-2179 (2014).

[34] Huaping Xiong, Chuanhai Gan, Xiaobing Yang, Zhigang Hu, Haiyan Niu, Jianfeng Li, Jianfang Si, Pengfei Xing, Xuetao Luo, "Corrosion behavior of crystalline silicon solar

cells, Microelectronics Reliability", Vol. 70, pp. 49-58 (2017).

[35] Contemporary Electroplating Textbook, Electroplating Study Group, Nikkan Kogyo Shimbun, pp. 2-3 (2011).

[36] Electroplating Textbook, Electroplating Study Group, Nikkan Kogyo Shimbun, pp. 24-27 (1986).

[37] Hayato Kiuchi, "Study on High Temperature Heat Resistant Mounting Technology for Power Devices by Ni Micro-Plating Using Sulfamic Acid Bath", Graduate School of Information, Production and Systems (IPS), Waseda University, Master's thesis (2016).

[38] Hiroto Nakagawa, "Establishment of High Temperature Heat-Resistant Mounting Technology for Power Modules by NMPB", IPS, Waseda University, Master's thesis (2016).

[39] User Manual of Resonant Thin Plate Fatigue Test Device RF-HT, pp. 17-18, Nippon Techno Plus Co. Ltd.

[40] Masayuki Tsushida et al., "Development of Fatigue Testing Machine and Investigation of Fatigue Fracture Behavior of Mg-Zn-Y Alloy", Kumamoto University (2007).

[41] Masayuki Tsushida, Ryosuke Ikeda, Hiromoto Kitahara and Shinji Ando, "Development of Fatigue Testing Machine for Thin Sheet Specimen and Fatigue Test for

Magnesium Single Crystal", Journal of the Society of Materials Science, Japan, Vol. 58, No. 8, pp. 703-708 (2009).

[42] Z. Iwai, M. Hino and I. Mizumoto, "Shindokogaku no Kogi to Ensyu", pp. 139-140, Nisshin syuppan (2000).

[43] Shinji Kumai and Masaharu Kato, "Low Cycle Fatigue in Metallic Materials", Journal of SHM, Basic Science Series. Part 28th, pp. 2-10 (1993).

[44] Physical Electronics, Handbook of Auger Electron Spectroscopy, pp. 3.

[45] Let’s Familiarize Ourselves with the SEM, Hitachi High-Tech Corp., pp. 41-47, pp. 88-89.

[46] Tanimura Yasuyuki," Foundation of Fracture Engineering", Nikkan Kogyo Shimbun, Ltd., pp. 144-146 (2009).

[47] Q.K. Zhang and Zhefeng Zhang, "In Situ Observations on Creep Fatigue Fracture Behavior of Sn-4Ag/Cu Solder Joints", Acta Mater., Vol. 59, Issue 15, pp. 6017-6028, (2011).

[48] Japan Institute of Metals and Materials, "Data Book of Metal", Maruzen Co., Ltd., pp. 21-25 (2004).

[49] https://kyjworld.web.fc2.com/binaryphasediagram.htm

[50] Japan Society of Materials Science, Division Committee of Fractography,

"Fractography", Maruzen Co., Ltd., pp. 91-111 (2000).

[51] Takashi Nakamura, "Fundamental Knowledge of Metal Fatigue", J.JFS, Vol. 79, No.2, pp. 58-69 (2007).

[52] Antony Aguilar, Stanislau Y Herasimenka, Joseph Karas, Harsh Jain, Jongwon Lee, Krystal Munoz, Lynne Michaelson, Tom Tyson, William J Dauksher, Stuart Bowden, "Development of Cu plating for silicon heterojunction solar cells", IEEE 43rd Photovoltaic Specialists Conference (PVSC), pp. 1972-1975 (2016).

[53] J. Horzel, N. Bay, M. Passig, M. Sieber, J. Burschik, H. Kühnlein, A. Brand, A. Letize, B. Lee, D. Weber, R. Böhme, "Low cost metallisation based on Ni/Cu plating enabling high efficiency industrial solar cells", 29th European Photovoltaic Solar Energy Conference, pp. 22-26 (2014).

[54] Rehman, Atteq U., and Soo H. Lee., "Review of the potential of the Ni/Cu plating technique for crystalline silicon solar cells", Materials, Vol. 7, Issue. 2, pp. 1318-1341 (2014).

[55] Yu Xinguang, Ryota Domen, Isamu Morisako, Keiko Koshiba, Tomonori Iizuka, Kohei Tatsumi, "Long-term Reliability of Nickel Micro-Plating Bonding by Using Resonant Type Fatigue Testing Machine", Quarterly Journal of The Japan Welding Society, Vol. 40, Issue 1, pp. 1-8 (2022).

[56] Trinasolar Japan Homepage, https://www.trinasolar.com/jp/product/commercial, (2022).

[57] Masuda, Atsushi, Naomi Uchiyama, and Yukiko Hara, "Degradation by acetic acid for crystalline Si photovoltaic modules", Japanese Journal of Applied Physics, Vol. 54, 04DR04 (2015).

[58] Nobuhito Imajo, Keisuke Ohdaira, Atsushi Masuda, "Damp-heat and thermal cycling alternative test on crystalline Si photovoltaic modules without encapsulant", the 69th JSAP Spring Meeting, 26a-F408-4 (2022).

[59] Borri C., Gagliardi M., & Paggi M., "Fatigue crack growth in Silicon solar cells and hysteretic behaviour of busbars", Solar Energy Materials and Solar Cells, Vol. 181, pp. 21-29 (2018).

[60] Chaturvedi P., Hoex B., & Walsh T. M., "Broken metal fingers in silicon wafer solar cells and PV modules", Solar Energy Materials and Solar Cells Vol. 108, pp. 78-81 (2013).

[61] Xiong H., Gan C., Yang X., Hu Z., Niu H., Li J., Si J., Xing P., Luo X., "Corrosion behavior of crystalline silicon solar cells", Microelectronics Reliability, Vol. 70, pp. 49-58 (2017).

[62] Dirk Maler, Peter Schmitt, Patrick Voos, Richard Wagner, "Solar Cell Microstructural Analysis", Published by Buehler, a division of Illinois Tool Works. Vol.

5, Issue. 6 (2015).

[63] Johann Walter, Marco Tranitz, Michael Volk, Christian Ebert, Ulrich Eitner, "Multi-wire Interconnection of Busbar-free Solar Cells", Energy Procedia, Vol. 55, (2014).

[64] Faes Antonin, Despeisse, M., Levrat Jacques, Champliaud J., Badel Nicolas, Kiaee Mohammad, Söderström Thomas, Yao Yu, Grischke Rainer, Gragert M., Ufheil J., Papet P., Strahm B., Cattaneo Gianluca, Cattin Jean, Baumgartner Y., Hessler-Wyser A., Ballif Christophe., "SmartWire solar cell interconnection technology", Proc. 29th Eur. Photovoltaic Sol. Energy Conf., pp. 2555-2561 (2014).

[65] Kenjiro Komai: Mechanical Materials, The Society of Materials Science, Japan 51 (1999).

[66] Hasan, M.K., Sasaki, K., "Thermal deformation analysis of tabbed solar cells using solder alloy and conductive film", Mech Sci Technol, Vol. 30, pp. 3085–3095 (2016).

[67] T. T. Mattila and J. K. Kivilahti, "The role of recrystallization in the failure of SnAgCu solder interconnections under thermomechanical loading", IEEE Transactions on Components and Packaging Technologies, Vol. 33, Issue 3, pp. 629-635 (2010).

[68] Chen, H., Mueller, M., Mattila, T., Li, J., Liu, X., Wolter, K., & Paulasto-Kröckel, M. L, "Localized recrystallization and cracking of lead-free solder interconnections under thermal cycling", Journal of Materials Research, Vol. 26, pp. 2103-2116 (2011).

[69] N. Park, C. Han, J. Jeong and D. Kim, "Lifetime Prediction Model of Thermal Fatigue Stress on Crystalline Silicon Photovoltaic Module", IEEE 39th Photovoltaic Specialists Conference (PVSC), 2013, pp. 1575-1578 (2013).

[70] M.T. Zarmai, N.N. Ekere, C.F. Oduoza, E.H. Amalu, "Optimization of Thermo-Mechanical Reliability of Solder Joints in Crystalline Silicon Solar Cell Assembly", Microelectronics Reliability, Vol. 59, pp. 117-125 (2016).

[71] Musa T. Zarmai, N.N. Ekere, C.F. Oduoza, Emeka H. Amalu, "Evaluation of Thermo-Mechanical Damage and Fatigue Life of Solar Cell Solder Interconnections", Robotics and Computer-Integrated Manufacturing, Vol. 47, pp. 37-43 (2017).

[72] F.X. Che, John H.L. Pang, "Characterization of IMC Layer and Its Effect on Thermomechanical Fatigue Life of Sn–3.8Ag–0.7Cu Solder Joints", Journal of Alloys and Compounds, Vol. 541, pp. 6-13 (2012).

[73] Yasuaki Ishikawa, "Outdoor evaluation of photovoltaic modules using electroluminescence method", Oyo Buturi, 2022, Vol. 91, Iss. 9, pp 558-561 (2022).

Publication Record

1. Paper Publication

○1. Yu Xinguang, Domen Ryota, Morisako Isamu, Koshiba Keiko, Iizuka Tomonori, Tatsumi Kohei, "Long-term Reliability of Nickel Micro-Plating Bonding by Using Resonant Type Fatigue Testing Machine", Quarterly Journal of The Japan Welding Society, Vol. 40, Iss. 1, pp. 1-8 (2022).

○2. Xinguang Yu, Zhi Fu, Isamu Morisako, Keiko Koshiba, Tomonori Iizuka, Kohei Tatsumi, "Improvement in the Reliability of Crystalline Silicon Solar Cell Interconnection by Using Nickel Micro-Plating Bonding (NMPB) Technology", Japanese Journal of Applied Physics, Vol. 62, No. 1, pp. 1-6 (January 2023).

2. Conference Presentation

1. Xinguang Yu, Ryota Domen, Isamu Morisako, Keiko Koshiba, Tomonori Iizuka, Kohei Tatsumi, "Long Term Reliability of Nickel Micro-Plating Bonding by Using Resonant Type Fatigue Testing Machine", the 166th Spring Meeting of the Japan Institute of Metals and Materials, P139 (2020).

2. Xinguang Yu, Ryota Domen, Isamu Morisako, Keiko Koshiba, Tomonori Iizuka, Kohei Tatsumi, "Long Term Reliability of Nickel Micro-Plating Bonding by Using Resonant

Type Fatigue Testing Machine", the 167th Autumn Meeting of the Japan Institute of Metals and Materials, P60 (2020).

3. Xinguang Yu, Ryota Domen, Isamu Morisako, Keiko Koshiba, Tomonori Iizuka, Kohei Tatsumi, "Long Term Reliability of Nickel Micro-Plating Bonding by Using Resonant Type Fatigue Testing Machine", 14th International Collaboration Symposium on Information, Production and Systems (ISIPS) (2020).

4. Xinguang Yu, Ryota Domen, Isamu Morisako, Keiko Koshiba, Tomonori Iizuka, Kohei Tatsumi, "High-Temperature Reliability of Nickel Micro-Plating Bonding by Using Resonant Type Fatigue Testing Machine", the 168th Spring Meeting of the Japan Institute of Metals and Materials, P25 (2021).

5. Xinguang Yu, Zhi Fu, Isamu Morisako, Keiko Koshiba, Tomonori Iizuka, Kohei Tatsumi, "Improvement on Reliability of Crystalline Silicon Solar Cell Interconnection by Using Nickel Micro-Plating Bonding (NMPB) Technology", The 82nd JSAP Autumn Meeting, 2p-S401-2 (2021).

6. Xinguang Yu, Zhi Fu, Isamu Morisako, Keiko Koshiba, Tomonori Iizuka, Kohei Tatsumi, "Application of Nickel Micro-Plating Bonding (NMPB) Technology to Crystalline Silicon Solar Cell Interconnection", The 69th JSAP Spring Meeting, 22p-E106-4 (2022).